# Atomic scale simulations for a better insight in plasma medicine

Proefschrift voorgelegd tot het behalen van de graad van doctor in de Wetenschappen aan de Universiteit Antwerpen te verdedigen door

Maksudbek Yusupov
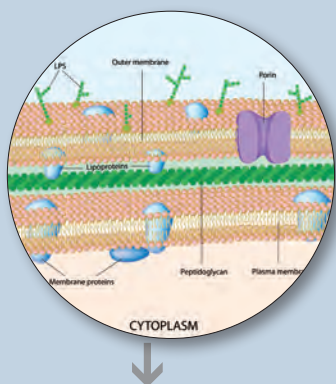

```
...
do i1=1,na
if (c(i1,3).gt.shock_z_sep) then
vel(3,i1) = vel(3,i1) - shock_vel
endif
enddo
endif
100 continue
mdstep=mdstep+1
 if (iflext.eq.1) call chdt
goto (110,120,130,140,150,160,170,180,190,195,196,199) nmethod
stop 'Unrecognised method (check control-file)'
110 call verlet1 !NVT-dynamics with Berendsen thermostat
...
```

Promotoren
prof. dr. Annemie Bogaerts
prof. dr. Erik C. Neyts

Universiteit Antwerpen
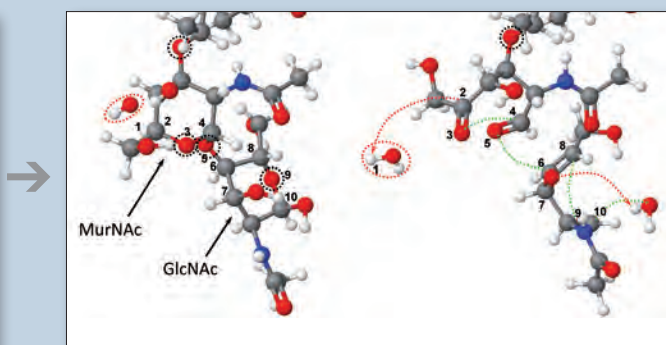
Faculteit Wetenschappen

Departement Chemie

Atomic scale simulations for a better insight in plasma medicine

Simulaties op atomaire schaal voor een beter inzicht in plasma geneeskunde

Proefschrift voorgelegd tot het behalen van de graad van doctor in de Wetenschappen aan de Universiteit Antwerpen te verdedigen door

Maksudbek YUSUPOV

Promotoren: Prof. Dr. Annemie BOGAERTS,

Prof. Dr. Erik C. NEYTS

Antwerpen, 2014

Contents

Acknowledgements

Chapter 1

Plasma medicine: An emerging field

1.1 What is plasma?

1.1.1 Overview

A plasma, the fourth state of matter, is a quasineutral gas consisting of different species, such as electrons, (positive and negative) ions, excited species, neutrals (radicals and molecules), photons, and electromagnetic fields. The quasineutrality of the plasma means that the charges compensate each other.

Much of the visible matter in the universe is in the plasma state; stars, solar corona, the Earth's ionosphere as well as Aurora Borealis are naturally occurring plasmas (see Figure 1.1). Besides omnipresent plasmas in the universe, plasmas can also artificially be created in the laboratory. Two types of laboratory plasmas are distinguished, i.e. the high-temperature or fusion plasmas, and the so-called low-temperature plasmas or gas discharges. Plasmas are also subdivided into plasmas that are in thermal equilibrium (thermal plasmas) and those which are not in thermal equilibrium (non-thermal plasmas).
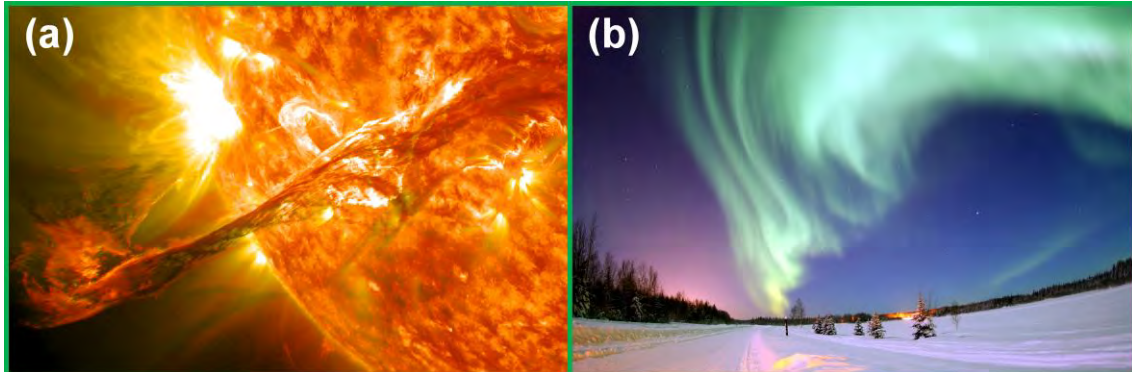
Figure 1.1   *Types of natural plasmas. (a) Solar corona (thermal plasma) and (b) Aurora Borealis (non-thermal plasma).*

In plasmas which are in thermal equilibrium, the temperature of all species (electrons, ions and neutral species) is almost equal. Examples of these kinds of plasmas are stars (natural) and fusion plasmas (man-made). To form thermal plasmas high temperatures are required. On the other hand, if the temperature of different plasma species (more precisely, the temperature of electrons as well as the heavy particles, such as ions and neutral species) is not the same, the plasma is called a non-equilibrium or non-thermal plasma. In these kinds of plasmas the electrons are typically characterized by much higher temperatures than the heavy particles. An overview of various kinds of laboratory plasmas and their

applications can be found in the review of Bogaerts *et al.* [1]. In view of this work, it may also be convenient to categorize plasmas into low- and atmospheric pressure plasmas. More information about non-thermal low temperature plasmas at low and atmospheric pressure is given in *subsection 1.1.2*.

In the rest of the thesis, I will use the term "plasma" to indicate a low-temperature (or room temperature) non-equilibrium (non-thermal) plasma at atmospheric pressure.

1.1.2 Non-thermal low temperature plasmas

Man-made (or laboratory) non-thermal low-temperature (cold) plasmas are generated in their most simple form by applying a sufficiently high potential difference between two electrodes placed in a gas. The electric field breaks down the gas into electrons and ions. Because the electrons are very light, they gain energy from the electrical field much faster than the heavy ions due to the electric acceleration. This consequently leads to an electron temperature increasing quickly to around 10000 K, whereas ions and neutral species can remain at low (nearly room) temperature. The high energy of the electrons gives rise to inelastic electron collisions, which in turn helps to sustain the plasma (e.g., electron impact ionization).

There are many types of non-thermal plasmas, such as direct current (dc), alternating current (ac), radio-frequency (rf, which can be subdivided into capacitively coupled (CCPs) and inductively coupled plasmas (ICPs)), pulsed, atmospheric pressure glow discharges, dielectric barrier discharges (DBDs), corona discharges, plasma jets, magnetron discharges, etc. Each of them has its own specific advantages and applications in different fields [1]. Indeed, low-temperature plasmas are nowadays used for a wide range of applications, both in the industrial (e.g., plasma displays, lighting, lasers, surface modification, etc.), environmental (e.g., water cleaning, destruction of volatile organic compounds, conversion of greenhouse gases, etc.) as well as in biomedical (e.g., sterilization of medical equipment) fields [1].

Recently, the use of low-temperature (or cold) atmospheric pressure plasma (CAPP) sources in biology, health care and medicine is attracting increasing interest and is becoming one of the main topical areas of plasma research [2-4]. The fields of application include disinfection of both living tissue and non-living

surfaces (medical tools, diagnostic devices, etc, see e.g., [5-7]), tooth bleaching [8], treatment of skin diseases [9], killing or apoptosis of cancer cells [10-14] and even tissue regeneration [15]. The use of CAPPs for healthcare purposes consequently led to the emergence of a new innovative field in plasma research, so-called "Plasma Medicine" [2].

1.2 Plasma medicine

1.2.1 Background

Plasma medicine or biomedical application of CAPPs is an emerging field in plasma research. It is a relatively recent area of research compared to traditional areas of plasma processing, and has been growing very quickly in recent years. It is very much a multidisciplinary field on the intersection of medicine, biology, microbiology, chemistry, biochemistry and physics.

A lot of research was performed in the past ten to fifteen years on the interaction of CAPPs with biological materials by many research groups worldwide. In the literature, many reviews on plasma medicine are available, including reviews on plasma medicine (where the authors provide an update on the recent research works related to plasma medicine, and summarize the current status of this emerging field) [2, 15, 16], on CAPP sources and their effects and applications [4, 17-21], on specific plasma sources, such as atmospheric pressure plasma jets (APPJs) [22, 23] and DBDs [24, 25], on decontamination, inactivation, sterilization, etc. [26-29], on CAPPs in and in contact with liquids [30], on the emerging role of reactive oxygen and nitrogen species in redox biology [31], on the application of CAPPs in dermatology [32] as well as reviews on modeling of CAPPs [33] and simulations of plasma-biomolecule interactions [34].

In the following subsections, a brief introduction to CAPP sources (*subsection 1.2.2*), their effects and applications (*subsection 1.2.3*), their interaction with bacteria (*subsection 1.2.4*) and the role of active plasma agents in plasma-surface interactions (*subsection 1.2.5*) will be given, as well as an overview of fundamental studies (experimental and modeling, *subsection 1.2.6*) performed on the interaction of CAPPs with biomolecules.

1.2.2 Cold atmospheric pressure plasma (CAPP) sources

In recent years, a wide range of different CAPP sources have been developed for biomedical applications, e.g., the plasma needle [35], APPJ [36-39], floating-electrode DBD [40], microscale APPJ (i.e., μ-APPJ) [41-43] and DBDs [18, 44, 45]. All these setups have two characteristics in common, i.e., they operate at low (near ambient) temperature and at atmospheric pressure.
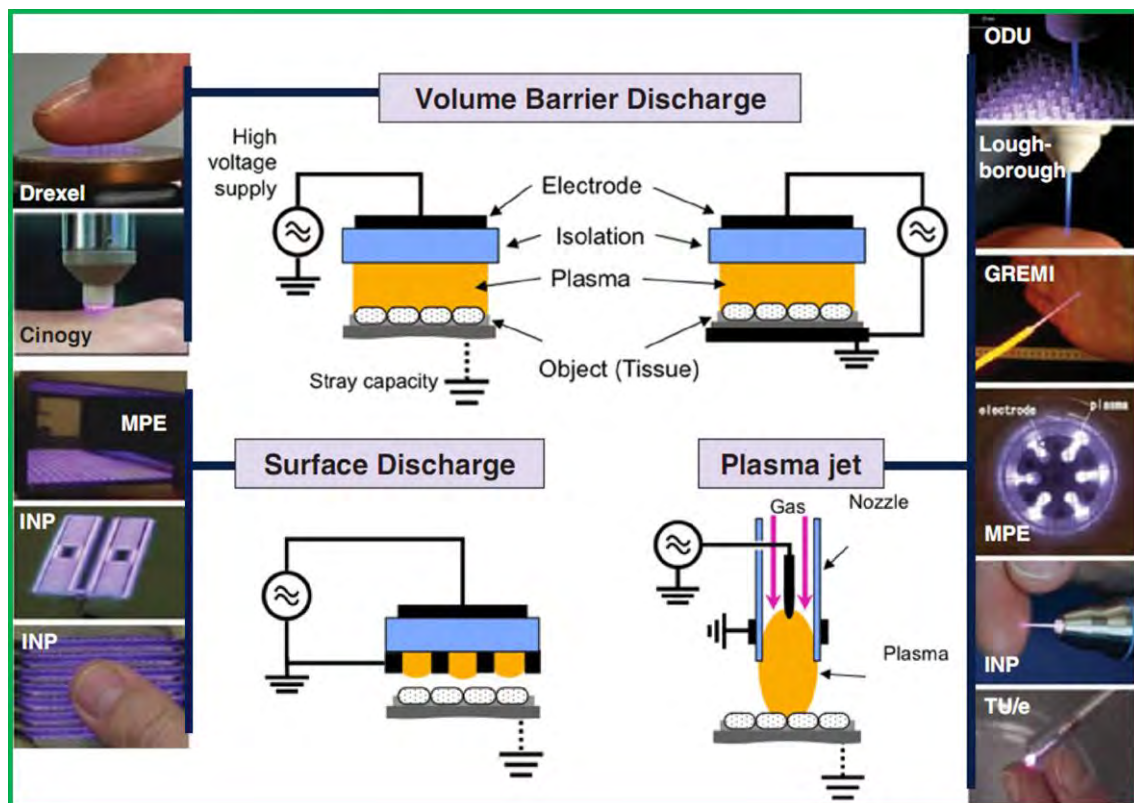
Figure 1.2 *Different types of CAPP sources used in plasma medicine (adapted from [21, 46]).*

They are used in the main areas of plasma medicine, such as biological decontamination (i.e., the decomposition or removal of micro-organisms, such as bacteria, bacterial spores, fungi, viruses, endotoxins and harmful proteins such as prions) and therapeutic applications (i.e., treatment of skin diseases, wound healing, cancer treatment, etc). Figure 1.2 illustrates the different types of CAPP sources that were developed in various laboratories, such as INP (Greifswald, Germany), TU/e (Eindhoven, Netherlands), GREMI (Orléans, France), etc. in recent years.

Following the classification from von Woedtke and coworkers [21], CAPP sources can be divided into three types, i.e., (dielectric) barrier discharges

((D)BDs), plasma jets, and corona discharges [23, 24, 36, 47, 48]. Up to now, research activities were mainly focused on DBDs and plasma jets at atmospheric pressure [21], see schematic pictures in Figure 1.2. Only these two CAPP setups will be described here. A detailed description of all kind of CAPP sources used in plasma medicine as well as about their operating conditions has been reported in [17, 18, 21-23, 25].

Non-thermal atmospheric pressure DBD devices consist of two plane-parallel metal electrodes, where at least one of these electrodes is covered by an isolating (i.e., dielectric) layer. The reason for using this dielectric barrier in the discharge gap is to limit the discharge current and to avoid the transition to an arc. There are different types of DBDs with various electrode geometries used in plasma medicine (see Figure 1.2 and Figure 1.3 for schematic illustrations), depending on the applications [17, 18, 21].
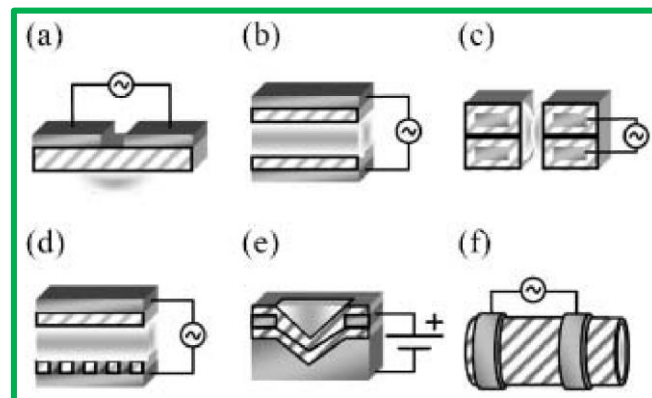
Figure 1.3 *Schematic pictures of various DBD configurations. (a) coplanar DBD, (b) parallel plate DBD, (c) coaxial DBD, (d) capillary plasma electrode discharge, (e) pyramidal DBD, and (f) capillary discharge/plasma pencil/plasma jet. Metal electrodes are shown in solid color and hatched objects represent dielectric materials (adopted from [25]).*

One of the main advantages of the DBD is that the discharge can be ignited without much effort in a broad range of operating conditions and that a stable discharge can be sustained. For instance, a variety of gases can be used in DBDs, including noble gases, air, water vapor, or special admixtures of nitrogen and oxygen. Furthermore, most DBDs are direct plasma sources (see [2]), i.e., these devices use the target (e.g., skin or other tissue) as the counter electrode and charged particles can reach the surface of this target. The total area of

treatment can be very large and is related to the size of the electrodes. A disadvantage of these setups is the need for a more or less constant distance to the treatment area [20]. The gas temperature in DBDs is typically quite low, i.e., about room temperature [17, 21].

Non-thermal APPJs are also frequently used plasma sources in biomedical applications. APPJs consist of a tube with (often) two electrodes (through which the working gas flows), and are typically operated in rf mode (e.g., at 13.56 or 27.12 MHz). RF power is applied to the electrode, which leads to the ignition of the gas discharge. APPJs exist in various designs (see Figure 1.2 and Figure 1.4 for schematic illustrations) due to the different arrangements and geometries of the electrodes (e.g., powered electrode can be in the shape of a ring, needle, etc., see [17, 22]).

Due to the gas flow the plasma can exit through the nozzle and reach the surface located at several centimeters after the tube end. Working gases are typically noble gases, such as helium and argon (with small percentage of reactive gases, such as O_2) [17]. In general, due to the high gas flow and low power consumption, the gas temperature is typically around 350 K. However, it can be decreased to ambient temperature using special electrical input signals (e.g., burst mode, see [18]). On the other hand, in the DBD jet (see Figure 1.4), the gas temperature of the plasma remains close to room temperature [22]. APPJs can be used in direct mode (where a variety of agents can reach the target) or in remote mode (where only the chemical species and radicals are effective). However, most of the APPJs work in direct mode [17].

The main advantage of APPJs is that the generated plasma is able to penetrate into small structures or narrow gaps with high aspect ratios due to small plasma dimensions [19]. Thus, even complex geometries with micro-structured cavities or capillaries can be easily treated with APPJs, which makes them particularly interesting for biomedical applications [17].

Another advantage of APPJs is the high etch rate [49], which is also important for e.g., removal of microorganisms from surfaces.

A disadvantage of APPJs is that these devices, even when operating in direct mode, are still related to indirect plasma sources (see [2]); the target (which needs to be treated) is not used as a counter electrode, i.e., the plasma generated inside the nozzle is transported to the object by a carrier gas flow. This makes

8

the plasma less controllable. Moreover, the concentrations of the plasma species in APPJs are normally lower than in direct DBD sources [20].
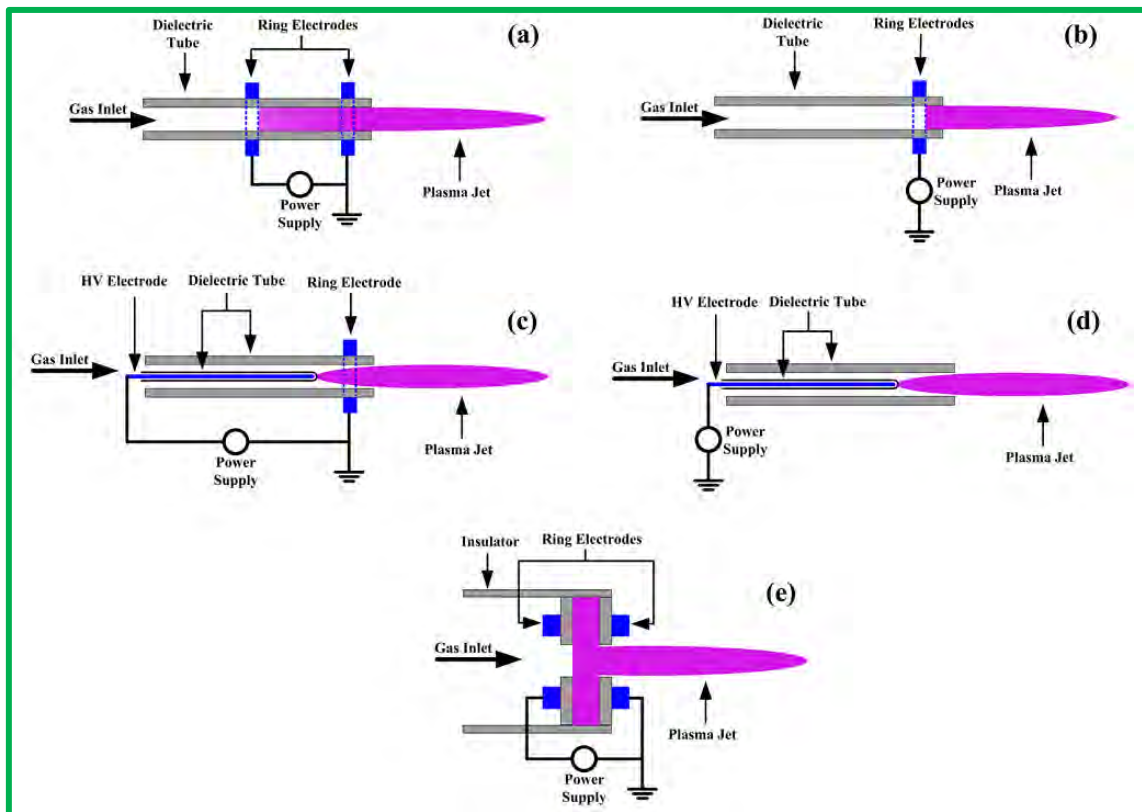
Figure 1.4 *Schematic representations of various APPJ configurations. (a) jet with two ring electrodes, (b) jet with one ring electrode, (c) jet with a centered pin electrode and one ring electrode, (d) jet with a centered pin electrode without grounded electrode, (e) jet with two ring electrodes that are attached to the surface of two centrally perforated dielectric disks (adopted from [22]). Note that all APPJs shown here are in fact DBD plasma jets [22].*

1.2.3 Effects and applications of cold atmospheric pressure plasmas

Plasma medicine envisages to offer an improved alternative to existing technologies for e.g. inactivation of microorganisms, blood coagulation, cancer treatment, and dental surgery. Plasma medicine generally makes use of a variety of CAPP sources as described above, by altering the external plasma process parameters (e.g., gas mixture composition, driving frequency and voltage), and hence by generating a variety of biologically active agents in these devices. However, to achieve this, a thorough understanding of the interaction mechanisms of the plasma with biochemically relevant structures is required, in

order to control the processes occurring in the plasma, as well as in the contact region of the plasma with the bio-organisms. This still remains a challenge.

In general, applications of CAPPs can be subdivided into two parts:

a) sterilization or disinfection of non-living surfaces (e.g., microbial deactivation of surgical and medical equipments, packaging materials, food and food product lines, seeds, etc.)

b) decontamination of living surfaces (e.g., treatment of skin diseases, killing or apoptosis of cancer cells, blood coagulation, wound healing, etc.)

Sterilization or disinfection of non-living surfaces. Recent experimental studies have demonstrated that CAPPs can provide an attractive alternative for inactivation and removal of hazardous biomolecules, such as bacteria, fungi, viruses, etc [27, 29, 50-61]. Moreover, they can be sustained in nontoxic gases, such as argon, hydrogen or oxygen, which implies their relative safety to the staff, as well as to the environment. Moreover, in view of their nonthermal nature (which is ideal for heat-sensitive materials), CAPPs may possibly replace conventional sterilization methods (e.g., autoclave) in the near future [5].

Experimental work is currently being performed on the decontamination of microorganisms in both dry and humid air as well as in solution (see e.g., the review of Bruggeman and Leys [30] and also see [62-65]). However, the inactivation mechanisms in these environments are still poorly understood and need to be investigated in more detail.

It should be mentioned that plasma deactivation is not only limited to the medical field (i.e., reprocessing of medical devices, such as endoscopes, surgical instruments, etc.) but can also be applied to the decontamination of seeds, food and their storage containers (see review from Niemira [66] and also see [67-71]).

Decontamination of living surfaces. The idea of using CAPPs in medical therapy (i.e., application of CAPPs to sensitive living surfaces like human skin) arose only after their application to non-living surfaces (see above). Indeed, CAPPs can be used in dermatology (for skin disinfection/antisepsis), while having no damage to the sensitive surface of biomaterials; this is due to the gas temperature of CAPPs, which is below the destruction threshold.

One of the areas of plasma medicine, where the use of CAPPs is being investigated, is in blood coagulation. CAPPs allow blood coagulation both in hospital emergency rooms and at the accident site in a secure manner [40, 72], specifically by slowing bleeding. Effects of blood coagulation by plasma have been demonstrated by research groups not only *in vitro* [73, 74], but also *in vivo* using an animal model [75].

Plasma sources are also able to kill bacteria that cause infections in skin wounds and ulceration without having a negative effect on human tissue [40, 76, 77]. Note that the treatment (with conventional antibiotics) of such infections is often problematic.

Various experimental works devoted to cancer treatment by CAPPs can also be found in the literature (see [10-14, 78-80]). Recently, at GREMI (France), a novel plasma source called plasma gun has been developed [81, 82]. It is based on a pulsed DBD reactor, which is connected to a dielectric catheter-like flexible silicon or polyimide tube. It allows plasma treatment not only on outer surfaces of the body (e.g., skin cancer) but also inside the body (other types of cancer).

Other applications of CAPPs in plasma medicine are also mentioned in the literature, including dermatology (see e.g. [32, 83]), wound healing (see e.g. [84-91]) and tooth bleaching (see e.g. [8, 44, 92]).

1.2.4 Interaction of cold atmospheric pressure plasmas with bacteria

As mentioned above, one of the main current applications of CAPPs is the sterilization of surfaces, i.e., disinfection (mainly) from bacteria. As this application is also studied in this PhD thesis, I will go a bit more in detail here. Based on the structural characteristics of the cell wall, bacteria can be divided into two large groups, i.e., gram-positive and gram-negative. The cell wall of both gram-positive and gram-negative bacteria is illustrated in Figure 1.5.

The outer part of the cell wall of gram-positive bacteria, e.g. *Staphylococcus aureus* (*S. aureus*), is composed of peptidoglycan (PG, see Figure 1.5(a)). PG, also known as murein, is an important component of the bacterial cell wall and is found on the outside of almost all bacterial membranes [93-95]. It forms a mesh-like layer composing the cell wall and serves as a protective barrier in bacteria. The PG layer is substantially thicker in gram-positive bacteria than in

gram-negative bacteria. For instance, in the gram-positive bacterium *S. aureus*, the PG structure is typically 20-30 nm thick, whereas in a gram-negative bacterium, such as *Escherichia coli* (*E. coli*), it is only 6-7 nm thick [96-98] (see Figure 1.5).
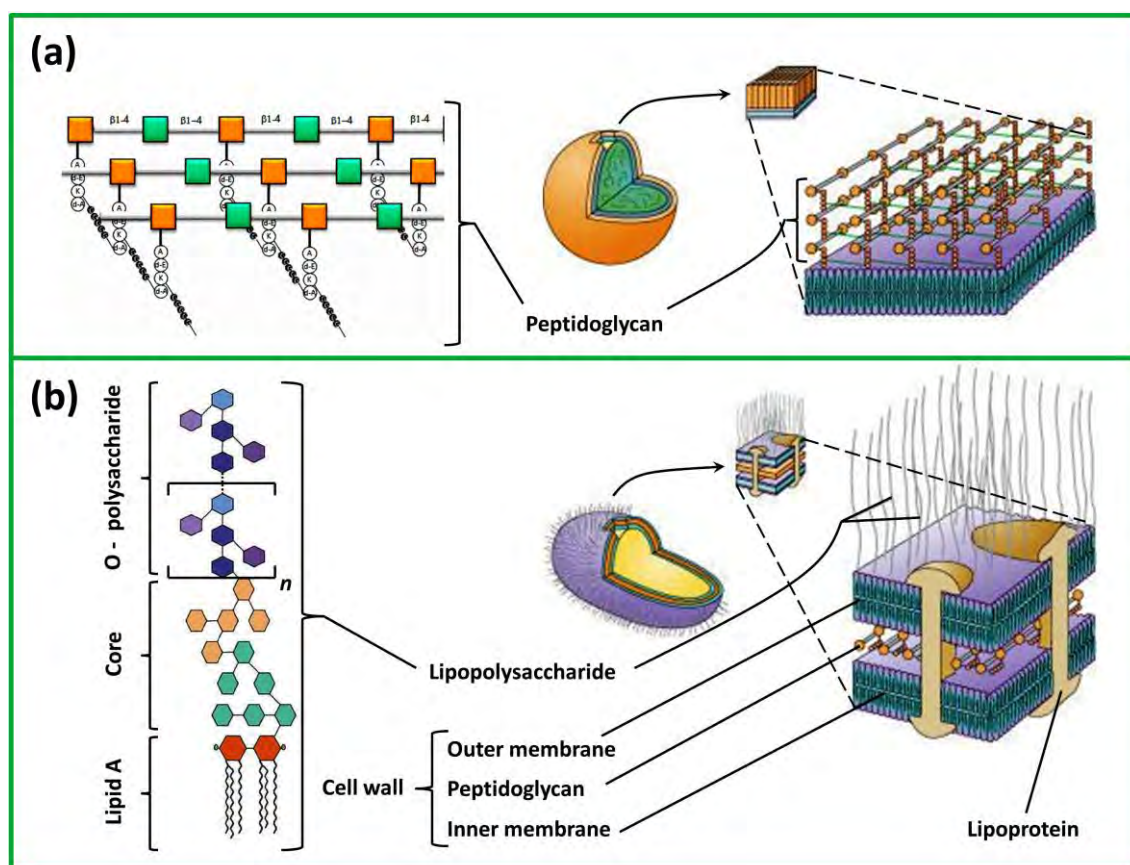
Figure 1.5   *Schematic representations of gram-positive (a) and gram-negative (b) bacteria.*

PG is assembled from repeating units consisting of a disaccharide (see Figure 1.5(a), orange and green squares), a stem (see Figure 1.5(a), open circles) and a bridge (see Figure 1.5(a), solid circles). A more detailed explanation of the PG structure is given below in *chapter 3*.

As mentioned above, PG is the outer protective barrier in bacteria and can therefore interact directly with plasma species. Reactive plasma species can react with PG, dissociate the important bonds in the PG and consequently lead to the destruction of the PG structure, which in turn results in subsequent structural damage of the bacterial cell wall.

PG is, however, of less importance in gram-negative bacteria. In these bacteria the PG layer is encapsulated by another membrane (see Figure 1.5(b)).

This outer membrane is composed of an asymmetric bilayer. The outer leaflet of the outer membrane is composed of lipopolysaccharide (LPS), rather than the usual glycerophospholipids found in most other biological membranes. LPS is composed of three parts, namely (a) the inner hydrophobic lipid A, (b) the core oligosaccharide which connects (c) the outer O-antigen polysaccharide to lipid A (see Figure 1.5(b)). The O-antigen is a repetitive glycan polymer of which the composition varies in different gram-negative bacteria and has a hydrophilic nature. Since the O-antigen comprises the outermost region of gram-negative bacteria it is by consequence targeted by hosts for antibody recognition. Lipid A consists of multiple fatty acid chains connected to two glucosamine units containing a phosphate group (see Figure 1.5(b), red hexagons and solid circles connected to them, respectively).

LPS is not only important for the structural integrity of gram-negative bacteria, it is also an endotoxin and the presence of LPS in the human bloodstream can result in a generalized sepsis syndrome including fever, hypotension, respiratory dysfunction, and may lead to multiple organ failure and even death [99].

The toxicity of LPS is mainly linked to lipid A and the toxic activity of lipid A is highly correlated to its molecular structure. Any deviation from its structure (e.g., the number and length of the fatty acid groups, as well as the phosphorylation state) decreases the toxicity of lipid A [100]. More information about the chemical structure of lipid A is given below in *chapter 5*.

Thus, the fundamental study of the interaction of plasmas with lipid A can be useful for improving our understanding about the destruction mechanisms of lipid A molecules, and hence, to obtain a better insight in the antibacterial properties of plasmas.

1.2.5 Plasma-surface interactions: the role of active plasma agents

CAPPs produce a large variety of biological active agents, such as reactive oxygen species (ROS) (e.g., O, OH, HO_2, H_2O_2, O_3) and reactive nitrogen species (RNS) (e.g., NO, NO_2, HNO_2, ONOOH) [31], charged particles, ultraviolet (UV) radiation and electric current, due to the complex physical and chemical processes occurring in a low temperature plasma [17, 21]. Many

experimental studies have been performed in order to identify the role of these plasma agents for e.g., microorganism inactivation processes [28, 29].

Electric current is mainly produced in direct DBD type discharges and also in some types of APPJs (where ions and electrons can play a key role). Electricity is being used for a long time in medicine and has many therapeutic effects [21]. Also in the context of plasma medicine, it was revealed that both positive and negative plasma ions play an important role in the interaction between biological organisms and plasma [101]. When relying on electric currents for therapeutic effects, it is obvious, however, that the current should be sufficiently low so as not to induce any unintended effects.

UV radiation is also produced by plasma sources, but usually in low concentrations. UV radiation is known for its therapeutic effects (e.g., induction of vitamin D production) and can be used in treatment of psoriasis (skin disease causing itch) or vitiligo (skin disease causing depigmentation of parts of the skin). However, a long-term exposure to UV radiation can cause skin erythema (redness of the skin), keratitis (inflammation of the eye) and eventually may lead to skin photoageing, cancer and cataract [102].

In CAPPs at low (i.e., tissue tolerable) temperatures, oxygen chemistry is often dominant. In this case, one major long living component is ozone. In hotter plasmas (with initial temperatures higher than 200 °C), nitrogen species typically dominate the chemistry [21]. Some of the experimental studies revealed that ROS, such as O and OH, play a dominant role in inactivation of bacteria, whereas other plasma-generated components (e.g., UV photons, charged particles, electric fields, and heat) have a minor contribution [103-106]. Moreover, it was found that the APPJ generates high densities of atomic oxygen and ROS [37]. Several experimental studies showed that plasma-induced apoptosis is triggered by ROS [78, 107-109]. However, RNS can also induce apoptosis [110]. Moreover, it was concluded that DNA inactivation is mainly caused by ROS, whereas thermal effects, UV radiation, or electrical fields and charged particles are found to be less important [111-115]. Bai *et al.* [62] and Hähnel *et al.* [64] have suggested that OH radicals are the key agents responsible for the inactivation of bacteria. Moreover, Xiong *et al.* have also proposed O and OH as inactivating species because they can easily penetrate into the biofilms surrounding bacteria and kill the bacteria [116].

The influence of feed gas humidity on the microbicidal efficiency was also investigated [64]. Moreover, it was predicted by numerical modeling that H_2O_2 molecules are among the dominant species in the afterglow region of a surface microdischarge in humid air at atmospheric pressure [117].

1.2.6 Overview of fundamental studies (experimental and modeling) of plasma interacting with bio-organisms

Effective biomedical application of CAPPs requires understanding the interaction mechanisms of the plasma-generated species with biochemically relevant structures, in order to control the processes occurring in the contact region of the plasma with the bio-organisms. However, this still remains a big challenge, although some fundamental investigations have already been carried out by experiments [118-121], as well as by simulations [122-125].

In [118-121], the authors investigated the antibacterial mechanisms of plasma, including separate and synergistic effects of plasma-generated ultraviolet and vacuum ultraviolet (UV/VUV) photons and particles (or radicals) at the cellular and molecular level for different kinds of biomolecules.

For example, Lackmann *et al.* experimentally found that both plasma-generated particles and UV/VUV photons modify DNA nucleobases and the particles also induce breaks in the DNA backbone. Moreover, the authors showed that plasma-generated particles cause physical damage to the cell envelope, whereas UV radiation does not. Furthermore, the study on the dried bacteria containing glyceraldehyde 3-phosphate dehydrogenase (GAPDH) protein has revealed that the treatment with a complete jet for 10 s caused greater inactivation rates than the combined rate for the particle-only jet and the UV-only jet, demonstrating some synergy of particles and UV in plasma-medicine [118].

Bartis *et al.* examined the effects of direct plasma, plasma-generated high-energy photons in UV/VUV, and radicals on lipopolisaccharide (LPS) using an inductively coupled low-pressure plasma [119]. They found that the direct plasma treatment causes rapid etching and deactivation of LPS: for both Ar and H_2 as feed gas, the direct treatment reduces the film thickness by ~50% after about 1 min of exposure. On the other hand, plasma-generated reactive neutrals

(mostly atomic O in Ar plasma and atomic H in H_2 plasma) cause a minimal etching of the films compared to direct plasma treatment, but these species deactivate the sample. Moreover, the authors showed that the radical treatment did not significantly affect the phosphorous and nitrogen content in contrast to direct and UV/VUV treatments.
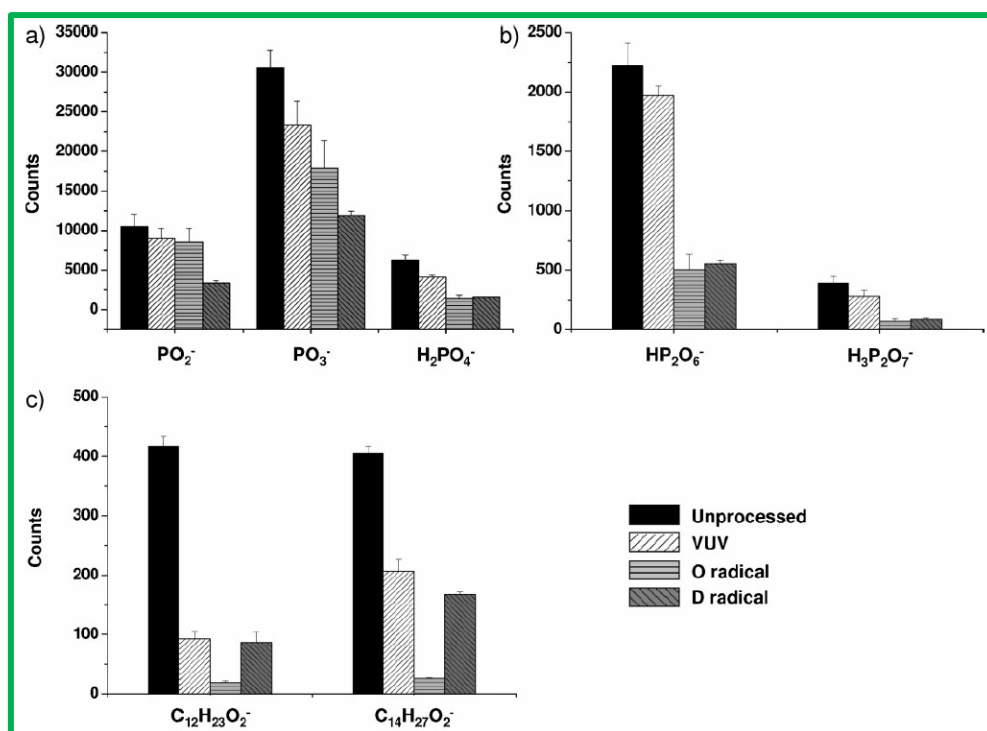
Figure 1.6 *The change of characteristic ToF-SIMS (i.e., time-of-flight secondary ion mass spectrometry) peaks. (a) phosphates, (b) pyrophosphates, and (c) fatty acids (adopted from [120]).*

In both Ar and H_2 plasmas, the C–O and C=O groups slightly increased, whereas the C–C/H bonds decreased after the radical treatment of LPS. The authors concluded that the radicals play a significant role in the deactivation and modification of the LPS and lipid A films, despite negligible material removal.

Similar conclusions were made by Chung and coworkers when studying the effects of VUV radiation, oxygen and deuterium radicals on the endotoxic biomolecule lipid A (which is the toxic part of the LPS) using a vacuum beam system [120]. The authors observed a lower etching yield for radical exposure compared to VUV-induced photolysis, i.e., the bulk chemical change was dominated by VUV photolysis, whereas the radical exposures resulted in chemical etching and modification only at the surface of the lipid A films. The

phosphate moieties and intact aliphatic chains, on the other hand, all decreased significantly in the case of radical exposure, even more than in the case of the VUV- treated samples (see Figure 1.6). The authors also found that after radical exposure the endotoxic activity of lipid A was significantly reduced [120].

Using an APPJ, Bartis *et al.* also showed the importance of oxygen species in the deactivation of LPS. They concluded that as soon as O_2 gas is added to the plasma, stronger deactivation takes place, i.e., the oxygen species are required for deactivation of LPS in the APPJ [121]. Moreover, using X-ray photoelectron spectroscopy (XPS) the authors showed a decrease in the C–C/H and a slight decrease in the O–C–O/N–C=O and O–C=O bonding, while the C–O/C=O bonds increase after a treatment of LPS by 1% O_2 in Ar APPJ containing various N_2 concentrations (see Figure 1.7) [121].
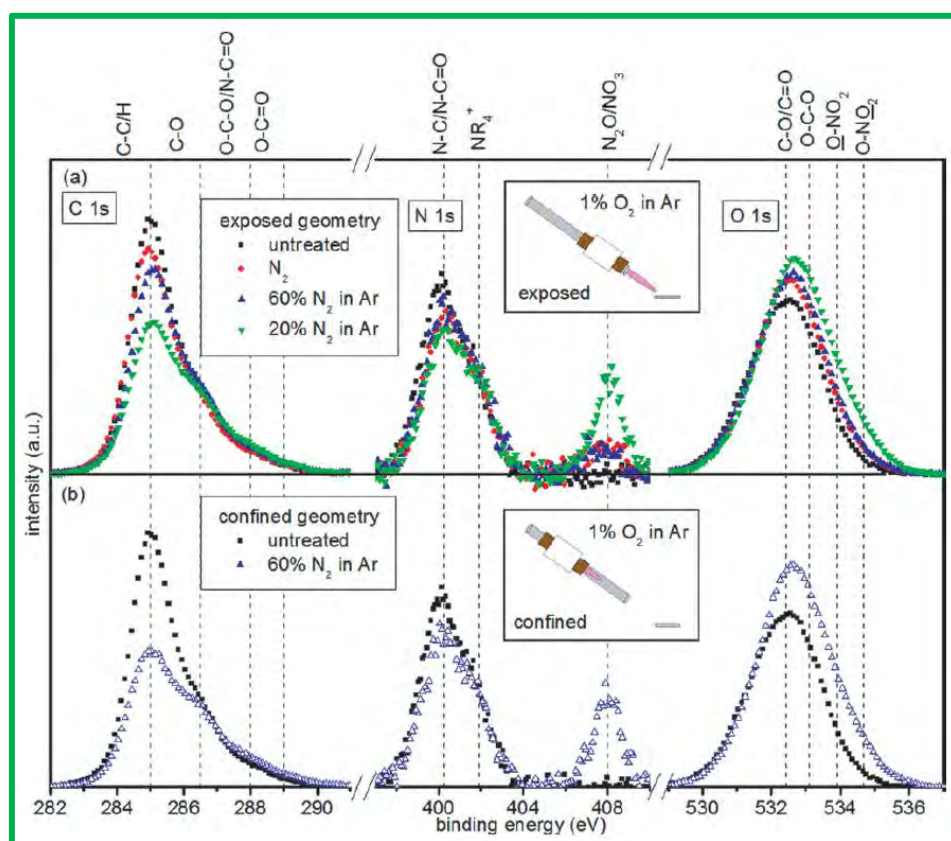
Figure 1.7 *XPS spectra of treated LPS films in N₂/Ar environments. The plasma is (a) exposed to the environment and (b) confined within the alumina tube (adopted from [121]).*

The authors also found that when N_2 was added to the feed gas, the ROS were reduced, which, in turn, led to a decrease in the biological deactivation (see Figure 1.7).

Complementary to experimental studies, computer simulations may also provide fundamental information about the processes occurring, both in the plasma and more importantly at the surface of living cells, which is difficult or even impossible to obtain through experiments. On the other hand, simulating the interaction of plasma with bio-organism (e.g., bacteria) is very difficult compared to modeling e.g., solid state materials. However, if a proper interatomic potential can be constructed for accurately describing all relevant interatomic interactions, molecular dynamics (MD) simulations can provide atomic scale insights. Information about recent modeling works related to CAPPs as well as to the plasma-biomolecule interactions can be found in the review papers of Lee *et al.* [33] and Neyts *et al.* [34], respectively.

Until now, however, very limited efforts have been spent on modeling the interaction of plasma species with living organisms, such as bacteria [122-125].

For example, Babaeva *et al.* performed molecular dynamics (MD) simulations to study the sputtering processes of lipid-like material, which is found on the cell membrane [122]. They found that prolonged exposure of the model lipid-like film to energetic ions can produce significant carbon removal.

Recently, Cordeiro employed MD simulations to determine the distribution, mobility and residence times of various ROS, such as superoxide, OH and HO_2 radicals as well as O_2 and H_2O_2 molecules, at the membrane-water interface [123]. He reported that O_2 molecules accumulate at the membrane interior, whereas superoxide radicals and H_2O_2 molecules remain at the aqueous phase. Both OH and HO_2 radicals, on the other hand, were able to penetrate deep into the lipid head groups region.

Abolfath *et al.* performed MD simulations to investigate the damage to a fragment of DNA in solution by free OH radicals, which are primary products of megavolt ionizing radiation in water-based systems [124]. They found that OH radicals are the main source of hydrogen-abstraction and formation of carbonyl and hydroxyl groups, which finally results in DNA single and double strand breaks.

Moreover, using MD simulations, the interaction of O and OH radicals with α-linolenic acid as a model system for the free fatty acids present in the upper skin layer was investigated in [125]. The calculations predicted that the abstraction of hydrogen atoms from fatty acids by O and OH radicals takes place, which in turn leads to the formation of a conjugated double bond, but also

to the incorporation of alcohol or aldehyde groups, thus increasing the hydrophilic character of the fatty acids and changing the general lipid composition of the skin. This is an important result, as it demonstrates the change in homeostatic function of the skin under influence of plasma radicals.

1.3 Aim of the work

Based on the considerations mentioned above, in this thesis, the interactions of plasma species with the outer part of both gram-positive and gram-negative bacteria, as well as with the liquid layer surrounding biomolecules are investigated by means of MD simulations. The plasma species under study are ROS, namely O, OH, HO_2 radicals as well as H_2O_2 and O_3 molecules. The model systems used in these studies are given below.

In *chapter 3*, the interaction of O, OH radicals as well as O_2, O_3, H_2O_2 and H_2O molecules with bacterial PG of the gram-positive bacterium *Staphylococcus aureus* is investigated by means of reactive MD simulations. PG is the outer layer of the cell wall of gram-positive bacteria and can therefore directly interact with plasma species. Moreover, it serves as a protective barrier, and its destruction can therefore lead to structural and chemical damage of the entire bacterium (see *subsection 1.2.4* above).

The effect of the liquid film (surrounding the bacteria) on the behavior of the reactive plasma species, namely O, OH, HO_2 and H_2O_2, is investigated in *chapter 4*. Water is considered as a model system for the plasma-liquid film interactions, since the largest component of the biofilm (or liquid film) surrounding most bio-organisms, including bacteria, is water [126]. Moreover, many experimental studies on the inactivation of bacteria using CAPP sources are performed in aqueous solutions or water [30, 62, 127-129]. Thus, our atomic level investigations are an important contribution towards a better understanding of the basic phenomena and processes occurring on/in a liquid film when being exposed to the bombardment of plasma species.

Finally, in *chapter 5*, reactive MD simulations are performed to study the interaction of ROS, more specifically OH and HO_2 radicals as well as H_2O_2 molecules, with the endotoxic biomolecule lipid A of the gram-negative

bacterium *Escherichia coli*. The chosen model system, lipid A, is the toxic region of the LPS (see *subsection 1.2.4* above). The goal in this work is to study whether the ROS destroy the lipid A structure and thereby decrease its endotoxic activity. A comparison and verification of our simulation results to experimental observations (see [119-121]) is also presented. The performed simulations can be useful for improving our understanding about the destruction mechanisms of lipid A molecules, and hence, to obtain a better insight in the antibacterial properties of plasmas.

These investigations are highly important for gaining a more fundamental insight into the mechanisms of plasma species interacting with bacteria and in plasma disinfection in general.

Chapter 2

Computational methodologies

2.1 Introduction

Nowadays, *computer simulations* play a very important role in research. In the past, research was characterized by the interplay between theory and experiment. With the advent of high speed computers (started to be utilized since the 50s), this picture changed; computer simulation methods (or so-called "computer experiments") became important in research due to their ability to "bridge" theory and experiment. One of the advantages of the computer experiments is that process parameter interdependencies can be resolved, which might be difficult or impossible to do in a real experiment. Moreover, computer simulations can often be performed for conditions close to the experimental conditions and the obtained simulation results can be compared directly with experimental observations. Other simulations may not correspond to experimental conditions, but still may provide complementary information. This, in turn, makes computer simulations an extremely powerful tool to both understand phenomena underlying experimental observations, but also to study regions that are not attainable experimentally.

2.2 Computer simulation methods

Owing to fast and powerful computers large and complex systems (e.g., biological structures, such as proteins) can be investigated using computer simulations. Two main families of simulation techniques at the atomic scale are *Monte-Carlo (MC)* and *Molecular Dynamics (MD)* simulations; a variety of hybrid models that combine features from both techniques exist as well. The choice between MD and MC is largely determined by the phenomenon under investigation. In this work, I only use classical MD simulations, in which the electronic structure of the system is not taken into account explicitly. If a higher accuracy is required, electronic effects should be taken into account, and one must resort to ab initio techniques (see below).

MD simulations are deterministic, which means that they do not rely on random numbers, in contrast to MC simulations. MD simulations are based on the integration of the equations of motion of the particles. The first proper MD simulation was reported by Alder and Wainwright in 1956 (and published in

1957, see [130]), who studied the dynamics of an assembly of hard spheres. MD simulations have been used to study a wide range of problems in many areas, including physics (theory of liquids, properties of statistical ensembles, structure and properties of small clusters, phase transitions, etc.), chemistry and biology (molecular structures, structure of membranes, dynamics of large biomolecules, protein folding, etc.), material science (defects in crystals, surface reconstruction, melting, film growth, etc.) and so on [131]. The advantage of MD is that it can be used for e.g. the determination of transport properties (such as viscosity coefficients, diffusion coefficients), whereas MC lacks an objective definition of time. Dynamical properties of the system can thus be investigated by MD simulations. As mentioned above, the disadvantage of classical MD simulations is that the description of the electronic (quantum) or excited states is difficult. Moreover, the accuracy of chemical reactions as simulated by classical MD is lower than by DFT or quantum-chemical methods. The attainable time scale, however, is in the order of nanoseconds to perhaps a microsecond, which is orders of magnitude larger than attainable by ab initio methods. Indeed, in quantum (or ab initio) MD simulations (which were developed more than thirty years ago by the work of Car and Parinello [132]), chemical reactions can be described with very high accuracy. Specifically, this method takes the quantum nature of the chemical bond explicitly into account. The electron density function for the valence electrons is calculated using quantum equations to determine bonding in the system, whereas the dynamics of ions (nuclei with their inner electrons) are followed classically. However, as mentioned above, this method is computationally very expensive and it requires more computational resources than classical MD simulations.

Therefore, currently only classical MD is practical for simulating e.g. biomolecular systems, which are composed of several thousands of atoms, over time scales of nanoseconds.

2.3 Classical Molecular Dynamics

2.3.1 Newtonian dynamics

As mentioned above, in this work classical MD simulations are used, in which the trajectories of all atoms in the system are calculated by integrating the equations of motion. However, it is known that systems at the atomistic level obey quantum laws rather than classical laws and that the *Schrödinger* equation is the one to be followed [133]. On the other hand, the Schrödinger equation can only be applied for the simplest systems, i.e., it is not possible to solve analytically the Schrödinger equation for complex systems, which consist of many atoms. To find the solutions for complex systems, the so-called *Born-Oppenheimer* approximation is applied [134]. According to this approximation, MD treats the atoms (atomic nuclei) as *classical* particles and assumes that the electrons are permanently in their ground state, such that the atomic interactions can be described by interatomic potentials dependent on the positions of the nuclei only. Thus, the Newton dynamics describe the nuclear motion.

A simple test of the validity of this classical approximation is based on the *de Broglie thermal wavelength* [135, 136] defined as:

$$\Lambda = \frac{h}{\sqrt{2\pi m k_B T}} \tag{2.1}$$

where m and T are the atomic mass and temperature, and h and k_B are the Planck constant and Boltzmann constant, respectively. The classical approximation is justified if Λ is much smaller than the mean nearest neighbor separation (or interatomic distance). In the case of H, C, N, O, P at a temperature $T = 300$ K, the wavelengths are 1.0, 0.29, 0.269, 0.252, 0.181 Å, respectively. In this work, the mean nearest neighbor interatomic distance is in the range of about 1-2 Å; hence, the interatomic distances (in this range) are at least four times larger than *de Broglie Λ wavelengths* given above, except for H. In principle, classical MD simulations cannot be performed for H atoms. However, in practice, it turns out that classical MD simulations still give reasonable results even for systems where H is present [137]. Thus, one can conclude that Newton's equations can be applied in this work.

In MD simulations, the time evolution of a set of interacting atoms in the system is followed via the solution of Newton's equations of motion, which can be formulated as follows:

$$\boldsymbol{F}_i = m_i \frac{d^2 \boldsymbol{r}_i(t)}{dt^2} \tag{2.2}$$

where $\boldsymbol{r}_i(t)$ is the position vector of atom i and $\boldsymbol{F}_i$ is the force acting on atom i at time t, and m_i is the mass of the atom. The integration algorithm used in this work for MD simulations is described below in *subsection 2.3.2*. Forces acting on the atoms are derived as the negative gradients of the potential energy (interatomic potential) U with respect to the atomic positions:

$$\boldsymbol{F}_i = -\nabla_{r_i} U(\boldsymbol{r}_1, \dots, \boldsymbol{r}_N) \tag{2.3}$$

Obviously, the accuracy of the interatomic potential used in MD simulations is very important. The most widely used interatomic potentials for complex bio-systems are discussed in *subsection 2.3.8*.

2.3.2 Integration algorithms

There are many different algorithms that are used for numerically solving Newton's equation of motion. Because of its simplicity and stability, the *Verlet algorithm* is commonly used in MD simulations [138]. This algorithm complies with the five main criteria for the integration algorithm, namely, good stability (i.e., conservation of total energy and momentum), time-reversibility, robustness (i.e., permitting a long time step), accuracy (i.e., remain close to the "true" trajectory) and being symplectic (i.e., conservation of phase space volume). The basic formula for this algorithm can be derived from the Taylor expansions for the positions $\boldsymbol{r}(t)$:

$$\boldsymbol{r}(t + \Delta t) = 2\boldsymbol{r}(t) - \boldsymbol{r}(t - \Delta t) + \boldsymbol{a}(t)\Delta t^2 + O(\Delta t^4) \tag{2.4}$$

where $\boldsymbol{a}(t)$ the acceleration, Δt is the time step and $O(\Delta t^4)$ is the *truncated error*. The truncated error of the algorithm is of the order of Δt^4. Note that the errors are intrinsic to the algorithm and do not depend on the implementation. They

can only be reduced by decreasing the time step *Δt* (see *subsection 2.3.7*). Since we are integrating Newton's equations, *a(t)* is just the force divided by the mass, where the force is a function of the positions *r(t)* (see eqn (2.3)).

Obviously, equation (2.4) is accurate up to terms of the fourth power in *Δt*. Moreover, the velocities in this equation do not appear at all, i.e., the velocities are not needed to compute the trajectories.

From the Verlet algorithm described above one can obtain the velocities from the formula given below:

$$\boldsymbol{v}(t) = \frac{\boldsymbol{r}(t+\Delta t)+\boldsymbol{r}(t-\Delta t)}{2\Delta t} \tag{2.5}$$

The main disadvantage of this algorithm is that velocities are not directly generated, i.e., positions and velocities are not calculated at the same time step (see eqns (2.4) and (2.5)). However, velocities are needed for estimating the kinetic energy (and hence the total energy), i.e., the calculation of the total energy of the system is one of the most important tests to verify that a MD simulation is proceeding correctly.

To overcome this difficulty, several alternative variants of the Verlet algorithm have been developed, such as the Beeman integration scheme, the Gear predictor-corrector approach, the leap-frog algorithm as well as the velocity Verlet algorithm (see [139]). All of them have their specific advantages and disadvantages [140].

In this thesis, the MD calculations are based on the *velocity Verlet algorithm* [141]. In this algorithm positions, velocities and accelerations at time *t+Δt* are obtained from the same quantities at time *t* in the following way:

$$\boldsymbol{r}(t + \Delta t) = \boldsymbol{r}(t) + \boldsymbol{v}(t)\Delta t + \frac{1}{2}\boldsymbol{a}(t)\Delta t^2 \tag{2.6}$$

$$\boldsymbol{v}\left(t + \frac{\Delta t}{2}\right) = \boldsymbol{v}(t) + \frac{1}{2}\boldsymbol{a}(t)\Delta t \tag{2.7}$$

$$\boldsymbol{a}(t + \Delta t) = -(1/m)\nabla U(\boldsymbol{r}(t + \Delta t)) \tag{2.8}$$

$$\boldsymbol{v}(t + \Delta t) = \boldsymbol{v}\left(t + \frac{\Delta t}{2}\right) + \frac{1}{2}\boldsymbol{a}(t + \Delta t)\Delta t \tag{2.9}$$

With this algorithm we never need to simultaneously store the values at two different times for any one of these quantities. This algorithm shows excellent long-time energy conservation, and allows the calculation of kinetic and potential energy at the same time. Moreover, it shows a reduced error on the velocities compared to the basic Verlet scheme. Hence, it is one the most widely used integration algorithm in MD simulations.

2.3.3 Boundary conditions

In MD simulations the system under investigation is typically composed of 10^2–10^7 atoms. Obviously, this is negligible compared with the number of atoms contained in a macroscopic piece of matter (of the order of 10^{23}). Even the simulation of 1 mole of material (i.e., 6.022×10^{23} atoms) using a simple interatomic potential, would take tens of years or longer. Consequently, MD simulations inherently face a size limitation problem. Moreover, the question arises when we use a (finite size) simulation cell (or simulation box) containing a limited number of atoms: what should we do with the atoms at the borders?

The solution to these problems is determined by the system of interest, and typically consists of applying specific boundary conditions.

Different types of boundary conditions can be formulated depending on the processes to be simulated [139]. *Free boundary conditions* (FBC) can be used when one wants to deal with e.g. a molecule (which can contain hundreds of atoms) or nanocluster in vacuum. FBC may also be used when studying ultrafast processes e.g. fast ion/atom bombardment, as the effect of the boundaries is not important due to the short time-scale of the involved processes.

Reflective boundary conditions (RBC) are applied by simply inverting the velocity components of any particle hitting the wall of the simulation box during some time step.

The most commonly used boundary condition in MD simulations is *periodic boundary conditions* (PBC). They are applied to simulate processes in a bulk material while keeping the number of atoms limited.

The implementation of PBC is as follows. Simulated particles are enclosed in the original box (or computational cell - see green rectangle in Figure 2.1).
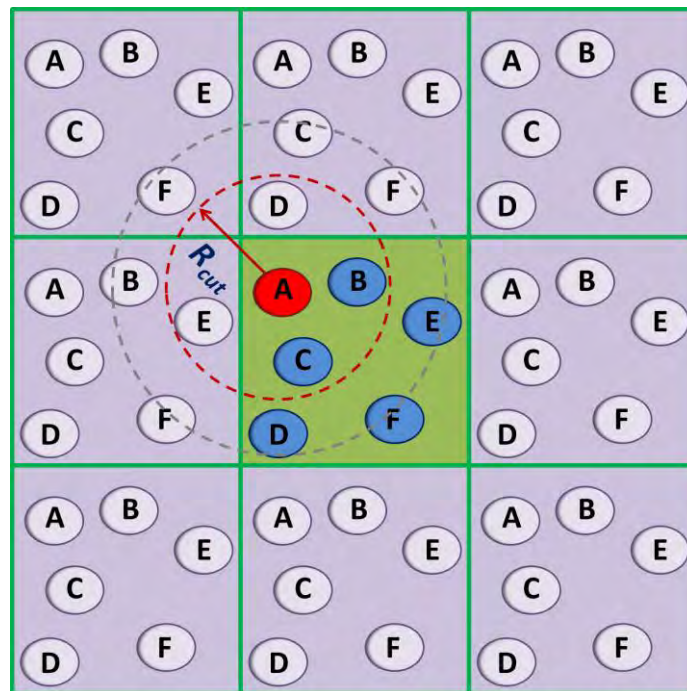
Figure 2.1 *Illustration of periodic boundary conditions and the concept of "minimum image criterion" (see text for explanation)*

This box is surrounded by translated copies of itself (see grey rectangles in Figure 2.1). All of the atoms in the original box, located at positions *r* in the box, are represented in the copied boxes, as an infinite set of particles located at *r* + *la* + *mb* + *nc,* *(l, m, n = -∞,+∞),*where *l, m, n* are integer numbers, and *a*, *b*, *c* the cell vectors. All atoms in the computational cell are thus replicated through space to form an infinite collection. Hence, every atom in the computational cell interacts not only with the other atoms in the simulation box, but also with their images in the nearby boxes (see "images" of the particles **A**–**F** in Figure 2.1). Moreover, if one of the atoms leaves the original box, its replica enters the box from the other side, and thus the number of atoms in the central box is conserved. Thus, by using PBC we are able to mimic an infinite structure and we can deal with the atoms at the boundaries of the simulation box (i.e., elimination of surface effects from the system).

In this work, I used RBC, where the structure (surrounded by vacuum) is positioned in the simulation box larger than the structure itself (see *chapters 3 and 5*), as well as PBC+FBC, in which PBC were used for two directions in the simulation box and FBC for the other direction (see *chapter 4*).

2.3.4 The minimum image criterion

When using PBC one should take into account the following. The computational box size should always be larger than $2R_{cut}$ (see Figure 2.1, red dashed circle), where R_{cut} is the cutoff distance of the interatomic potential. In this work, the cutoff distance of the interatomic potential is 10 Å (see *section 2.4*) and thus, the box size should be greater than 20 Å if we want to use PBC in our simulations (see the size of the water box in *chapter 4*).

This condition is called the *minimum image criterion*. If this criterion is fulfilled, any atom *i* interacts with only one image of any atom *j*, and it does not interact with its own images. So, in Figure 2.1, atom **A** in the original box interacts with **B** and **C** in the same box, as well as with "images" of **D** and **E** from the adjacent boxes. When this criterion is not fulfilled (i.e., the box size is smaller than $2R_{cut}$), an atom *i* may interact with its own images or with multiple images of another atom *j*, which is obviously non-physical (see the area within the grey dashed circle in Figure 2.1).

2.3.5 Thermodynamic ensembles

In MD simulations, besides applying appropriate boundary conditions (see subsection 2.3.3), it is also important to use a suitable simulation ensemble.

According to statistical mechanics, an ensemble is a collection of microstates (configurations) of the system, all having in common a specified set of extensive properties. Physical quantities, in statistical mechanics, are represented by averages over these microstates of the system, distributed in accord with a certain statistical ensemble.

In the natural MD ensemble, the number of particles in the simulation box (*N*), the volume (*V*) of this box containing the system atoms and the total system energy (*E*), remain constant [142]. This ensemble is called the microcanonical ensemble and represents an isolated system. In contrast, a conventional MC simulation probes the canonical (i.e. constant-*NVT*) ensemble, where *T* represents the system temperature.

The microcanonical or *NVE* ensemble is suitable to simulate e.g. a cluster in vacuum. However, it does not allow to control the temperature *T* or the pressure *P* of the system, which can be important for investigating the processes, where *T* and *P* should remain constant.

Therefore, MD simulation techniques have been developed to simulate ensembles other than the microcanonical ensemble. Two frequently used ensembles are the canonical *NVT* ensemble (i.e., a system with constant number of particles *N*, volume *V* and temperature *T*) and the isothermal-isobaric *NPT* ensemble (i.e., a system with constant number of particles *N*, pressure *P* and temperature *T)*. In the *NVT* ensemble, the system is kept in contact with an external heat bath such that energy can be gained from or released to the heat bath. In the *NPT* ensemble, the simulation box size can additionally be reduced or enlarged so as to maintain a target pressure. More information about other ensembles used in MD as well as MC simulations (e.g., grand-canonical ensemble) can be found in [139, 143].

In this work, I use *NVE, NVT* and *NPT* ensembles, employing the Berendsen thermostat and barostat [144] (see *chapter 3*) as well as the recently developed Bussi thermostat [145] (see *chapters 4 and 5*) to control the temperature and pressure.

2.3.6 Thermostat and barostat

Various algorithms exist for controlling the system temperature and pressure, e.g., stochastic coupling methods, such as Andersen [146] and Nosé-Hoover [147, 148]. An overview of thermostat algorithms for MD simulations is given in [149]. Below, I give a brief description about the Barendsen thermo/barostat as well as the Bussi thermostat, which are used in this work. More information can be found in [144, 145].

Berendsen thermostat. The Berendsen thermostat is used to control the system temperature by rescaling the velocities of the atoms in the system [144]. As such, the system is weakly coupled to an external heat bath.

The use of the Berendsen thermostat is simple. Energy is removed or added to the system to maintain a constant temperature. This is accomplished by multiplying the atomic velocities with a scaling factor λ. Thus, new velocities are determined from the current velocities as $\boldsymbol{v}'_i = \lambda \boldsymbol{v}_i$, where λ is defined as:

$$\lambda = \sqrt{1 + \frac{\Delta t}{\tau}\left(\frac{T_{bath}}{T(t)} - 1\right)} \qquad (2.10)$$

here τ is a coupling parameter whose magnitude determines how tightly the bath and the system are coupled together, *Δt* is the time step and T_{bath} is the temperature of the bath. A typical value for Δt/ τ is 0.1 [144]. Note that the Berendsen thermostat does not reproduce any known ensemble.

Berendsen barostat. The Berendsen barostat is applied to control the pressure in the system. In this method, the system is coupled to a "pressure bath" (or a piston), analogous to a temperature bath. The pressure is (on average) maintained at a constant value simply by scaling the volume by a factor λ, which is equivalent to scaling the atomic coordinates by a factor $λ^{1/3}$:

$$λ = 1 - κ\frac{Δt}{τ_P}(P(t) - P_{bath}) \tag{2.11}$$

where P_{bath} is the pressure of the bath, κ is the experimental isothermal compressibility, which is related to the volume as:

$$κ = \frac{1}{k_B T}\frac{\langle V^2\rangle - \langle V\rangle^2}{\langle V^2\rangle} \tag{2.12}$$

In this scheme, the new positions of the atoms can be found as $\boldsymbol{r}'_i = λ^{1/3}\boldsymbol{r}_i$. The instantaneous pressure can be calculated as follows:

$$P(t) = \frac{1}{V(t)}\left(Nk_B T(t) + \frac{1}{D}\langle\sum_{i=1}^{N} r_i(t) \cdot F_i(i)\rangle\right) \tag{2.13}$$

where *D* is the dimensionality of the system.

Bussi thermostat. As described above, in the Berendsen thermostat the velocities are rescaled at each time step in order to enforce the desired temperature (i.e., the total kinetic energy) of the system. However, although the Berendsen thermostat allows control of the simulated system's temperature, it does not generate the true canonical *NVT* ensemble. Recently, a technique was developed by Bussi *et al.* combining the simplicity of the Berendsen thermostat with a correct canonical sampling [145]. The Bussi thermostat is applied in the

same way as the Berendsen thermostat, but the scaling factor is determined using a stochastic procedure:

$$\alpha^2 = e^{-\frac{\Delta t}{\tau}} + \frac{\overline{K}}{N_f K}\left(1 - e^{-\frac{\Delta t}{\tau}}\right)\left(R_1^2 + \sum_{i=2}^{N_f} R_i^2\right) + 2e^{-\frac{\Delta t}{\tau}}R_1\sqrt{\frac{\overline{K}}{N_f K}(1 - e^{-\frac{\Delta t}{\tau}})}$$

(2.14)

where K is the instantenous kinetic energy of the system, $\overline{K}$ the desired kinetic energy (based on T_{set}), N_f the number of degrees of freedom and R_i a Gaussian-distributed random number. τ is a parameter equivalent to the one in the Berendsen formulation, controlling the strength of the coupling (see above).

The two key differences of the Bussi thermostat with the Berendsen thermostat are (a) the thermostat is stochastic (i.e., the scaling factor α not only depends on the system properties, but it is, in fact, sampled from a probability distribution, using random numbers), and (b) it is truly canonical.

It should be mentioned that if MD simulations are intended to capture the dynamics of the system and not necessarily to capture the correct (thermo)dynamics then both Berendsen and Bussi thermostats can be applied. Moreover, recent comparison of the results of adsorption processes using both thermostats have shown no significant differences [150].

2.3.7 Choosing the time step

As mentioned in previous subsections, there are limits on the typical time scales and length scales in MD simulations, and this needs to be taken into account in investigations of the processes and analyzing the results. Simulation runs are typically short (10^3-10^6 MD steps) and correspond to typically a few nanoseconds of real time, and in special cases it can extend to the microsecond regime [151]. Integration algorithms (presented in *subsection 2.3.2*) are all approximate and each has an error associated with them. As mentioned in *subsection 2.3.2*, the Verlet algorithm has a *truncation error* $O(\Delta t^4)$, which is proportional to Δt^4. A second type of errors are *round-off errors* that relate to the finite number of digits used in computer arithmetics and are associated with a

particular implementation of an algorithm. Both errors can be reduced by decreasing the time step (Δt). Otherwise, the total energy of the system in MD simulations will rapidly drift with time when the simulation is integrated by a large time step. Therefore, there is a need to choose the time step as short as possible for numerical stability and accuracy, and as long as possible to avoid inefficient simulation and waste of computational time. Unfortunately, there is no standard condition for evaluating the appropriate value of the time step.

In practice (as a rough rule-of-thumb), the atoms should not move more than 1/20 of the nearest-neighbor distance within one time step and the time step should be chosen according to this criterion [152]. On the other hand, the time step is determined by the fastest motions in the system, i.e., the atomic vibrations. These are typically in the range of several femtoseconds (fs), such that the MD time step is usually in the order of sub-fs to a few fs in order to ensure a stable time integration [153]. The time step is also determined to some extent by the mass of the atoms and the system temperature: lighter elements and higher temperatures require a somewhat shorter time step, whereas heavier elements and lower temperatures allow for a somewhat longer time step. Finally, the time step to use is also determined by the potential energy function. For instance, non-reactive force fields such as AMBER [154, 155] allow for a time step of up to 2 fs, while a reactive force field such as ReaxFF [156] typically requires a time step in the order of 0.25 fs.

In most cases, to validate the correctness of the chosen time step in MD simulations, a typical test of measuring the conservation of total energy E is performed in the microcanonical (*NVE*) ensemble. In other thermodynamic ensembles, such as in the canonical (*NVT*) ensemble, an effective energy $\tilde{H}$ can be used to verify the sampling accuracy and to play a role similar to the total energy in the *NVE* ensemble [145].

Based on above mentioned considerations, in this work, *0.1 fs* (see *chapter 3*) and *0.25 fs* (see *chapters 4 and 5*) were chosen as the time steps.

2.3.8 Interatomic interaction potentials

In this subsection, I mainly focus on the interatomic potentials (available in the literature) that are used in the context of plasma medicine (see *chapter 1, section 1.2*).

In classical MD, forces are taken as the negative derivative of some suitable interatomic interaction potential (also known as the "force field"), which governs all possible atomic interactions. Note that in chemistry, the term force field is used to denote the set of energy functions that describe the atomic interactions, while in physics, the term force field is used to denote the gradient of a scalar potential. Regardless of the common use of these terms, some potentials are invariably referred to in the literature as "force fields", for instance the Reax force field [156], whereas others are usually referred to as "potentials", as for example the Brenner potential [157]. Here, the terms "*force field*" and "*interatomic potential*" are used interchangeably, and the (in)ability of the energy functions to form and break bonds are specifically indicated by the adjectives "reactive" and "non-reactive".

Irrespective of being reactive or not, the force field used should be fairly generic, as e.g. in biological structures a multitude of elements typically needs to be represented. While this is usually not an issue for non-reactive force fields, there are only very few reactive force fields that are sufficiently generic to describe more than a few elemental combinations (see below).

Depending on the process and the desired properties that are being studied, the force field required may either be *reactive* or *non-reactive*. As mentioned above, in a *reactive force field*, chemical bonds may be broken and formed. In this case, the atomic connectivity must thus be recalculated every time step, increasing the computational load of these simulations. Moreover, an accurate description of the chemistry of the system typically requires a rather complex force field, which further increases the computational load. In a *non-reactive force field*, on the other hand, chemical bonds cannot be broken or formed, and the atomic connectivity thus remains fixed throughout the simulation and does not need to be recalculated every integration step. Moreover, the functional form of non-reactive force fields is typically much simpler. These simulations are therefore much faster, but cannot provide much insight in the chemistry. An example of such simulations is electroporation of lipid bilayers by strong electric fields [158, 159].

Non-reactive force fields are generally much faster than reactive force fields, and are capable of very accurately simulating the structure of a biomolecule. This is so because bonds between atoms cannot break and form, and the neighbours for each atom thus remain the same throughout the simulation. In

practice, only the region around the harmonic minimum of the (local) potential energy well needs to be reproduced. The obvious disadvantage is that these force fields cannot describe chemical processes, like bond breaking and formation, in which the atomic connectivity in the system dynamically changes in the course of the simulation.

In contrast to reactive force fields, such non-reactive force fields in the context of biomolecular simulations are most often of the "*united-atom*" type, which means that not all atoms are explicitly represented, but some typical groups of atoms are combined. Most often, the aliphatic hydrogens are combined with their respective carbon atoms into an effective CH_2 particle. As this reduces the total number of particles to be simulated, this technique reduces the computational load of the simulations, and allows to handle much larger systems than is possible in an all-atom description. For example, dipalmitoylphosphatidylcholine (DPPC) contains 130 particles in an all-atom description, but only 50 in the united-atom representation. A closely related alternative to speed up the simulations is by making use of *coarse-grained models*, in which small groups of atoms are treated as larger particles, enabling the access of longer time and length scales than possible via traditional atomistic approaches. In a sense, the united-atom approach is the lowest-level coarse-grained method. The difference essentially lies in the number of particles that is combined: in a united-atom simulation, typically only the atoms in a methylene group or a methyl group are combined, whereas in a coarse-grained simulation entire functional groups or structural units are treated as a single particle, for instance a phosphate group or a choline unit. A dimyristoylphosphatidylcholine (DMPC) molecule containing 118 atoms, for instance, can be represented by 10 coarse-grained particles [160].

In the context of plasma medicine, mainly two families of force fields have been used (although in a variety of different parametrizations), namely the *OPLS* force field ("Optimized Potentials for Liquid Simulations") [161, 162], and the *GROMOS* force field (GROningen MOlecular Simulation") [163]. Another force field that is often used was developed by Berger *et al.*, which is essentially a combination of one of the GROMOS parametrizations for bonded interactions, a modified version of the united-atom OPLS force field parameters for van der Waals interactions and atomic partial charges from ab initio calculations [164]. Descriptions of these force fields are given in [34].

It should also be noted that there are other families of force fields, such as AMBER [154, 155], CHARMM [165], which are widely used for larger biomolecules (proteins, polymers); their functional form is simpler and parameters are typically determined by quantum chemical calculations combined with thermophysical and phase coexistence data [166]. Moreover, state-of-the art biological MD programs such as NAMD [167, 168] and GROMACS [169, 170] are also used to investigate large biological structures, applying a variety of algorithms for parallelization of MD.

Reactive force fields. The currently available generic reactive force fields are the embedded atom method (*EAM*) [171] and modified EAM (*MEAM*) [172], the *Finnis-Sinclair* potential [173], the *COMB* potential [174] and the Reax force field (*ReaxFF*) [156], and to a lesser extent a variety of other potentials, including the *Vashishta* [175], *Tersoff* [176] and *Brenner* potentials [157]. The Finnis-Sinclair, EAM and MEAM were (originally) developed for metals, and have so far not been used in the context of plasma medicine. The COMB potential is a very recent development, intended primarily to study metal oxide systems. A parameterization that would enable typical biochemical molecules (including C, O, N and H atoms, for instance) is currently not yet available. The Vashishta potentials describe various Si-based materials, but again a parameterization relevant for biomolecules is not available. Therefore, here, these potentials will not be described further, and focus will be only on the ReaxFF and the Brenner potential, both of which have been used in the context of reactive MD simulations for plasma medicine (see *chapters 3-5*, as well as [122, 124, 125]).

The *REBO (*"Reactive empirical Bond Order"*) potential* or Brenner potential has been used to simulate reactive events in the context of plasma medicine, although it was originally developed for hydrocarbons [157, 177]. It has subsequently been extended to describe C/H/O compounds by Sinnott *et al.* [178]. The REBO potential is based on the bond order concept, and its functional form can be written as follows:

$$E_{system} = \sum_i \sum_{j>i} V_{rep}(r_{ij}) - \bar{b}_{ij} V_{att}(r_{ij}) \tag{2.15}$$

where $V_{rep}(r_{ij})$ and $V_{att}(r_{ij})$ are repulsive and attractive pair potentials, respectively, and $\bar{b}_{ij}$ is the bond order function, which contains all many-body

effects. The bond order function is a rather complex term; a detailed description is provided in [177]. In the context of plasma medicine, the REBO potential has been applied to study the interaction of energetic ions with lipid molecules [122].

An important advantage of the Brenner potential over ReaxFF (see below) is its (relative) simplicity, greatly reducing the computation time. Indeed, the Brenner potential only requires around 100 parameters to describe all possible interactions in C/H compounds, while the ReaxFF requires around 150 parameters. Moreover, a more simple functional form has the additional advantage of being more transparent than a more complex form. On the other hand, the ReaxFF is superior to Brenner in that it also describes Coulomb interactions and allows for polarization, and in contrast to the Brenner potential, all terms (except the Coulomb and van der Waals terms) are made bond order dependent. Moreover, it is parametrized for a much wider range of materials.

In this work, reactive MD simulations were carried out using the ReaxFF potential (see *chapters 3-5*). A detailed description of ReaxFF is given below in *section 2.4*.

2.4 ReaxFF potential

2.4.1 Overview

The *Reax force field* (or ReaxFF) is a classical force field, which was originally developed for hydrocarbons [156], but soon expanded to a variety of other elements. It is currently one of the most widely parameterized reactive force fields available.

ReaxFF has now been successfully applied to describe nearly half of the periodic table of the elements and their compounds, including hydrocarbons [156, 179], metals and metal catalyzed reactions [180, 181], metal oxides [182], metal hydrides [183] and silicon and silicon dioxide [140, 184-188]. Recently, it has also been used for organic molecules, such as glycine [189-191], as well as for complex molecules, such as DNA [124].

ReaxFF is capable of describing both covalent and ionic bonds, as well as the entire range of intermediate interactions (see *subsection 2.4.2*).

ReaxFF parameters are optimized to obtain good general agreement with quantum mechanical (QM) calculations for reaction energies, barriers and structures (in that order of importance). It accurately simulates bond breaking and bond formation processes, commonly approaching QM accuracy. Thus, it serves as a link between QM and empirical (non-reactive) force fields [192].

2.4.2 Potential functions and force field parameters

Overall system energy. The total system energy in ReaxFF is a sum of several partial energy terms, including the bond (E_{bond}) and lone pair (E_{lp}) energy terms, under- (E_{under}) and over- (E_{over}) coordination corrections, valence (E_{val}) and torsion (E_{tors}) angle terms, penalty energy (E_{pen}), conjugation (E_{conj}), hydrogen bonding (E_{Hbond}), Coulomb ($E_{Coulomb}$) and van der Waals ($E_{vdWaals}$) interactions, and some other (E_{other}) additional correction terms (e.g., three body conjugation, correction for C_2, see [179]) for specific binding topologies. The total energy can thus be expressed as:

$$
\begin{aligned}
E_{system} = E_{bond} + E_{lp} + E_{over} + E_{under} + E_{val} + E_{pen}+ \\
E_{tors} + E_{conj} + E_{Hbond} + E_{vdWaals} + E_{Coulomb}
\end{aligned}
\tag{2.16}
$$

All these energy terms are composed of rather complex functions containing a number of coefficients and the details of these energy terms are given below. Note that all parameters (used in formulae below), which are not explained explicitly, can be found in [156, 179, 193, 194].

Bond order and Bond energy. ReaxFF is based on the bond order/bond distance relationship. This concept was earlier applied to carbon and silicon by Tersoff [176] and to hydrocarbons by Brenner [157]. In ReaxFF, the (uncorrected) bond order for each bond is summed from σ, π and $\pi\pi$ contributions to the bond, and is calculated from the instantaneous interatomic distance:

$$BO'_{ij} = BO'^{\sigma}_{ij} + BO'^{\pi}_{ij} + BO'^{\pi\pi}_{ij} =$$
$$exp\left[p_{bo,1}\left(\frac{r_{ij}}{r_0^{\sigma}}\right)^{p_{bo,2}}\right] + exp\left[p_{bo,3}\left(\frac{r_{ij}}{r_0^{\pi}}\right)^{p_{bo,4}}\right] + exp\left[p_{bo,5}\left(\frac{r_{ij}}{r_0^{\pi\pi}}\right)^{p_{bo,6}}\right]$$

(2.17)

In this expression, r_{ij} is the scalar distance between atoms i and j. r_0^{σ}, r_0^{π} and $r_0^{\pi\pi}$ are the covalent bond radii of σ, π- and double π-bonds between i and j, and $p_{bo,1}$ to $p_{bo,6}$ are fitting parameters. Energy penalties related to overcoordination and stabilization energies related to undercoordination, both of which depend on the local bonding topology of atoms i and j, are then used to enforce the correct bond order.

The corrected bond orders (i.e., BO_{ij}, which are derived from the uncorrected bond order BO'_{ij}; cf. above) are then used to evaluate the bond energy involving a pair of atoms i and j using the relation:

$$E_{bond} = -D_e^{\sigma} \cdot BO_{ij}^{\sigma} \cdot exp\left[p_{be,1}\left(1 - \left(BO_{ij}^{\sigma}\right)^{p_{be,2}}\right)\right] - D_e^{\pi} \cdot BO_{ij}^{\pi} - D_e^{\pi\pi} \cdot BO_{ij}^{\pi\pi}$$

(2.18)

where D_e^{σ}, D_e^{π} and $D_e^{\pi\pi}$ are the dissociation energies of σ, π- and double π-bonds while $p_{be,1}$ and $p_{be,2}$ are the bond energy parameters (i.e., fitting parameters of the force field). Equation (2.18) ensures that the energy and force associated with a bond smoothly go to zero as the bond breaks.

Lone pair energy. This energy term accounts for unpaired electrons of an atom using the following equation:

$$E_{lp} = \frac{p_{lp} \cdot \Delta_i^{lp}}{1 + exp\left(-75 \cdot \Delta_i^{lp}\right)} \tag{2.19}$$

where $\Delta_i^{lp} = n_{opt}^{lp} - n_i^{lp}$ corresponds to the number of unpaired electrons and p_{lp} is a lone pair energy parameter (i.e., fitting parameter of the force field). Lone electron pairs on heteroatoms such as oxygen and nitrogen can affect dramatically the response of these atoms to over- and undercoordination.

Overcoordination energy. For an overcoordinated atom ($\Delta_i > 0$), the following equation imposes an energy penalty on the system:

$$E_{over} = \frac{\alpha}{\Delta_i^{lpcorr} + Val_i} \cdot \Delta_i^{lpcorr} \cdot \left[\frac{1}{1 + exp(\lambda_6) \cdot \Delta_i^{lpcorr}}\right] \tag{2.20}$$

where

$$\alpha = \sum_{j=1}^{nbond} p_{be,3} BO_{ij} \tag{2.20a}$$

$$\Delta_i^{lpcorr} = \beta - \Delta_i^{lp} \cdot \frac{1}{1 + \lambda_6 \cdot exp(\lambda_{32} \cdot \gamma)} \tag{2.20b}$$

$$\beta = \sum_{j=1}^{nbond} BO_{ij} - Val_i \tag{2.20c}$$

$$\gamma = \sum_{j=1}^{neighbors(j)} \left(\Delta_j - \Delta_j^{lp}\right) BO_{ij}^{\pi} \tag{2.20d}$$

Here, Val_i is the number of bonding electrons of the atom, which binds to other atoms. Furthermore, $p_{be,3}$, λ_6 and λ_{32} are fitting parameters of the force field. This also applies to the other λ_i ($i = 1 - 34$), which occur in the following formulas. All these parameters can be found in [156, 194].

Undercoordination energy. For undercoordinated atoms ($\Delta_i < 0$), it is important to account for the resonance of π-electrons between the undercoordinated atom and its neighbors. The energy penalty for undercoordination around atom i is expressed as:

$$E_{under} = -p_{under} \cdot \frac{1 - exp\left(\lambda_7 \cdot \Delta_i^{lpcorr}\right)}{1 + exp\left(-\lambda_8 \cdot \Delta_i^{lpcorr}\right)} \cdot f_6(i, \lambda_9, \lambda_{10}) \tag{2.21}$$

where

$$f_6(i, \lambda_9, \lambda_{10}) = \left(1 + \lambda_9 \cdot exp\left(\lambda_9 \cdot \sum_{j=1}^{neighbors(i)} (\Delta_j - \Delta_j^{lp}) \cdot \left(BO_{ij}^\pi + BO_{ij}^{\pi\pi}\right)\right)\right)^{-1} \tag{2.21a}$$

Valence angle energy. The energy associated with vibration around the optimum valence angle between atoms i, j and k is calculated as follows:

$$E_{val} = f_7(BO_{ij}) \cdot f_7(BO_{jk}) \cdot f_8(\Delta_j) \cdot \left\{k_a - k_a \cdot exp\left[-k_b(\Theta_0 - \Theta_{ijk})^2\right]\right\} \tag{2.22}$$

where

$$f_7(BO) = 1 - exp(-\lambda_{11} BO^{\lambda_{12}}) \tag{2.22a}$$

$$f_8(\Delta_j) = \frac{2 + exp(-\lambda_{13} \cdot \Delta_j)}{1 + exp(-\lambda_{13} \cdot \Delta_j) + (p_{v,1} \cdot \Delta_j)} \cdot$$
$$\left[\lambda_{14} - (\lambda_{14} - 1) \cdot \frac{2 + exp(\lambda_{15} \cdot \Delta_j)}{1 + exp(\lambda_{15} \cdot \Delta_j) + exp(-p_{v,2} \cdot \Delta_j)}\right] \tag{2.22b}$$

$$SBO = 1 - \left[\prod_{n=1}^{neighbors(j)} exp\left(-BO_{jn}^8\right)\right] \cdot$$
$$\left(\Delta_j - \lambda_{34}\Delta_j^{lp} + \sum_{n=1}^{neighbors(j)} BO_{jn,\pi}\right) \tag{2.22c}$$

$$\begin{aligned}
&SBO2 = 0 &&\text{if } SBO \leq 0 \\
&SBO2 = SBO^{\lambda_{17}} &&\text{if } 0 < SBO < 1 \\
&SBO2 = 2 - (2 - SBO)^{\lambda_{17}} &&\text{if } 1 < SBO < 2 \\
&SBO2 = 2 &&\text{if } SBO > 2
\end{aligned}$$

$$\Theta_0 = \pi - \Theta_{0,0}\{1 - exp[-\lambda_{18}(2 - SBO2)]\} \qquad (2.22d)$$

The equilibrium angle Θ_0 for Θ_{ijk} depends on the sum of π-bond orders (*SBO*) around the central atom *j*. Thus, the equilibrium angle changes from around 109.47^0 for sp^3 hybridization (π-bond=0) to 120^0 for sp^2 hybridization (π-bond=1) to 180^0 for sp hybridization (π-bond=2) based on the geometry of the central atom *j* and its neighbors. It is important to note that the energy contribution from valence angle terms goes to zero as the bond orders in the valence angle goes to zero.

Penalty energy. To describe systems (or to reproduce stability of systems) with two double bonds sharing an atom in a valence angle, like allene, an additional energy penalty is imposed for such systems:

$$E_{pen} = \lambda_{19} \cdot f_9(\Delta_j) \cdot exp\left[-\lambda_{20} \cdot (BO_{ij} - 2)^2\right] \cdot exp\left[\lambda_{20} \cdot (BO_{jk} - 2)^2\right]$$

$$(2.23)$$

where

$$f_9(\Delta_j) = \frac{2 + exp(-\lambda_{21} \cdot \Delta_j)}{1 + exp(-\lambda_{21} \cdot \Delta_j) + exp(\lambda_{22} \cdot \Delta_j)} \qquad (2.23a)$$

Torsion angle energy. The energy associated with a torsion angle ω_{ijkl} (i.e., the middle bond of three bonds formed by four atoms maintaining a certain angle) is computed as

$$E_{tors} = f_{10}(BO_{ij}, BO_{jk}, BO_{kl}) \cdot sin\Theta_{ijk} \cdot sin\Theta_{jkl} \cdot$$
$$\left[\frac{1}{2}V_2 \cdot exp\left\{p_l\left(BO_{jk} - 3 + f_{11}(\Delta_j, \Delta_k)\right)^2\right\} \cdot \\ (1 - cos2\omega_{ijkl}) + \frac{1}{2}V_3 \cdot (1 + cos3\omega_{ijkl})\right] \qquad (2.24)$$

where

$$f_{10}(BO_{ij}, BO_{jk}, BO_{kl}) = \\ \left[1 - exp(-\lambda_{23} \cdot BO_{ij})\right] \cdot \left[1 - exp(-\lambda_{23} \cdot BO_{jk})\right] \cdot \\ \left[1 - exp(-\lambda_{23} \cdot BO_{kl})\right] \qquad (2.24a)$$

$$f_{11}(\Delta_j, \Delta_k) = \frac{2 + exp(-\lambda_{24} \cdot (\Delta_j + \Delta_k))}{1 + ex\,p[-\lambda_{24} \cdot (\Delta_j + \Delta_k)] + ex\,p[\lambda_{25} \cdot (\Delta_j + \Delta_k)]} \qquad (2.24b)$$

As in the valence energy term, the torsional contribution from a four-body structure should vanish as any of its bonds dissociates.

Conjugation energy. Equations (2.25) and (2.25a) describe the contribution of the conjugation effects to the molecular energy. A conjugated system is a system of connected π-orbitals with delocalized electrons.

$$E_{conj} = f_{12}(BO_{ij}, BO_{jk}, BO_{kl}) \cdot \lambda_{26} \cdot [1 + (cos^2 \omega_{ijkl} - 1)] \cdot sin\Theta_{ijk} \cdot sin\Theta_{jkl}$$

$$(2.25)$$

where

$$f_{12}(BO_{ij}, BO_{jk}, BO_{kl}) = exp[-\lambda_{27} \cdot (BO_{ij} - 1.5)^2] \cdot$$
$$exp[-\lambda_{27} \cdot (BO_{jk} - 1.5)^2] \cdot$$
$$exp[-\lambda_{27} \cdot (BO_{kl} - 1.5)^2] \qquad (2.25a)$$

As shown in the equation, the conjugation energy has a maximal contribution to the total system energy when successive bonds have bond-order values of 1.5 (as in benzene and other aromatics).

Hydrogen bond interactions. Description of the bond-order dependent hydrogen bond term for a X-H—Z system as incorporated in ReaxFF is given in equation (2.26):

$$E_{Hbond} = p_{hb,1} \cdot [1 - \exp(p_{hb,2} \cdot BO_{XH})] \cdot$$
$$exp\left[p_{hb,3}\left(\frac{r_{hb}^o}{r_{HZ}} + \frac{r_{HZ}}{r_{hb}^o} - 2\right)\right] \cdot sin^8\left(\frac{\Theta_{XHZ}}{2}\right) \qquad (2.26)$$

where Θ_{XHZ} is the hydrogen bond angle, i.e., angle between atoms X, H (hydrogen) and Z in the system.

ReaxFF employs a *Taper correction* [195] in order to avoid energy discontinuities when charged species move in and out of the non-bonded cutoff radius. Each non-bonded energy and derivative is multiplied by a Taper-term (see Van der Waals and Coulomb energy terms, below), which is taken from a distance-dependent 7th order polynomial:

$$Tap(r_{ij}) = \sum_{m=0}^{7} Tap_m \cdot r_{ij}^m \tag{2.27}$$

where

$$
\begin{aligned}
Tap_0 &= \quad 1 \\
Tap_1 &= \quad 0 \\
Tap_2 &= \quad 0 \\
Tap_3 &= \quad 0 \\
Tap_4 &= -35 \cdot r_{cut}^{-4} \\
Tap_5 &= \quad 84 \cdot r_{cut}^{-5} \\
Tap_6 &= -70 \cdot r_{cut}^{-6} \\
Tap_7 &= \quad 20 \cdot r_{cut}^{-7}
\end{aligned}
\tag{2.27a}
$$

Here, r_{cut} is the non-bonded cutoff radius, which is typically set to 10 Å in ReaxFF.

Van der Waals interactions. In addition to the bonded interactions described above, there are repulsive interactions between very close atoms owing to Pauli's exclusion principle and long range attractive forces due to dispersion. These pairwise interactions include the *van der Waals* and *Coulomb* forces which are evaluated for *every* atom pair, irrespective of the geometry and instantaneous connectivity. To account for these non-bonded interactions, ReaxFF uses a distance-corrected Morse potential including Taper terms:

$$
E_{vdWaals} = \\
Tap(r_{ij}) \cdot D_{ij} \cdot \left\{ exp\left[\alpha_{ij} \cdot (1 - \frac{f_{13}(r_{ij})}{r_{vdW}}) \right] - 2 \cdot exp\left[0.5\alpha_{ij} \cdot (1 - \frac{f_{13}(r_{ij})}{r_{vdW}}) \right] \right\}
$$

$$\tag{2.28}$$

where

$$f_{13}(r_{ij}) = [r_{ij}^{\lambda_{28}} + \left(\frac{1}{\gamma_\omega}\right)^{\lambda_{28}}]^{1/\lambda_{28}} \tag{2.28a}$$

Coulomb interactions. As with the van der Waals interactions, Coulomb interactions between all atom pairs are also taken into account in ReaxFF:

$$E_{Coulomb} = C \cdot Tap(r_{ij}) \cdot \frac{q_i \cdot q_j}{\left[r_{ij}^3 + (1/\gamma_{ij})^3\right]^{1/3}} \tag{2.29}$$

The electronegativity equalization method (*EEM*) [196, 197] is used to calculate atomic charge distributions based on geometry and connectivity.

Depending on the system studied in a Reax-based MD simulation, some of the energy terms in ReaxFF (e.g., conjugation, penalty and torsion energies) can be neglected. Therefore, these energy contributions could be removed (or excluded) from the force field in order to speed up the computational time. For instance, torsion energy is of no importance in metals, whereas this energy term should be taken into account for biomolecular systems.

Force field parameters. In this work, I used the force field parameters developed by Rahaman *et al.* [189]. This force field was developed for the glycine/water system containing C/H/O/N atoms. A training set for the ReaxFF hydrocarbon potential was augmented with several glycine conformers and glycine-water complexes. Parameters of the force field were optimized to reproduce the quantum mechanically derived energies of the species in the training set. The optimized force field could accurately describe the properties of gas-phase glycine. Moreover, the effect of solvation on the conformational distribution of glycine was also investigated in [189].

Using Rahaman's force field parameters I investigated the interaction of O_x as well as H_xO_y with peptidoglycan (PG) that is composed of some saccharides and amino acids (see *chapter 3*), in which the structures of its parts (i.e., amino acids) are close to the structure of glycine. All bond lengths (e.g., C–C, C–O, C–N) in PG were correctly described by this force field. However, in my further investigations with water as a model system (see *chapter 4*), it was found that this force field does not accurately describe reactions of ozone and reactive

nitrogen species (RNS, see *chapter 1, subsection 1.2.5*) with water molecules. Therefore, further developments/improvements to this force field need to be addressed.

However, it should be noted that nowadays the Rahaman's force field parameters are under development and more than 500 molecular systems, including all the amino acids and some short peptide structures were already included to the training set and have been investigated by means of quantum mechanical calculations [190, 191].

I also studied the destruction processes of lipid A by plasma species (see *chapter 5*). This structure consists of the elements C, H, O, N, and P. Phosphorus, however, is not explicitly included in Rahaman's force field parameters. To address this problem, I combined two different force fields in this investigation, i.e., the parameters for the C/H/O/N elements are obtained from [189], which were developed by Rahaman *et al.* for the glycine/water system, whereas the P parameters are adopted from [124] (see *chapter 5*).

The force field parameters used in this work can be found in *Appendix*.

2.5 Reax code – reactive MD code

In this work, to investigate the interaction processes of plasma species with biochemically relevant structures (see *chapters 3-5*), I employ the original, non-commercial Reax code developed by Prof. A. C. T. van Duin. The original version of the code is written in Fortran 77. This code allows for reactive MD simulations on systems consisting of more than 1000 atoms (see water system in *chapter 4*). However, parallel ReaxFF versions also exist (see e.g., PuReMD [198], LAMMPS [199, 200] and ADF [201]) that are able to handle more than million atoms [202].

The code can be subdivided in six parts: reac.f, poten.f, ffopt.f, vibra.f, blas.f and shanno.f. The general MD routine is contained in *reac.f*. In *poten.f*, the actual potential energy contributions are calculated. Force field optimization is done in *ffopt.f*. BLAS (Basic Linear Algebra Subprograms) routines are provided in the *blas.f*. *Vibra.f* is included in the code for calculating vibrational frequencies. Furthermore, both the conjugate gradient and the steepest descent energy minimization methods are also included in the code and contained in

shanno.f. Program parameters are defined in *cbka.blk*. A more detailed description of the code and its features can be found in the *ReaxFF User Manual* written by Prof. A. C. T. van Duin in 2002 [203].

Chapter 3

Plasma induced destruction of peptidoglycan

(Investigation of gram-positive bacteria)

The results presented in this chapter were published in:

Yusupov M, Neyts E C, Khalilov U, Snoeckx R, van Duin A C T and Bogaerts A 2012 Atomic scale simulations of plasma species interacting with bacterial cell walls *New J. Phys.* **14** 093043

Yusupov M, Bogaerts A, Huygh S, Snoeckx R, van Duin A C T and Neyts E C 2013 Plasma-induced destruction of bacterial cell wall components: a reactive molecular dynamics simulation *J. Phys. Chem. C* **117** 5993-5998

3.1 Introduction

In this chapter, the interaction of various reactive oxygen plasma species, which were previously identified as being biomedically important [5, 29, 204-206], with bacterial peptidoglycan (PG) is studied. PG is the outer part of the cell wall of gram-positive bacteria such as *Staphylococcus aureus* (see *chapter 1, section 1.2*). It is used as a model system for plasma - bacteria interactions. For this purpose, reactive MD simulations based on the ReaxFF potential are carried out [156], using the ReaxFF glycine-force field, as developed by Rahaman *et al.* [189]. In this chapter I present the results of two different studies. After a description of the structure of PG (in *section 3.2*) and the computational details (in *section 3.3*), I will describe in *section 3.4* the interaction of O, O_2 and O_3 with PG. Subsequently, in *section 3.5* I will describe the interaction of OH, H_2O_2, and H_2O molecules with PG. Conclusions will be given in *section 3.6*.

3.2 Structure of peptidoglycan

As mentioned in *chapter 1, section 1.2*, PG is an important component of the bacterial cell wall. It forms a mesh-like layer composing the cell wall and serves as a protective barrier in bacteria. The chemical structure of PG can be found in [98, 207, 208].

A schematic picture of the PG structure is presented in Figure 3.1. It is assembled from repeating units consisting of a disaccharide, a stem, and a bridge. The disaccharide is composed of β(1-4) linked N-acetylglucosamine and N-acetylmuramic acid (GlcNAc-MurNAc), the stem is the pentapeptide L-alanine-D-*iso*-glutamine-L-lysine-D-alanine-D-alanine   (L-Ala$_1$-D-*iso*-Gln$_2$-L-Lys$_3$-D-Ala$_4$-D-Ala$_5$), and the bridge is a pentaglycine (Gly$_1$-Gly$_2$-Gly$_3$-Gly$_4$-Gly$_5$) interpeptide. The pentaglycine bridge, branching off the ε-amino group of the L-Lys of the stem peptide, connects one PG chain to the D-Ala$_4$ of a neighboring chain (Figure 3.1). It is important to note that this composition is often found in nascent PG, whereas the last (fifth) D-Ala$_5$ residue is lost in the mature macromolecule [95]. Hence, in this work, a tetrapeptide stem is assumed instead of a pentapeptide stem (see Figure 3.1).
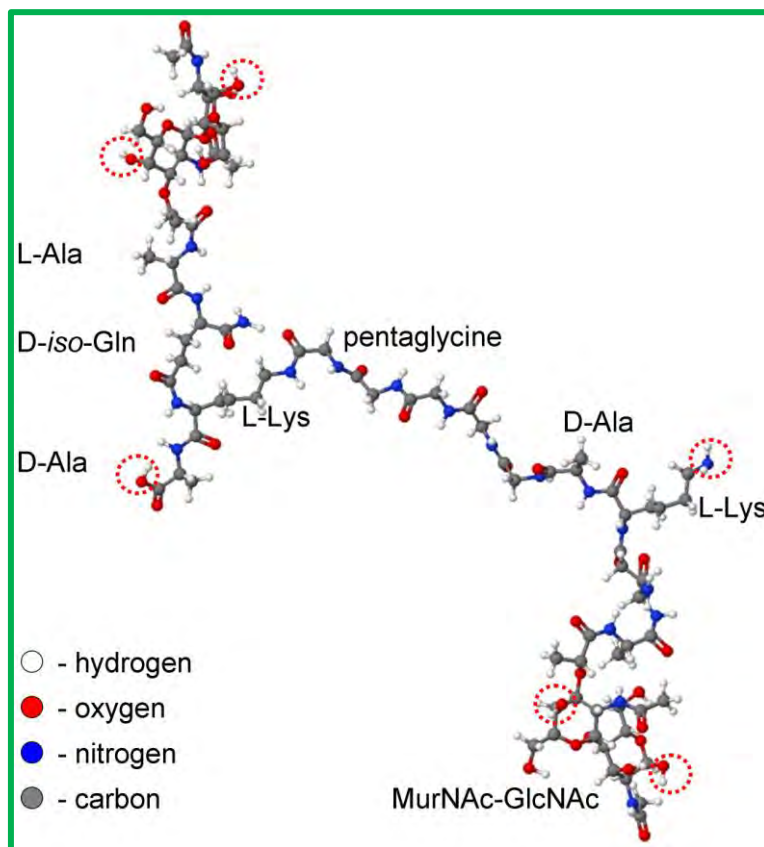
Figure 3.1   *Schematic representation of the PG structure. Fixed atoms are indicated by red dashed circles. The color legend applies also to all the other similar figures below.*

Unfortunately, the exact three-dimensional structure (or tertiary structure) of the PG is still unclear and remains elusive, although many experimental investigations have been performed to define the chemical structure and to study the physical properties of the PG. One of the reasons for this is that it is not possible to distinguish the strands and peptides with conventional electron microscopy due to the similarity in dimensions of these structures and the occurring artifacts of this technique [96, 209]. However, various experimental studies have partially characterized the PG structure (see e.g. [207]). Moreover, based on these experimental studies, several models have been proposed for the three-dimensional structure of the PG, such as the vertical scaffold and the horizontal layered models ([95-97, 209-211]). However, these models can explain only certain properties of PG.

In this work, the PG structure is modelled as consisting of only two disaccharides with tetrapeptide stems (see Figure 3.1, left and right sides), connected with one pentaglycine interpeptide (see Figure 3.1, center). With this

minimal construction we are able to take into account all possible atomic bonds in the PG structure.

It is clear from Figure 3.1 that the most important bonds in the PG structure are C–C, C–N and C–O. As far as the structural integrity of the PG is concerned, the C–O bonds are of importance only in disaccharides (i.e. in MurNAc–GlcNAc, see Figure 3.1). If these C–O bonds or any of the C–C or C–N bonds break, this will lead to the destruction of the PG. Note that there are also C–O bonds in other parts of the PG, but they are not taken into account as they are less important in damaging the PG structure.

3.3 Computational details

In our MD simulations, the PG structure is placed in a box with dimensions ~75 Å × 88 Å × 51 Å. We do not apply periodic boundary conditions (PBC) in any direction as no infinite surface is needed in the simulations. Moreover, we apply reflective boundary conditions (RBC) for the impinging plasma species (see below) but not for PG itself. A few atoms in the PG structure are fixed to keep it from drifting. The fixed atoms are chosen such that they are positioned at the periodically repeating parts of the PG structure, i.e. O and H atoms in D-Ala$_4$, MurNAc and GlcNAc, and two H atoms in L-Lys (see Figure 3.1, red dashed circles).

Prior to the particle impacts, the structure is equilibrated at room temperature (i.e., 300 K) as follows. First, the structure is thermalized in the isothermal-isobaric ensemble (i.e., *NPT* dynamics) for 100 ps to equilibrate the temperature of the system and to obtain a structure at zero stress. The obtained structure is subsequently equilibrated in the *NVT* ensemble using the Berendsen heat bath [144] for 40 ps. Finally, the resulting structure is relaxed in the microcanonical ensemble corresponding to *NVE* dynamics for 20 ps. The temperature relaxation constant is set to 0.1 ps in all temperature controlled simulations, i.e. during the thermalization, as well as during the particle impact simulations. In all simulations, a time step of 0.1 fs is used.

In all simulations, the impacts of the plasma species are performed as follows. Ten incident particles (e.g. ten OH radicals) are randomly positioned at

a minimum distance of 10 Å around the PG structure and also from each other. This distance ensures that there is initially no interaction between the plasma species and the PG structure. The initial energy of the impinging plasma species corresponds to room temperature and their velocity directions are chosen randomly. To study all possible damaging mechanisms of the PG and to obtain statistically valid results for bond-breaking processes, 50 runs are performed for each plasma species (i.e. for O, O_2, O_3, OH, H_2O_2 and H_2O). Every simulation trajectory lasts 300 ps, corresponding to 3×10^6 iterations. This time is long enough to obtain a chemically destroyed PG structure, at least if a critical bond in the structure is broken (see below). Thus, at the end of the simulation all plasma species interacted with the structure, possibly resulting in the breaking of various bonds as described below in *sections 3.4 and 3.5*.

3.4 Interaction of oxygen plasma species with peptidoglycan

First it should be mentioned that no bond cleavage events are observed in the case of O_2 impacts. These molecules are found to have only weak attractive non-bonded interactions with the PG structure. Therefore, O_2 molecules are not considered further in this section.

In the following studies, examples of the bond-breaking mechanisms will only be shown for oxygen atoms, although similar mechanisms have also been observed for O_3 molecules. Note that in the case of O_3, the first reaction to occur is invariably with hydrogen from the PG, resulting in the formation of an O_2 molecule and an OH radical. It has to be mentioned here that in our later investigation (see *chapter 4*) we found that O_3 molecules might not be properly described by ReaxFF. Given the ReaxFF-description of O_3 molecules, the results shown in Table 3.1 for O_3 molecules (i.e., the fraction of dissociation events, see below) can quantitatively be different from those that would result from a more accurate O_3 description, but we expect that the qualitative trends remain the same.

3.4.1 Dissociation of C–N bonds

One of the cleavage mechanisms of C–N bonds is presented in Figure 3.2, where D-Ala, connected to the pentaglycine bridge, is being broken by an impinging oxygen atom (see Figure 3.1, right-hand side). It is clear from Figure 3.2(a) that oxygen (encircled by the red dashed line) is reacting with hydrogen initially bound with carbon, i.e. a hydrogen-abstraction reaction is taking place.
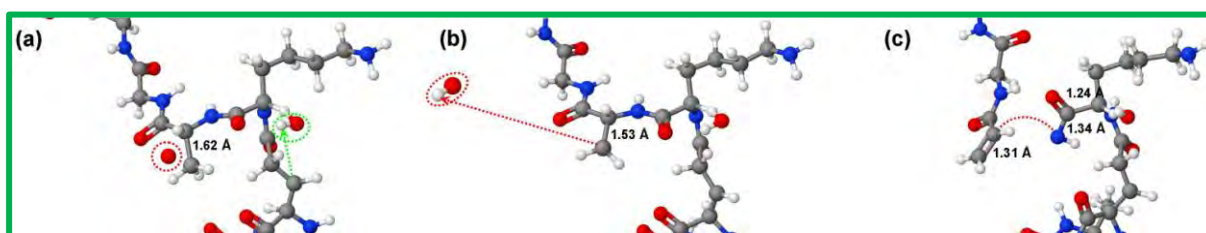
Figure 3.2   Snapshots from our MD simulations, showing the interaction of an oxygen atom with D-Ala, leading to the cleavage of a C–N bond. (a) Oxygen, shown in red dashed circle, reacts with hydrogen (t = 15.6 ps). (b) Hydrogen abstraction takes place and results in a decrease in the C–C bond length (t = 16.2 ps). (c) Cleavage of the C–N bond (indicated by the red dashed line) and creation of the double C–C bond (t = 30.6 ps). Note that there is another oxygen atom (shown by the dashed green circle, see (a)) that abstracts a hydrogen atom from another carbon atom, resulting in the formation of a secondary alkyl radical.

Note that there is another oxygen (shown by the dashed green circle) that has already abstracted a hydrogen atom from another carbon atom. As we concentrate on the breaking of C–N bonds in this section, an explanation for this process will be given later. As shown in Figure 3.2(b), the distance between the C–C bonds starts to decrease after the hydrogen-abstraction reaction (cf. bond distances in Figure 3.2(a) and (b)). Because of the hydrogen abstraction, a primary alkyl radical is generated in D-Ala. Since this radical is not stable [212], a double C–C bond is created by homolytic cleavage of the C–N bond, with the formation of a resonance-stabilized amide radical (see Figure 3.2(c)). Note that the resonance-stabilized amide radical is more stable than the primary radical, which could therefore be the driving force for the C–N bond breaking process. It should be noted that also a secondary alkyl radical is created after the hydrogen abstraction (see dashed green circle in Figure 3.2(a)). Since secondary alkyl radicals are more stable than primary alkyl radicals, no bond breaking takes place in this case.
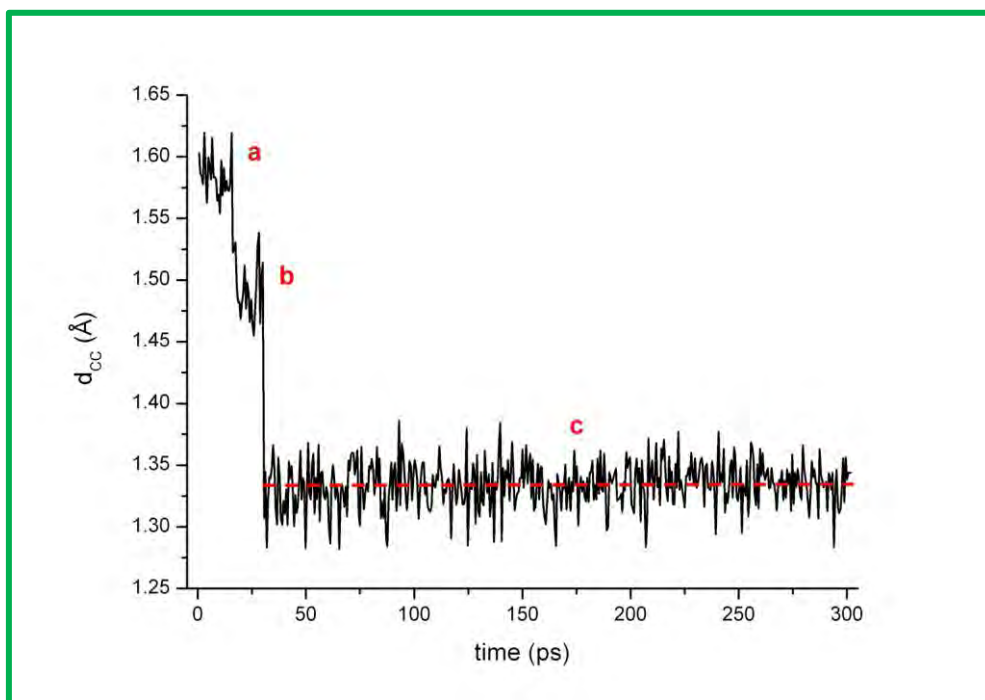
Figure 3.3 *Time evolution of the C–C bond length. The **a**, **b** and **c** labels correspond to (a),*
(b) and (c) in Figure 3.2, respectively. After 30.6 ps, the average distance between the carbon
atoms remains constant until the end of the simulation. The average C–C bond length is about
1.33 Å, which is typical for a double C–C bond (see red dashed line).

After dissociation of the C–N bond, the two carbon atoms form a double
bond (see Figure 3.2(c)). The average C–C bond length does not change further
until the end of the simulation and is found to be about 1.33 Å, i.e. a typical
value for the bond length of a double C–C bond [212], as shown in Figure 3.3
(see red dashed line).

In Figure 3.4 the time evolution of the average number of C–N bonds upon
impact of either O atoms or O_3 molecules is shown. Note that the average
number of C–N, C–C and C–O bonds is calculated from 50 independent runs for
each incident species. It is clear from Figure 3.4 that the average number of C–N
bonds decreases during the simulation, i.e., the plasma species are effective in
dissociating the C–N bonds in the PG structure. It is also obvious from Figure
3.4 that most of the C–N bonds break due to O atom impacts, rather than due to
O_3 molecules.

56
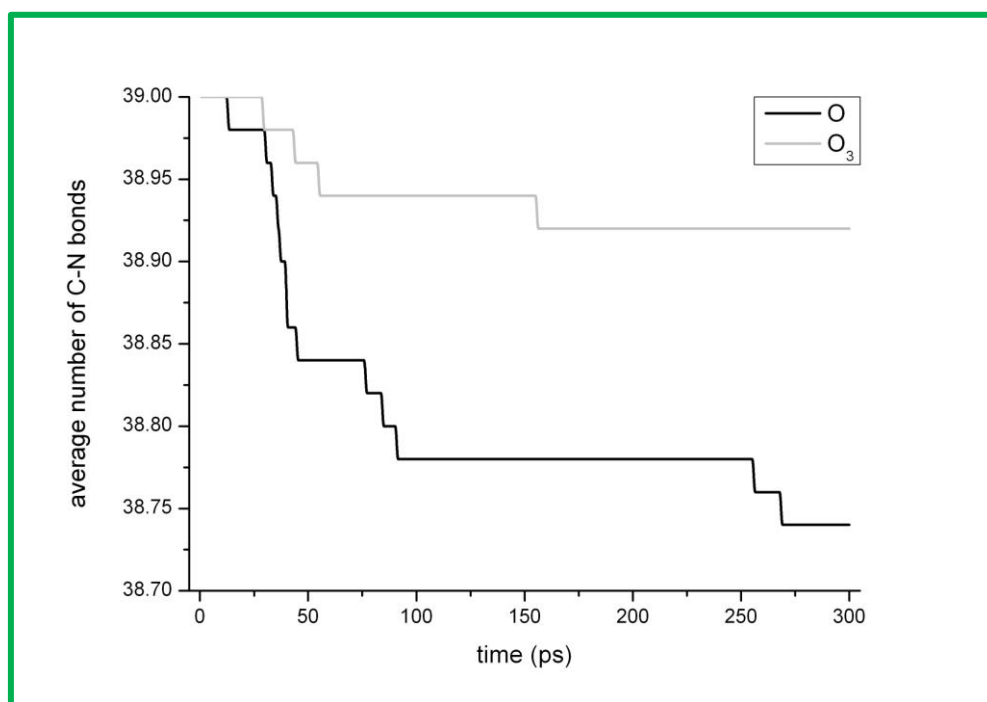
Figure 3.4 *Time evolution of the average number of C–N bonds upon the impingement of O atoms and O₃ molecules. The value of the average number is calculated from 50 independent simulations for each incident species.*

When O atoms are used as the impacting species, dissociation of C–N bonds is observed in 26% of the simulations cases. When O_3 is used, on the other hand, this value decreases to 8% (see Table 3.1).

Table 3.1 *Fraction of dissociation events of important bonds (i.e. C–N, C–O and C–C bonds) and associated standard deviations upon impact of O atoms or O₃ molecules. The values are calculated from 50 independent simulations for each incident species.*

Incident plasma species	C–N bond breaking events (%)	C–O bond breaking events (%)	C–C bond breaking events (%)
O atoms	26 ± 6	78 ± 6	38 ± 7
O₃ molecules	8 ± 4	56 ± 7	26 ± 6

Moreover, it is also observed that most of the C–N bond dissociations occur only in the alanine part of the PG structure. In the case of impacting O atoms, for instance, almost 80% of the C–N bond dissociations occur in the alanine part. Note, however, that the dissociation of C–N bonds occurs only due to the hydrogen abstraction from a methyl group in the alanines (see below).

The calculated bond length distribution of the carbon atoms is shown in Figure 3.5 for different simulation times. At the beginning of the simulation ($t = 0$ ps), there is only one peak centered at ~1.56 Å, indicative of single C–C bonds [212].
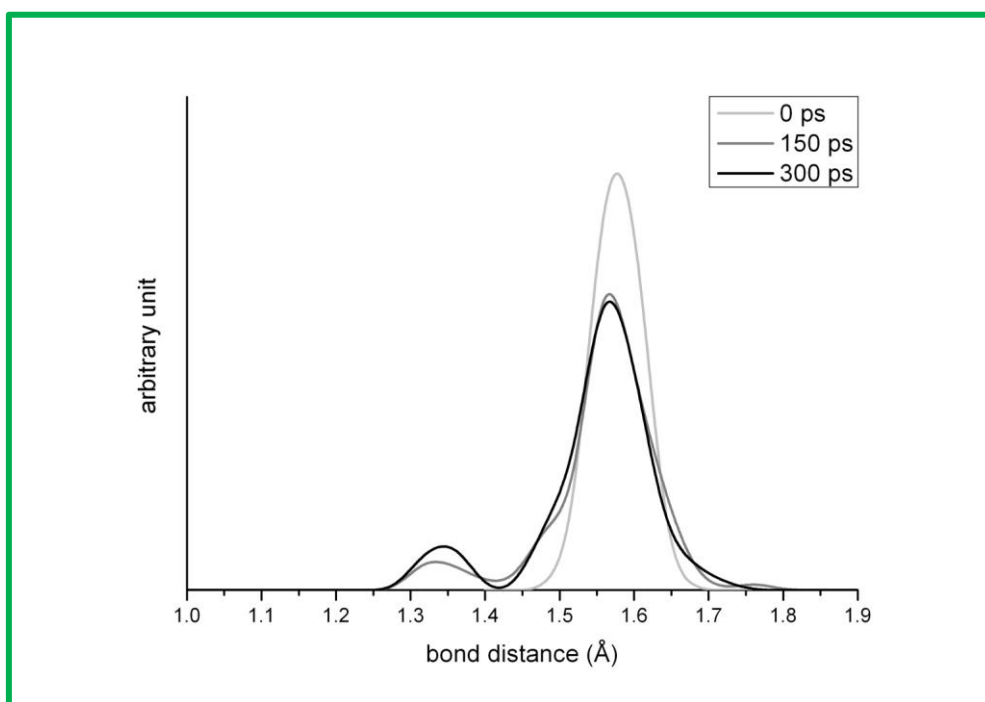
Figure 3.5 *Bond length distribution of carbon atoms after different simulation times, i.e. after 0, 150 and 300 ps. The peaks around 1.56 and 1.34 Å correspond to single and double C–C bonds, respectively.*

After 150 ps, the amplitude of this peak decreases and a new maximum appears at ~1.34 Å, indicating the presence of double C–C bonds. In the subsequent 150 ps, this maximum continues to increase slightly, indicating that the number of double C–C bonds is increasing. Note that the formation of double C–C bonds can only be due to hydrogen abstraction by plasma species. As demonstrated above, this can lead to the breaking of neighboring bonds in some cases (e.g. C–N bonds in the alanine part, see above).

It should also be mentioned that the breaking of C–N bonds in the alanine part depends on the position of the hydrogen abstraction taking place in the alanine. Observations show that if the hydrogen abstraction primarily takes place in the methyl part of the alanine, this eventually leads to the formation of a double C–C bond and the destruction of the neighboring C–N bond (see e.g. Figure 3.2). On the other hand, if the hydrogen abstraction primarily takes place

in the central part of the alanine, it cannot lead to a cleavage of the C–N bond, even if a double C–C bond is formed. For instance, it is obvious from Figure 3.6 that after two hydrogen-abstraction reactions in L-Ala (see Figure 3.1, left side of the PG), a double C–C bond is created without any bond breakage (see Figure 3.6(c)).
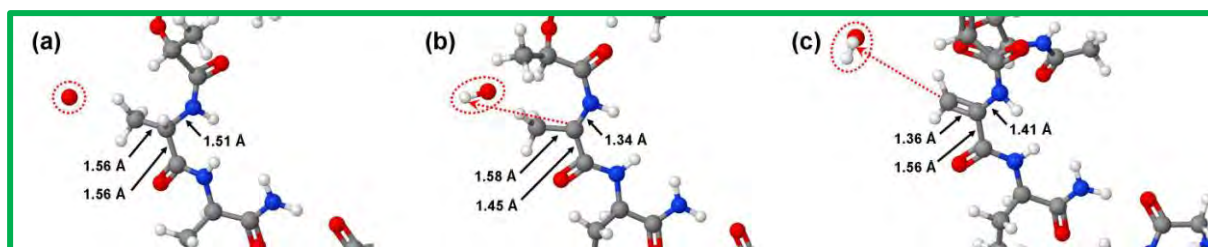
Figure 3.6   *Snapshots from our MD simulations, showing the interaction of an oxygen atom with L-Ala, leading to the formation of a double C–C bond. (a) Oxygen, shown in red dashed circle, reacts with hydrogen positioned at the centre of L-Ala (t = 9.6 ps). (b) Hydrogen abstraction takes place (t = 19.2 ps). (c) Second hydrogen abstraction takes place in methyl residue of L-Ala and double C–C bond is formed (t = 45 ps).*

Indeed, the first hydrogen abstraction occurs in the central part of the alanine (see Figure 3.6(b)) with the formation of a carbon radical. This radical is stabilized by its amide neighbors due to electron delocalization effects [213] and is therefore more stable than the primary radical mentioned above (see Figure 3.2(a)). Hence, after the second hydrogen abstraction, a primary radical is also created and these two radicals subsequently form a stable double C–C bond (see Figure 3.6(c)).

   Note that breaking of C–N bonds is also observed in other parts of the PG. The calculations show that the mechanism of the C–N bond dissociation in these parts is similar to the cleavage mechanism in the alanine part as described above, i.e. it occurs due to hydrogen abstraction and subsequent formation of double C–C bonds. However, no C–N bond-breaking events were observed in the pentaglycine interpeptide, even when hydrogen abstraction took place. This is probably due to the resonance-stabilized structure of pentaglycine. It should also be mentioned that the examples of the C–N bond-breaking mechanisms were demonstrated only for oxygen atoms. As mentioned above, similar mechanisms have been observed for O_3 molecules.

3.4.2 Dissociation of C–O bonds

The structurally important C–O bonds are found both in the disaccharides (MurNAc–GlcNAc) as well as between them. There are four oxygen atoms that are linked with two carbon neighbors in one disaccharide (see Figure 3.1), while the other oxygen atoms in the structure have either hydrogen neighbors or they are connected with carbon atoms by double bonds. Therefore, the breaking of these C–O bonds is not considered in this study, as they do not play a significant role in the destruction of the PG structure (see Figure 3.1).
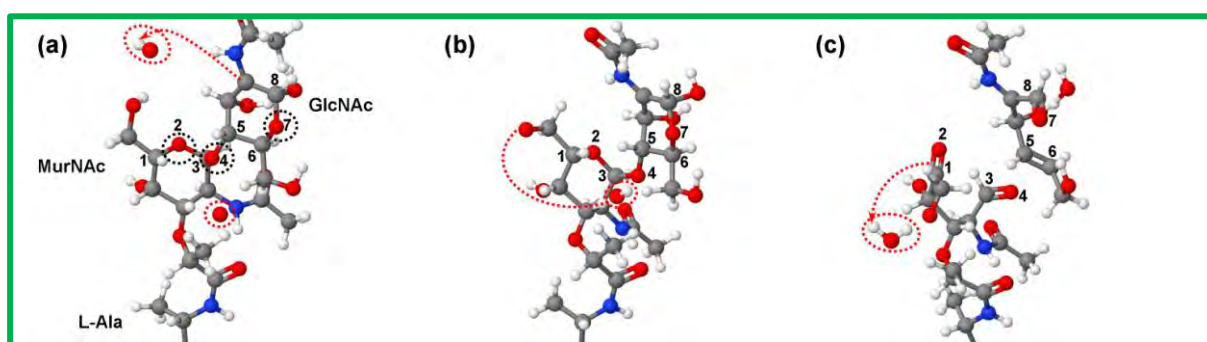
Figure 3.7   Snapshots from our MD simulations, showing the consecutive breaking mechanisms of three important ether C–O bonds (see black dashed circles) upon oxygen atom impact. (a) First oxygen atom abstracts the hydrogen from GlcNAc (see first red dashed circle, t = 16.8 ps). (b) Another hydrogen is abstracted from MurNAc by a second oxygen atom, resulting in the formation of an OH radical (see red dashed circle, t = 45 ps). (c) The OH radical abstracts another hydrogen atom, which is connected to C_1 (cf. C_1 from (b)), and a water molecule is created (t = 45.6 ps). Subsequently, some double C–O and C–C bonds are formed, which lead to breaking of the C–O ether bonds (cf. the bonds between numbered atoms from (b) and (c), and see text for a detailed description of the mechanism).

There are several C–O bond-breaking mechanisms observed in this study. In all of these mechanisms, the dissociation again occurs due to the hydrogen-abstraction reaction. After the hydrogen abstraction, a double C–O bond may be formed (more specifically, one C–O bond is broken and another becomes a double bond), or a double C–C bond may be formed, or both double bonds are formed. In most cases, the hydrogen-abstraction reaction leads to a cascade of C–O bond cleavage events, i.e. the breaking of three important C–O bonds: one in MurNAc, one in GlcNAc and one between them (see Figure 3.1). Note that here ether bonds are denoted as "important C–O bonds", i.e., as one of two bonds between two carbon atoms and one oxygen atom in disaccharides (see Figure 3.7(a), black dashed circles).

One of the observed consecutive breaking mechanisms of three ether bonds is presented in Figure 3.7. Note that this mechanism is observed most in the simulation for all impinging species. In Figure 3.7(a), the oxygen atom abstracts a hydrogen atom from GlcNAc with the formation of an OH radical (see first red dashed circle). After a few ps, a second oxygen atom abstracts a hydrogen atom from MurNAc and a second OH radical is formed (see Figure 3.7(b), red dashed circle). For clarity, some atoms were numbered that participate in the dissociation of the ether bonds (see Figure 3.7(a), black dashed circles). In Figure 3.7(c), the OH radical abstracts another hydrogen, which is connected to C_1, with the formation of a water molecule. Consequently, a radical is created at C_1, which results in a cascade of homolytic cleavage and double bond formation reactions starting with the creation of a double C_1–O_2 bond, which in turn leads to cleavage of the C_3–O_2 bond. The latter subsequently leads to the creation of a double C_3–O_4 bond. Moreover, this leads to the cleavage of the C_5–O_4 bond, which in turn yields the formation of the double C_5–C_6 bond. This subsequently results in the dissociation of the C_6–O_7 bond and the formation of the double C_8–O_7 bond. Finally, the cascade process leads to cleavage of part of the molecule, which in turn eventually results in damage to the bacterial cell wall.

In Figure 3.8, the time evolution of the average number of ether bonds upon impact of O atoms and O_3 molecules is shown. As mentioned above, the average number of ether bonds is calculated from 50 runs for each incident species.

It is clear from Figure 3.8 that the average number of C-O bonds decreases during the simulation, i.e. the C–O bonds are broken by the impacting plasma species. Moreover, most of the ether bond cleavage events occur due to oxygen atoms impacts, rather than due to O_3 molecules (see Figure 3.8). From the 50 simulations that were carried out for each type of incident species, the dissociation of the ether bonds occurs with oxygen atoms in 39 cases (i.e., 78%), whereas this value is 28 for O_3 (56% of the cases), i.e. about 1.4 times less (see Table 3.1). It should also be mentioned that most of the bond cleavage events occur in the disaccharide part, rather than in other parts of the PG structure. Thus, the dissociation of the important ether C–O bonds in the disaccharide part is observed much more frequently than the dissociation of C–N or C–C bonds in other parts of the PG structure. The values for C–N bond-breaking are shown above and those for C–C bond-breaking are given below in *subsection 3.4.3*.
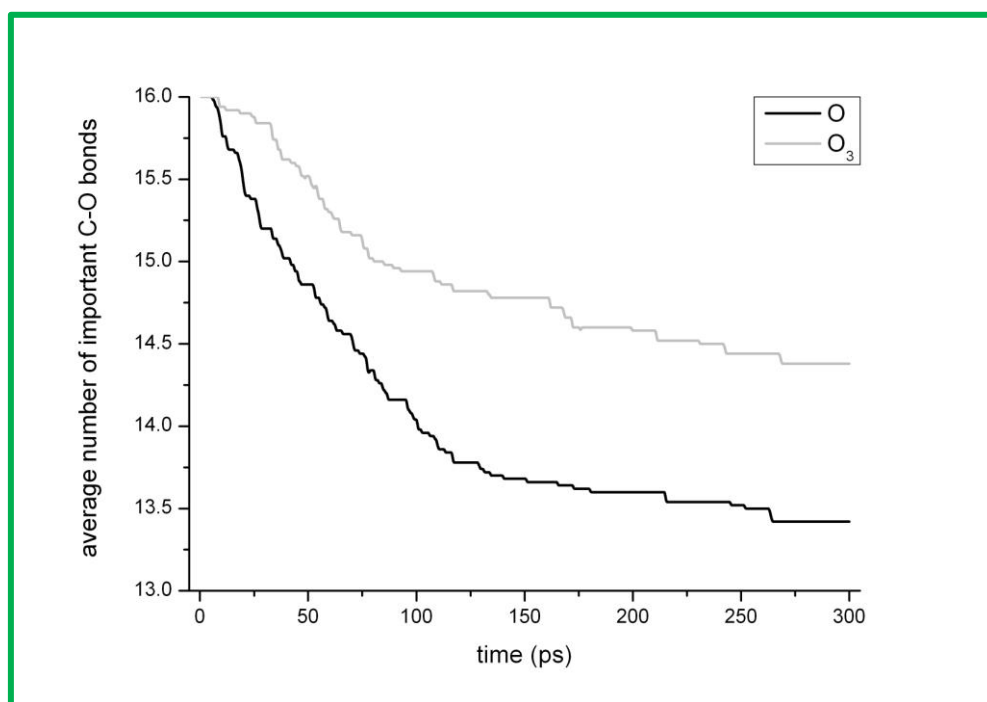
Figure 3.8   *Time evolution of the average number of ether bonds upon the impingement of O atoms and O_3 molecules. The value of the average number is calculated from 50 simulations for each incident species.*

The study on C–O bond dissociation shows that if the hydrogen-abstraction reaction is initiated at a carbon atom located near one of the three important ether bonds in the disaccharide part (see Figure 3.7(a), black dashed circles), this can eventually lead to consecutive cleavage of at least two of these three C–O bonds. Moreover, it should also be mentioned that the carbon, at which the hydrogen-abstraction reaction takes place and subsequently the dissociation of the important C–O bonds occurs, should not necessarily be a first neighbor of the participating O atom in a ring of MurNAc or GlcNAc. Indeed, the dissociation of the ether bonds in MurNAc, GlcNAc or between them can also occur when the hydrogen-abstraction reaction takes place from another carbon atom, which is a second or third neighbor of the participating O atom in a MurNAc or GlcNAc ring. Furthermore, the cleavage of the important C–O bonds (and even cleavage of all three of them) can be observed when the hydrogen abstraction takes place from a carbon or oxygen, which are positioned in the residue close to the O atom in a ring of MurNAc or GlcNAc (see Figure 3.7(b), residues connected to C_1 and C_6).

62

The dissociation of a fourth ether bond occurs mostly due to the hydrogen abstraction from a methyl residue of MurNAc, which is close to this bond (see Figure 3.9(a), black dashed circle).
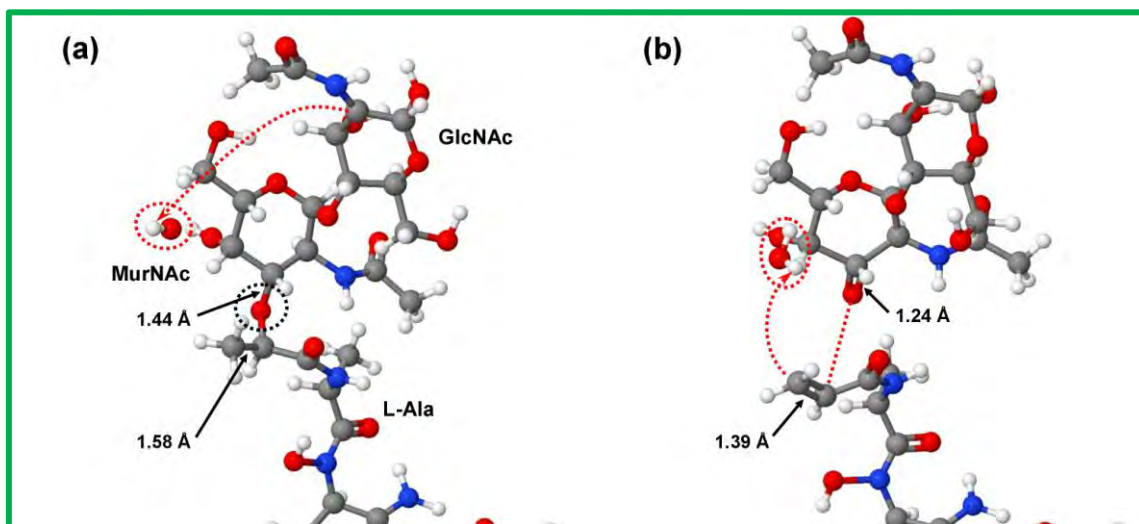
***Figure 3.9*** *Snapshots from our MD simulations, showing the breaking mechanism of the fourth important ether C–O bond (see black dashed circle) upon oxygen atom impact. (a) Oxygen abstracts the hydrogen atom from GlcNAc and an OH radical is formed (t = 70.2 ps). (b) Another hydrogen is abstracted from the methyl residue of MurNAc, which is close to the fourth ether bond, resulting in the formation of double C–C and C–O bonds, which subsequently leads to the cleavage of the fourth ether bond (t = 70.8 ps).*

Indeed, after the hydrogen abstraction from the methyl residue, an unstable primary alkyl radical is created, which leads to the formation of a double C–C bond and this, subsequently, will induce the breaking of the ether bond and the formation of the double C–O bond (see Figure 3.9(b)); the bond lengths are indicated for the sake of clarity.

It should also be mentioned that after breaking of any of the structurally important C–O bonds in the disaccharide part, a double bond remains instead of two single bonds. It is also clear from Figure 3.10 that at the beginning of the simulation, the number of single and double C–O bonds in the PG is approximately the same (see Figure 3.10, light gray curve). However, after 150 ps, i.e. in the middle of the simulation, the number of single bonds has already decreased significantly, whereas the number of double C–O bonds has increased (see Figure 3.10, gray curve).
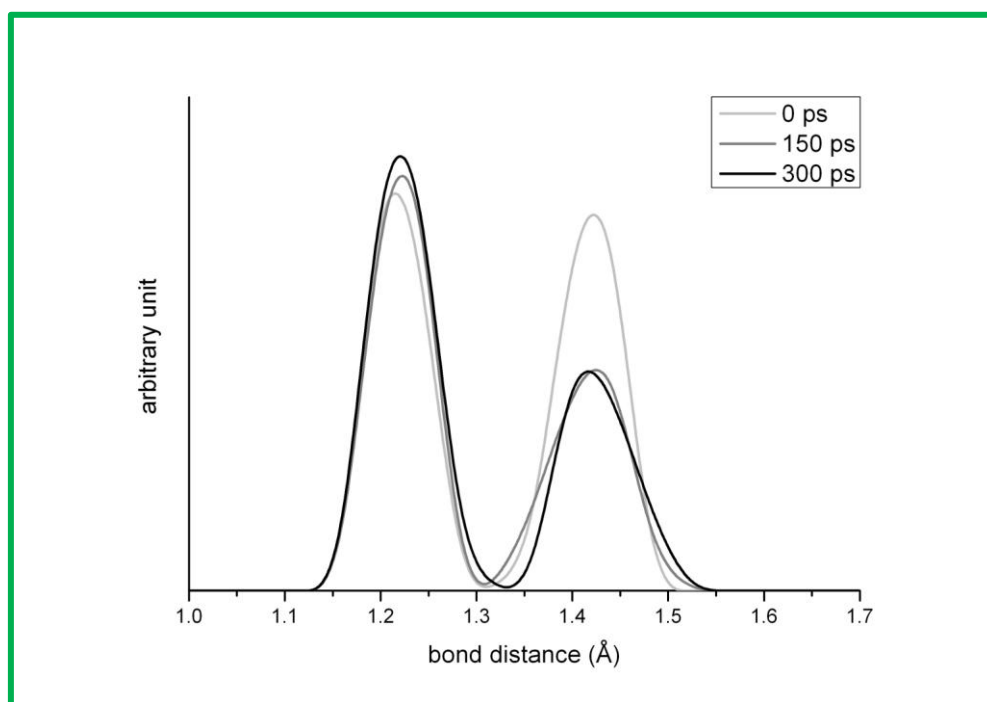
Figure 3.10 *C–O bond length distribution after different simulation times, i.e. after 0, 150 and 300 ps. The peaks around 1.43 and 1.23Å correspond to single and double C–O bonds, respectively.*

Finally, at the end of the simulation, the peak of the double C–O bonds becomes approximately twice as high as the single C–O bond peak. The comparison of the maxima of the single and double C–O bond curves in the beginning and at the end of the trajectory (i.e., at 0 ps and after 300 ps, respectively) shows the decrease in single C–O bonds much faster than the increase in double C–O bonds. This is due to the dissociation of single C–O bonds and the formation of double C–O bonds. Indeed, the latter are formed from remaining (i.e. non-dissociated) single C–O bonds. Note that all examples of the important ether C–O bond-breaking mechanisms were shown above only for oxygen atoms. As mentioned above, similar mechanisms were observed in the case of O_3.

3.4.3 Dissociation of C–C bonds

As is clear from Figure 3.1, bonds between carbon atoms are found in all parts of the PG structure. However, our investigation shows that the dissociation of C–C bonds occurs only in the disaccharide part and in most cases after the breaking of three ether bonds (see above).

As is the case for the C–N and the C–O bonds, a number of different bond-cleavage mechanisms are observed for C–C bond dissociation. The most frequently observed mechanism is illustrated in Figure 3.11.
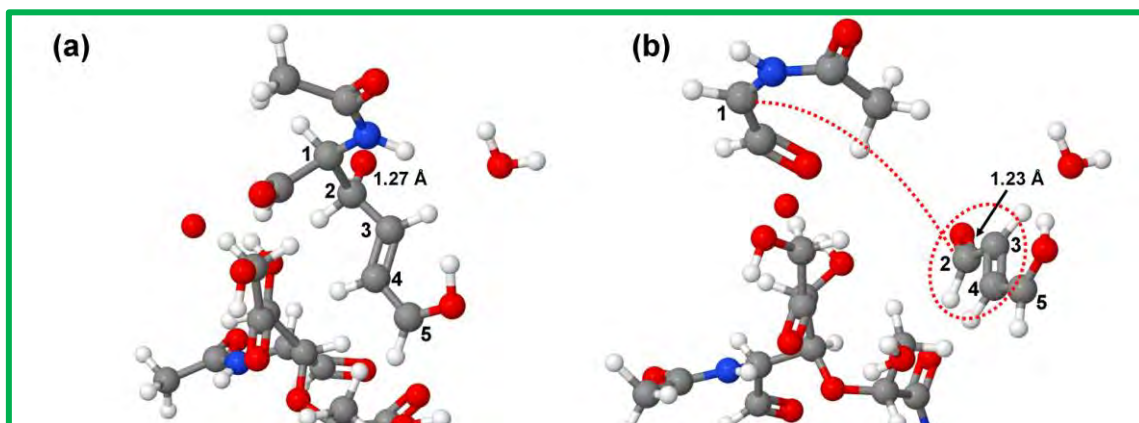
Figure 3.11 *Snapshots from our MD simulations, showing the breaking mechanism of a C–C bond upon oxygen atom impact. (a) After the hydrogen abstraction, the distance between the oxygen radical and C_2 begins to decrease (t = 81.6 ps). (b) Oxygen radical forms a double bond with C_2 and this leads to the dissociation of the C_1–C_2 bond (t = 82.8 ps). As a result, a conjugated system is formed (see red dashed circle).*

In this process, the C–C bond in GlcNAc is broken after the homolytic cleavage of three ether bonds. Again, for clarity, the C atoms participating in the mechanism are numbered (see Figure 3.11). It can be seen in Figure 3.11(a) that after the initial hydrogen-abstraction reaction an O radical is created, which is connected to C_2. For the O radical to form a double C–O bond, one of the two C–C bonds (i.e. bonds between C_1–C_2 or C_2–C_3) needs to be homolytically broken. This bond cleavage is found to occur between C_1–C_2. This results in the formation of two molecules: one with a conjugated system (see Figure 3.11(b), red dashed circle) and one with a resonance-stabilized radical. Note that the radical in the conjugated system is also resonance stabilized (see Figure 3.11, C_5), although this radical is not important for the above-mentioned breaking mechanisms since the same mechanisms were also observed when there was no radical at that position (see Figure 3.11, C_5).

The time evolution of the average number of C–C bonds upon impact of O atoms or O_3 molecules is depicted in Figure 3.12.
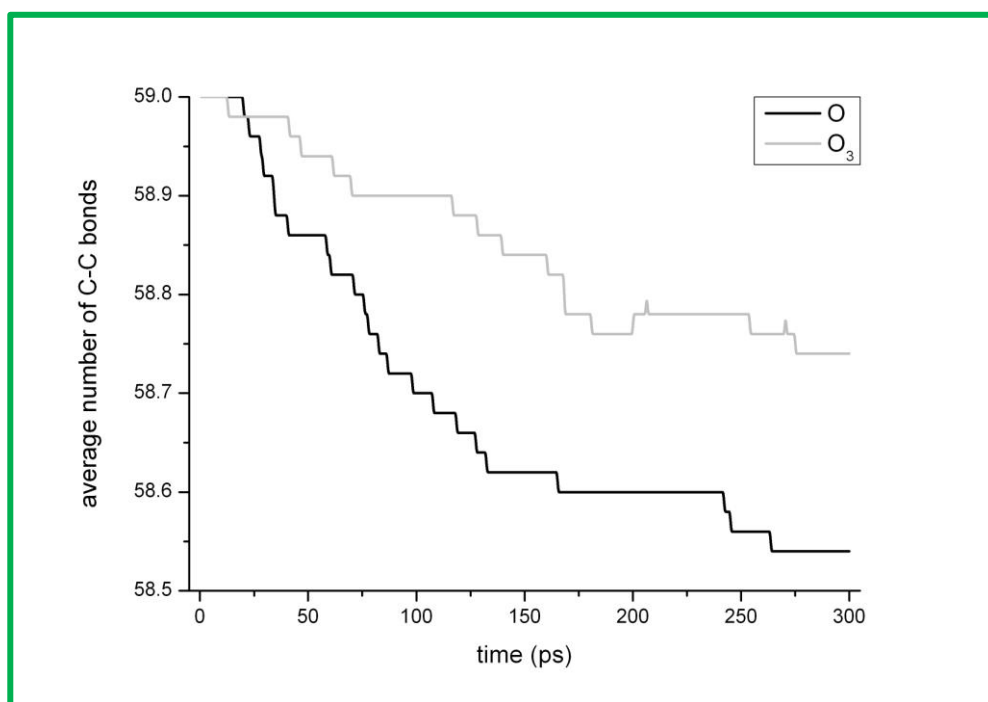
Figure 3.12 *Time evolution of the average number of C–C bonds upon the impingement of O atoms and O₃ molecules. The value of the average number is calculated from 50 simulations for each incident species.*

As was mentioned above, the average number of C–C bonds is calculated from 50 runs for each incident particle. It is clear from Figure 3.12 that the average number of C–C bonds decreases during the simulation, i.e., the C–C bonds are effectively broken by impinging plasma species. Again, most of the C–C bond-breaking events occur due to oxygen atom impacts, rather than due to O_3 molecules. Furthermore, the investigation shows that from the 50 simulations performed for each impinging species, oxygen atoms lead to dissociation in 19 cases (38%), whereas O_3 leads to dissociation in 13 of these cases (26%, see Table 3.1).

It should be mentioned that for O_3 molecules the same C–C bond-breaking mechanisms were observed as for the O atoms.

3.5 Interaction of hydrogen containing oxygen species with peptidoglycan

In a previous section the interaction of oxygen species, i.e., O, O_2 and O_3, with bacterial PG was investigated. These species are formed in the plasma, but it is not certain that they can really interact with bacteria, as they might react in the liquid layer surrounding the cells, forming other species, such as OH, H_2O_2, as well as H_2O molecules [62, 214]. These H-containing species are also generated in the plasma itself, and might remain stable when penetrating the liquid layer surrounding the bacterial cells. It is also known that H_2O_2 is mainly formed from gas phase recombination of OH radicals [215]. Hence, OH radicals can act as highly reactive species on their own, but also as precursors for the formation of H_2O_2 molecules. The chemical reactivity of these ROS warrants the effectiveness of plasmas for decontamination and sterilization purposes [30, 63].

In this section, the mechanisms of the interaction of the H-containing reactive oxygen plasma species (i.e. OH, H_2O_2 and H_2O) with PG are studied. Also O, O_3, and O_2 are considered once again, to elucidate (and also summarize) which of these ROS (i.e., O, O_2, O_3, OH, H_2O_2 and H_2O) are indeed important for bacterial cell inactivation. Water molecules are also considered as impinging species, as water vapor is naturally present in atmospheric air, and most bio-organisms, including bacteria, are commonly coated by an aqueous layer surrounding them. Consequently, studying the interaction mechanisms of water molecules with the surface of bacterium (e.g. with the PG) is also of significant interest.

3.5.1 Results and discussions

The investigations on the impacts of H_2O (as well as O_2, see *section 3.4*) reveal that no bond-breaking events occur in the important C–O, C–C and C–N bonds in PG. These molecules are found to assemble around the PG, having weak attractive non-bonded interactions with the structure (i.e. hydrogen bridge formation). Therefore, H_2O (as well as O_2) molecules will not be considered in this section.

The impacts of OH and H_2O_2 species (as well as O and O_3, see *section 3.4*), on the other hand, do result in important bond breakings, but the mechanisms

induced by these species appear to be completely different. Indeed, the break-up mechanism induced by OH (as well as by O and O_3) impacts consists of the dissociation of structurally important bonds (i.e., C–O, C–C and C–N bonds) in the PG, initiated by a hydrogen-abstraction step by the impinging species. In most cases, the abstraction of hydrogen leads to a cascade of C–O bond cleavage events, that is, the dissociation of three important ether bonds in the disaccharide: one in MurNAc, one in GlcNAc and one between them. A visual representation of this mechanism for OH impacts is shown in Figure 3.13. Similar results were presented in *subsection 3.4* for the O and O_3 species.
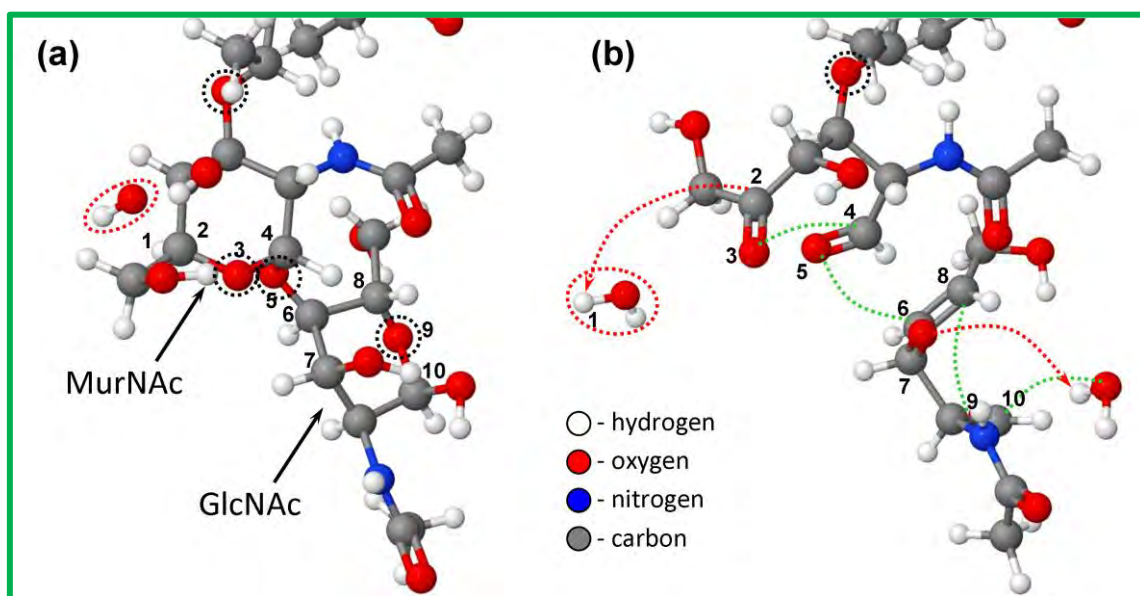
Figure 3.13 *Snapshots from our MD simulations, presenting the consecutive breaking of three important ether C−O bonds in the disaccharide (see black dashed circles in MurNAc, GlcNAc, and between them) upon OH radical impact. (a) OH radical (see red dashed circle) first approaches H_1. (b) OH radical abstracts the H_1 atom, which is connected to C_2, forming a water molecule (see red dashed circle). Subsequently, some double bonds are created, which lead to the dissociation of three ether C−O bonds (cf. the bonds between numbered atoms from (a) and (b)). The hydrogen-abstraction reaction and the breaking of bonds are indicated by red dashed arrows and by green dashed lines, respectively.*

The interaction mechanisms of H_2O_2 molecules with PG differ from the mechanisms of the other investigated plasma species (i.e., OH, O_3, and O). The main difference is that H_2O_2 molecules first dissociatively react with each other, forming HO_2 radicals and water molecules. Subsequently, these HO_2 radicals react with the PG structure. Hence, in all cases, the interaction mechanism is initiated by hydrogen-abstraction, but in the case of H_2O_2, the hydrogen is

abstracted from the HO_2 radicals by the PG (mostly by an O atom of the PG structure, see below), whereas in the case of the other plasma species investigated (i.e., OH, O_3, and O), the impinging species abstract a hydrogen from the PG.

As in the case of the other impacts, most of the bond-breaking processes due to H_2O_2 molecules occur in the disaccharide parts of the PG (i.e., dissociation of the important ether C−O bonds; see Table 3.2 below). Various C−O bond-breaking mechanisms are observed in the case of H_2O_2 impacts. The most frequently observed mechanism is illustrated in Figure 3.14. For clarity, relevant atoms are numbered, and the O and H atoms of the impinging H_2O_2 molecules are colored purple and light blue, respectively.
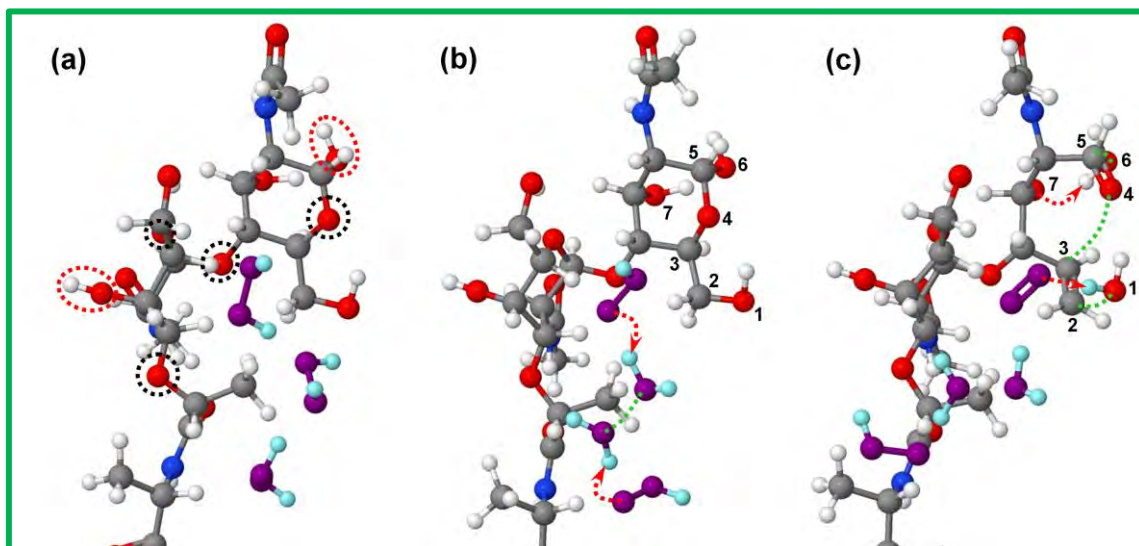
Figure 3.14 Snapshots from our MD simulations, showing the breaking mechanism of the important ether $C_3−O_4$ bond in GlcNAc upon impact of H_2O_2 molecules. Atoms positioned in the periodically repeating parts of the PG are shown in panel (a) by red dashed circles, and the ether bonds are indicated by black dashed circles, respectively. H_2O_2 molecules, with the corresponding O and H atoms, are indicated in purple and light-blue colors, respectively. The hydrogen-abstraction reaction and the breaking of bonds are indicated in panels (b) and (c) by red dashed arrows and by green dashed lines, respectively. The color legend is identical to Figure 3.13.

In a first step, H_2O_2 molecules assemble around the PG as a result of weak attractive non-bonded interactions with the PG structure (see Figure 3.14(a)). When three H_2O_2 molecules are in close vicinity of each other, they react with each other, dissociating into HO_2 radicals and water molecules in a concerted process (see Figure 3.14(b): red dashed arrows and green dashed line).

Subsequently, one of the HO_2 radicals reacts with the OH residue of GlcNAc (see Figure 3.14(c)). This OH residue abstracts the hydrogen from the HO_2 radical, forming water (see O_1 with bonded H atoms) and an oxygen molecule. As a consequence, this leads to the simultaneous dissociation of C_2-O_1, C_3-O_4, and C_5-O_6 bonds, the formation of double C_2-C_3 and C_5-O_4 bonds, and the abstraction of a hydrogen connected to O_7 by O_6 (see Figure 3.14(c)). Our simulations predict that the dissociation of other ether bonds is also initiated by hydrogen-abstraction from HO_2 radicals.

Table 3.2 *Fraction of important bond dissociations (i.e., C–N, C–O and C–C bonds) and associated standard deviations upon impact of O, O_3, OH and H_2O_2. Note that the values are calculated from 50 independent simulations for each incident species.*

Incident plasma species	C–N bond breaking events (%)	Ether C–O bond breaking events (%)	C–C bond breaking events (%)
O atoms	26 ± 6	78 ± 6	38 ± 7
O_3 molecules	8 ± 4	56 ± 7	26 ± 6
OH radicals	8 ± 4	54 ± 7	14 ± 5
H_2O_2 molecules	0	44 ± 7	12 ± 5

The investigations on H_2O_2 molecules interacting with PG reveal that fewer consecutive dissociations of three important ether bonds take place in comparison with O_3, OH, and O impacts (see Figure 3.13(b) for the OH impacts). This can be attributed to the different bond-breaking mechanisms occurring in the case of H_2O_2 (see above). As a result, H_2O_2 molecules are slightly less effective in breaking C−O bonds than the other plasma species, as can be deduced from Table 3.2.

Similarly, they are also less effective in breaking C−N and C−C bonds, as is also evident from Table 3.2. Indeed, dissociation of C−N bonds upon impact by H_2O_2 molecules is not observed at all in the simulations. The O, O_3, and OH species can break C−N bonds, and this is again invariably initiated by hydrogen-abstraction reactions. The cleavage of C−N bonds is found to occur most often in the alanine parts rather than in other parts of the PG structure.

The bond-breaking mechanisms of C−C bonds are found to be similar for the different plasma species investigated; that is, the dissociation of C−C bonds

occurs only in the disaccharides, as part of a consecutive mechanism initiated by the breaking of ether bonds. Indeed, after the homolytic dissociation of C−O bonds, some oxygen atoms form a double bond with a neighboring C atom, and this can lead to the breaking of C−C bonds. Thus, the OH, O_3, O, and H_2O_2 species are only capable of breaking C−C bonds indirectly.

Finally, it is clear from Table 3.2 that dissociation of the important ether C−O bonds in the disaccharides is observed much more frequently than the dissociation of C−N or C−C bonds in the PG.

To further quantify the bond cleavage processes, we calculated the average times needed to break the important bonds (i.e., C−O, C−C, and C−N bonds) in the PG, and they are shown in Table 3.3 for the case of O atom impact. Here the results are only shown for the average times needed for breaking of maximum two bonds.

Table 3.3   *Average characteristic times needed to break the important bonds (i.e. C–O, C–C and C–N bonds) and associated standard deviations, upon impact of O atoms. Note that the values are calculated from 50 independent simulations and each simulation time takes 300 ps.*

Bonds	bond broken	Number of events	Average time (ps)
C–O	first	39	53 ± 9
	second	34	63 ± 9
C–C	first	19	98 ± 18
	second	3	89 ± 20
C–N	first	12	85 ± 25
	second	1	37 ± 0

Note that in this study, up to seven C−O bond-breaking events are observed in one run (see consecutive breaking mechanism of C−O bonds, illustrated in Figure 3.13 above), but it is not shown in the table, as we here focus on the initiation of the dissociation of important bonds in the PG. However, more detailed tables for the average times of all bond-breaking events, for all impacting species, can be found in the supporting information of [216].

It is clear from Table 3.3 that the bond-breaking events do not occur immediately after the start of the simulation. Indeed, in most cases, it takes several tens to 100 ps before a bond is broken. Once a C−O bond is broken, it

typically takes only a short time before the next C−O bond is broken. Indeed, in the case of O atom impacts, in 71% of the cases the second C−O bond is broken within 2 ps, and in 50% of the cases, the second bond-breaking occurs even almost immediately (i.e., within 0.6 ps), and this corresponds to the consecutive breaking of ether C−O bonds (see above). In the case of the other plasma species (i.e., OH, O_3 and H_2O_2), the percentages of the short time differences (i.e., within 2 ps after the first bond-breaking) are 43%, 58%, and 42%, respectively, whereas the percentages of immediately occurring bond-breaking (i.e., consecutive breaking of ether C−O bonds) amount to 29%, 42%, and 42% for OH, O_3, and H_2O_2 impacts, respectively. These results again show that most of the ether C−O bond cleavage processes correspond to the consecutive breaking of three ether bonds.

The presented results for the average times needed for breaking of important bonds again show that the chosen simulation time (i.e., 300 ps) is long enough to observe the bond-dissociation processes in the PG structure.

3.6 Conclusions

The interaction of important plasma species, that is, O, OH, O_2, O_3, H_2O, and H_2O_2 molecules, with bacterial PG was investigated by means of reactive MD simulations. It was found that O_2 and H_2O molecules cannot structurally damage the PG structure and interact with PG through hydrogen bridge formation. The other plasma species, i.e., O, O_3, OH, and H_2O_2, are found to break structurally important bonds of PG (i.e., C−O, C−C, or C−N bonds), which subsequently leads to destruction of the bacterial cell wall. The performed calculations reveal that O_3, OH, and especially O atoms are more effective in bond cleavage than H_2O_2 molecules, in agreement with many experiments demonstrating the crucial role of reactive oxygen species (such as O and OH) in bacterial inactivation [62-64, 103-106, 217].

Furthermore, the ether C−O bonds in the disaccharides are found to break up more easily, followed by the C−C bonds and C−N bonds in PG. In the case of H_2O_2 molecules, no C−N bond-breaking events are observed, indicating again that the H_2O_2 molecules are somewhat less effective in bacterial cell wall

destruction. However, in contrast with the highly reactive O and OH radicals, H_2O_2 molecules are stable species in an aqueous environment and are thus more likely to interact directly with the PG. Hence, it is expected that the H_2O_2 molecules are also very important for bacterial deactivation.

The mechanisms of the important bond-breaking processes in PG were studied in detail. It was found that in all bond cleavage events the dissociation of important bonds (i.e., C–O, C–C and C–N bonds) is initiated by hydrogen-abstraction. However, a clear difference is observed in the mechanisms upon impact of H_2O_2 molecules on one hand and OH, O, and O_3 species on the other hand. Indeed, in the latter case a H atom is abstracted from the PG by the plasma species (OH, O, or O_3), whereas in the case of H_2O_2 impacts, the H_2O_2 molecules first react with each other, forming HO_2 radicals, from which a H atom is abstracted by an O atom in the PG structure. Abstraction of a H atom from the HO_2 radicals can then cause the dissociation of the important bonds in PG (i.e., cell wall damage). This corresponds to the experimental observation that hydroperoxyl (HO_2) radicals are strong bactericidal oxidants and can cause the inactivation of the bacteria in an aqueous environment [128, 218].

The fraction of important bond dissociations upon impact of O, O_3, OH and H_2O_2 was also shown. The obtained values were calculated from 50 independent simulations for each incident species.

C–N bond dissociations are found to occur most often in the alanines, rather than in other parts of the PG structure. These dissociations are again invariably initiated by a H-abstraction reaction, removing a H atom from the methyl part of the alanines. The H-abstraction reaction which leads to the dissociation of the ether bonds in the disaccharides, most often also leads to a cascade of additional ether bond-breaking events. This results in the dissociation of three important C–O bonds, i.e., the ether bonds in MurNAc and GlcNAc, and the ether bond between them. Moreover, the dissociation of a fourth important C–O bond occurs mostly due to the H abstraction from the methyl residue of MurNAc, which is close to this bond. It was also found that the cleavage of the C–C bonds occurs only in the disaccharides and in most cases after the breaking of three ether bonds.

The average times needed for breaking important bonds are typically in the order of several tens to 100 ps. This shows that the chosen simulation time (i.e., 300 ps) is long enough to observe the bond dissociation processes in the PG.

Moreover, once a first C−O bond is broken, it typically takes <2 ps before a second C−O bond is broken (i.e., in at least ~50% of the cases), which illustrates that the ether C−O bond cleavage process typically proceeds through the consecutive breaking of three ether bonds.

It should, however, be realized that these MD simulations correspond to "ideal" conditions. In reality, bacteria are typically surrounded by a liquid film, which affects the effectivity of the plasma species in dissociating chemical bonds. The effect of this liquid film has not yet been included in this study, but will be investigated in *chapter 4* below. Indeed, the moist environment could prevent the PG destruction in reality, since reactive oxygen species might be less exposed to the PG in the bacterial cell wall. On the other hand, it is known that under some conditions, the plasma jet can blow away (part of) the liquid film [219]. Thus, our simulations provide detailed insight in the mechanisms of bacterial cell wall damage by plasma species when the liquid film is not present or blown away, or when it is of little importance.

Chapter 4

Behavior of reactive oxygen species in a water layer

(Investigation of plasma-liquid film interaction)

4.1 Introduction

In *chapter 3*, the reactive MD simulations were performed to study the interaction mechanisms of ROS with PG, which is an important component of the cell wall of gram-positive bacteria. Note, however, that these simulations were carried out under perfect vacuum conditions (i.e. the PG was without a liquid film surrounding it). In reality, bacteria are typically covered by a liquid layer, which in turn can affect the plasma species; the plasma species can either reach the biomolecules by travelling through this film or they can form new species along the way. Hence, it is important to investigate the behavior of these reactive plasma species in a liquid film.

Therefore, in this chapter, the interaction mechanisms of various ROS with a liquid layer are investigated. Specifically O, OH and HO_2 radicals, as well as H_2O_2 molecules were studied. Water is considered as a model system for the plasma-liquid film interactions, since the largest component of the biofilm (or liquid film) surrounding most bio-organisms, including bacteria, is water [126]. Moreover, many experimental studies on the inactivation of bacteria using CAPP sources are performed in aqueous solutions or water [30, 62, 127-129]. Thus, this atomic level investigation is an important contribution towards a better understanding of the basic phenomena and processes occurring on and in a liquid film when being exposed to the bombardment of plasma species.

As mentioned above, the impinging plasma species under study are O, OH, HO_2 and H_2O_2, which were experimentally identified as being biomedically important [62, 103, 104, 106, 127, 128, 217, 218]. Recently, numerical simulations also demonstrated that chemically reactive species (e.g., O and OH radicals), as well as "long living" species (e.g., O_3 and H_2O_2 molecules) are formed in large quantities after the nozzle exit in an argon plasma jet flowing into humid air [220]. Thus, the probability of these species interacting with the surface of living organisms is high. Note that O_3 and RNS are also found to have bactericidal effects (see e.g., [31, 221, 222]). However, they are not included in the present study, as the force field used in these simulations does not accurately describe reactions between these species and water molecules. Nevertheless, a force field appropriate for studying these species and their reactions is under development.

4.2 Computational details

The water system under study was prepared as follows. First, a box with dimensions 25 Å × 25 Å × 23.93 Å was filled with 500 water molecules, corresponding to a density of 1 g/cm^3. Water molecules were added one by one to the system with random positions (to avoid overlap). The system was then equilibrated for 500 ps in the canonical ensemble, following *NVT* dynamics, at room temperature, employing the Bussi thermostat [145] with a coupling constant of 100 fs. Note that this thermostat differs from the Berendsen thermostat [144] in the way of calculating the scaling factor and it is able to correctly generate the canonical ensemble (see *chapter 2, section 2.3*). Therefore, there is no need to relax the resulting structure in the microcanonical *NVE* ensemble using the Berendsen heat bath, as was done in *chapter 3* above.

The obtained structure is subsequently placed in a new simulation box with dimensions 25 Å × 25 Å × 80 Å and the structure is allowed to expand in the two *z*-directions for 100 ps, again employing the Bussi thermostat. This is done in order to create a liquid-gas interface to investigate the interaction of plasma species with water, when they impact the surface from the gas phase (or plasma). In all simulations (i.e., during the thermalization, as well as during the particle impact simulations) a time step of 0.25 fs is used. PBC (see *chapter 2, section 2.3*) are applied in the *x*- and *y*-directions to mimic an infinite slab of water.

Figure 4.1 illustrates the model system under study (i.e., water, see (a)) and its mass density profile (see (b)). To keep the structure from drifting in the *z*-direction, a center-of-mass restraint is employed, i.e., the distance between the center of mass of water (z = 36.2 Å) and a dummy atom (at z = 5 Å) is kept constant. The water density profile shows that there are two interfaces, i.e., above and below the water slab, where the density increases (or decreases) along the z-axis. Moreover, the density becomes more or less constant (around 0.9 g/cm^3) between z = 26 and 46 Å, corresponding to bulk water. This profile is very similar to the density profile obtained by ab initio MD simulations reported in [223].
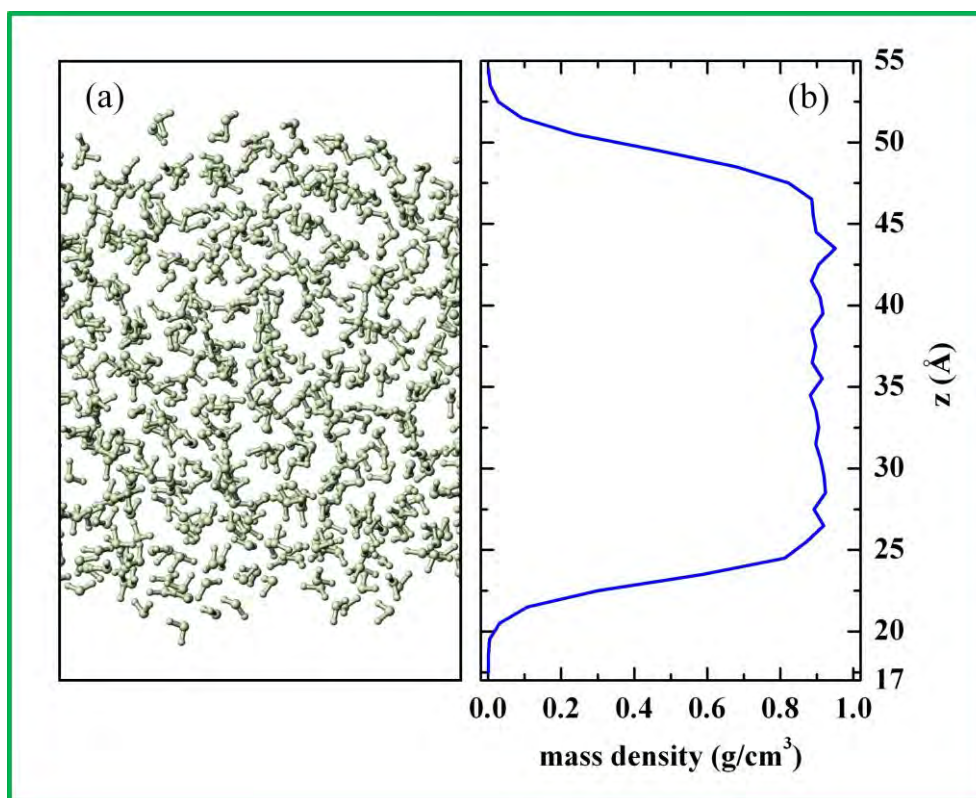
Figure 4.1 *Water slab (shown in grayish green color) with two interfaces above and below (a), and its mass density profile (b). A dummy atom (not shown here) is positioned at z=5 Å, and the distance between this atom and the center of mass of water (z=36.2 Å) is restrained, to keep the structure from drifting in the z-direction.*

4.3 Results and discussions

4.3.1 Validation of the model system

In order to validate the model of water used in these simulations, the structural, static and dynamic properties of water were investigated. All calculated parameters, such as the O–H bond length, partial charges on O and H atoms, HÔH angle, dipole moment, O–O distance and O–O radial distribution functions, are in good agreement with results obtained by *ab initio* simulations [224], classical simulations [184, 225] and experiments [226-228].

The diffusion coefficient of H and O atoms in water is calculated from the long-time behavior of the mean squared displacement (MSD), using the Einstein-Smoluchowski equation (see [184]). The MSD of the H and O atoms

from water molecules is shown in Figure 4.2(a). Note that the MSD was averaged from five different water molecules for both O and H atoms. The calculated diffusion coefficients of both H and O atoms are $\sim 0.12 \text{Å}^2/\text{ps}$ and these values correspond fairly well to the *ab initio* simulation values [224].
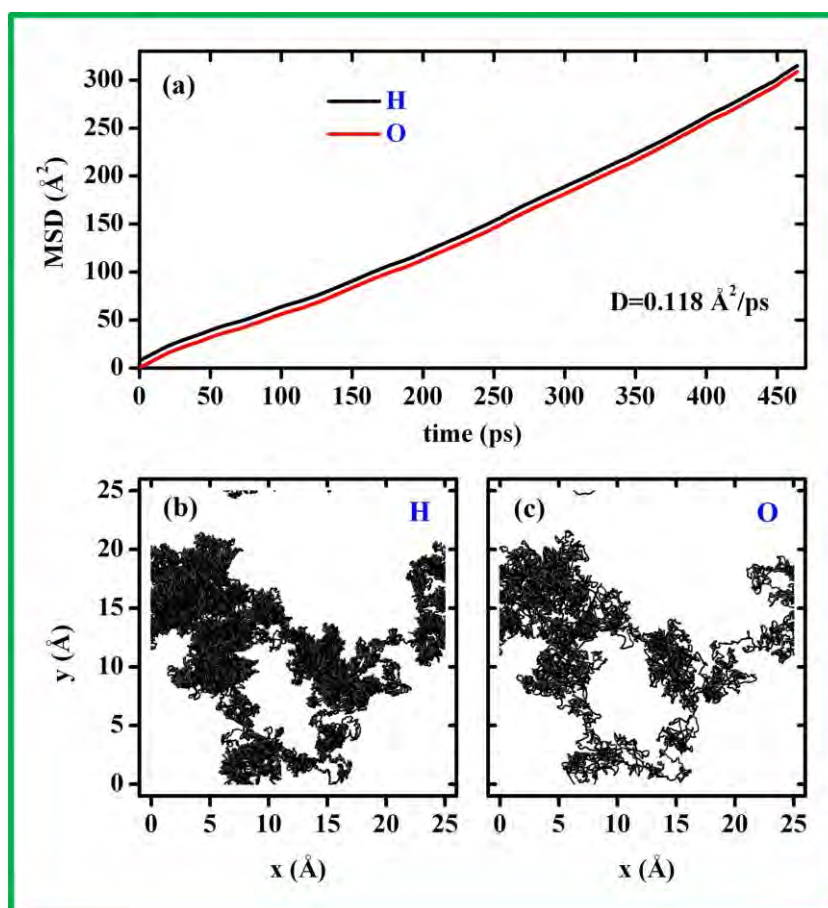
Figure 4.2   *The MSD of hydrogen and oxygen atoms from different water molecules (a), and the trajectories of hydrogen (b) and oxygen (c) atoms of a water molecule in the x-y plane. The calculated diffusion coefficient is $\sim 0.12 \text{ Å}^2/\text{ps}$.*

Panels (b) and (c) of Figure 4.2 illustrate the trajectories of H and O atoms of the same water molecule in the *x–y* plane of the simulation box (i.e., top view, see Figure 4.1). It is clear that the shapes of the trajectories are similar, which explains that the H and O atoms of a single water molecule travel as one system (i.e., the water molecule does not dissociate during the long period of the simulation). The denser profile for H compared to O is the result of the higher oscillation of the former.

4.3.2 Behavior of the plasma species in a liquid layer

a) Interaction of plasma species with water.

To investigate the reaction mechanisms of incident plasma species with water, the MD simulations are performed as follows. Each plasma particle is randomly positioned at a minimum distance of 10 Å above the water slab as before to avoid interaction between the plasma species and water prior to the impact. The initial energy of the impinging plasma species corresponds to room temperature and their velocity directions are chosen randomly; the thermal velocity of the plasma species ranges between 2.5 and 5.5×10^3 m/s at 300 K. The interaction mechanisms of the plasma species with water will be discussed below in the following order: O, OH, HO_2 and H_2O_2.
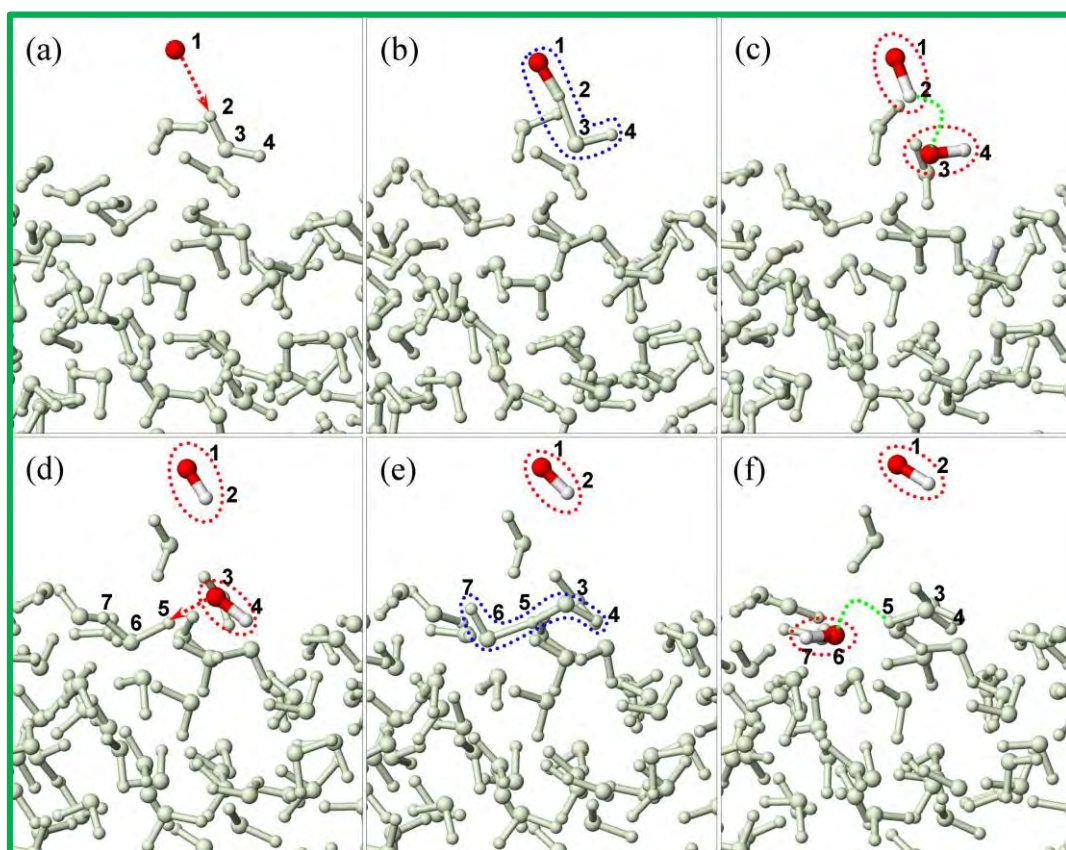
Figure 4.3 *Snapshots from our MD simulations, showing the interaction of an O atom with water, resulting in the formation of two OH radicals (a-c), which subsequently react with water (d-f). The water molecules are illustrated in grayish green color. The reaction intermediates are shown within blue dashed closed-curves. The newly formed OH radicals are presented in red dashed circles. The cleavage of bonds is indicated by green dashed lines.*

The interaction mechanism of O atoms as well as OH radicals with water is presented in Figure 4.3. For clarity, the atoms that participate in the dissociation of O–H bonds are numbered. After approaching one of the water molecules (Figure 4.3(a)), the O atom abstracts a hydrogen atom and two OH radicals are created (see Figure 4.3(c)).

Subsequently, one of the OH radicals (O_3–H_4 in Figure 4.3(c)) reacts with another water molecule resulting in the formation of a new water molecule and an OH radical (H_5–O_3–H_4 and O_6–H_7 in Figure 3(f)). Note that prior to the formation of this new OH radical and water molecule, the reactants go through an intermediate complex (see blue dashed curve in Figure 4.3(e)). Thus, the OH radical and water react with each other, exchanging a hydrogen atom and reforming the reactants. This can be represented in a reaction scheme as follows:

$$OH + H_2O \overset{aq}{\leftrightarrow} [HO - H - OH] \overset{aq}{\leftrightarrow} H_2O + OH \qquad (4.1)$$
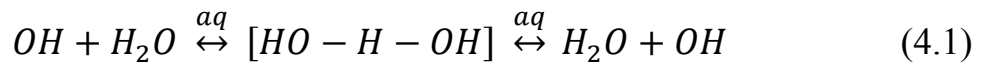
This reaction was observed during the entire simulation period, i.e., 1.4 ns. Hence, the interaction of O atoms with water always results in the formation of OH radicals, whereas the interaction of OH radicals with water leads to the consecutive formation of new OH radicals and water.

Figure 4.4 illustrates the interaction of the HO_2 radical with water. It is clear that the reactants again first go through an intermediate complex (see blue dashed curve in Figure 4.4(b)), resulting in the dissociation of the hydroperoxyl and the formation of a superoxide (O_2^-) and a hydrated proton (H_3O^+) (see red dashed circles in Figure 4.4(c)).

The reaction scheme for HO_2 is given in equation (4.2):

$$HO_2 + H_2O \overset{aq}{\leftrightarrow} [O_2 \cdots H \cdots OH_2] \overset{aq}{\leftrightarrow} O_2^- + H_3O^+ \qquad (4.2)$$
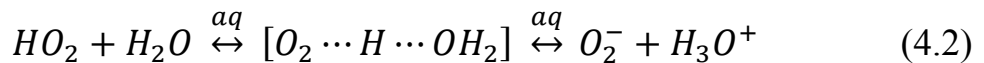
It is obvious from equation (4.2) that every reaction step is in equilibrium, which is in agreement with literature, since it is known that HO_2 dissociates into H^+ and O_2^- in aqueous phase with an equilibrium constant of 2.1×10^{-5} [229]. Moreover, it is stated that HO_2 is a better proton donor but a weaker proton acceptor than water [230]. Our calculations predict that in most cases the ions almost immediately (i.e., within a few fs) recombine to recreate the

hydroperoxyl and water molecules, which is indeed like expected, based on the equilibrium constant [229].
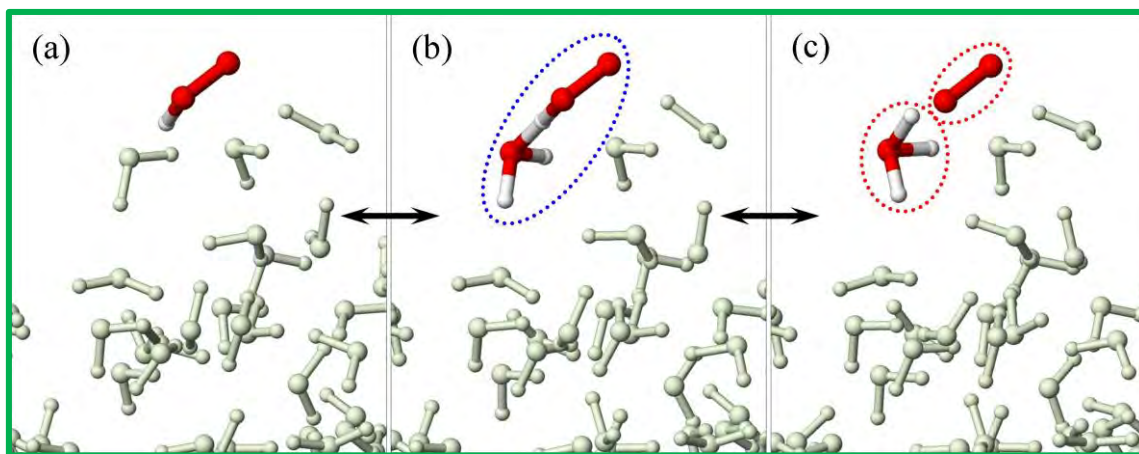
Figure 4.4 *Snapshots from our MD simulations, showing the interaction of a HO₂ radical with water. The water molecules are illustrated in grayish green color. The reaction intermediates and the newly formed species are presented in blue and red dashed circles, respectively.*

However, an analogue mechanism was also observed, in which recombination also takes place, but only after the hydrated proton (H_3O^+) is transported through exchanging the H^+ between several water molecules. This can be explained by "structural diffusion", i.e., the continuous interconversion between hydration complexes, as shown in [231].

In the case of H_2O_2, no bond-breaking events occurred in water, pointing out the stability of H_2O_2 in water. Moin *et al.* have investigated the stability of H_2O_2 in water, using *ab initio* quantum mechanical charge field MD simulations [232]. Their study revealed that there are at least four hydrogen bonds found between H_2O_2 and water molecules, which leads to a strong binding of H_2O_2 with water molecules, and which is responsible for the stabilization of H_2O_2 in aqueous solution [232].

b) Interaction of plasma species with each other in water.

The interaction of plasma species with each other (e.g., OH with OH) in water was also studied. To investigate this, particles of the same plasma species were randomly positioned above the surface of water. To prevent premature reaction of these species with each other in the gas phase, they were shifted closer to the surface, i.e. to $z \approx 55$ Å (cf. Figure 4.1), and positioned relatively

far from each other (i.e., at least 7 Å). Keeping these restrictions in mind, the maximum number of particles that could be simulated was seven (e.g., seven OH radicals). The total simulation time for this study was 100 ps and for each type of plasma species 5 runs were carried out. This time is long enough for reactions to occur. The discussion of the results will again be in the following order: OH, HO_2 and H_2O_2. O atoms will not be considered, since they quickly form OH radicals when they react with water molecules (see Figure 4.3(a–c) above).

The calculations for the OH radicals have revealed that these species do not react with each other in water.

HO_2 radicals, on the other hand, do react with each other according to the following reaction scheme:

$$2HO_2 \xrightarrow{aq} H_2O_2 + O_2 \tag{4.3}$$

The same aqueous phase reaction scheme was shown in [229] with a rate constant of $k_{298} = 8.6 \times 10^5$ M^{-1}s^{-1}.

In the case of H_2O_2 molecules, similar reaction mechanisms as with HO_2 radicals were observed. When three H_2O_2 molecules are in close vicinity of each other on the water surface, one of the H_2O_2 molecules abstracts two H atoms from two other H_2O_2 molecules, resulting in the formation of two water molecules and two HO_2 radicals, as represented in equation (4.4):

$$3H_2O_2 \xrightarrow{aq} 2HO_2 + 2H_2O \tag{4.4}$$

The same mechanism was observed in *chapter 3, section 3.5*, when H_2O_2 molecules interacted with the PG structure. Subsequently, these two HO_2 radicals form H_2O_2 and O_2 through the reaction path given in eqn (4.3) and explained above. Thus, the final products of three H_2O_2 molecules will be H_2O_2, O_2 and water. It was also found that in the interface (and even in the bulk water) two H_2O_2 molecules can react with each other, when a water molecule participates in the reaction:

$$2H_2O_2 + H_2O \xrightarrow{aq} HO_2 + 2H_2O + OH \xrightarrow{aq} O_2 + 3H_2O \qquad (4.5)$$
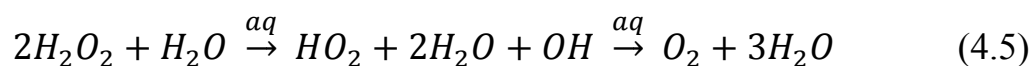
One of the H_2O_2 molecules abstracts a H atom from another H_2O_2 molecule and forms a water molecule, which results in the formation of two radicals (i.e., HO_2 and OH). These radicals then form stable O_2 and H_2O molecules. Thus, the final product of two H_2O_2 molecules will be O_2 and water.

As mentioned above, O_3 species are not followed because of the limitations of the force field used in the simulations. However, it is stated in literature that O_3 species are relatively unstable in aqueous solution and decompose slowly but continuously to oxygen [233]. Furthermore, this stability also depends on the source of water (e.g., pure, tap, buffered, etc.) [233]. The dissolution of O_3, in turn, occurs through a complex mechanism, resulting in the formation of OH, HO_2 and HO_3 radicals [230]. From these considerations, one can say that although the interaction of O_3 species with water was not investigated, the study was performed for the most important active components of O_3, i.e., OH and HO_2 [230], which will be responsible for the reactivity of O_3 in water.

4.3.3 Trajectory of the plasma species in a liquid layer

The trajectories of OH, HO_2 and H_2O_2 species in the water slab are presented in Figure 4.5. The trajectory of the O atom is not presented, as it immediately forms OH radicals. Note that the trajectories are calculated for a long time (i.e., 1.4 ns) in order to reveal whether the above mentioned species can penetrate the water layer or not.

Obviously, all three species can travel through the interface, penetrate deeper and even cross the central line of the water slab (i.e., $z = 36.2$ Å). It can be deduced from Figure 4.5 that the trajectories of the H_2O_2 and HO_2 species are continuous, while the trajectory of the OH radical is composed of broken curves. Indeed, as mentioned above, the OH radicals continuously react with water molecules, abstracting H atoms from water molecules and forming new OH radicals (see Figure 4.3(d)–(f)). When a new OH radical is created the trajectory jumps from the previous OH radical to the new one, resulting in a trajectory discontinuity of ~2 Å, since the average O–H bond length of a water molecule is $d = 0.98$ Å (see [184]). Note that in the calculation of the trajectory, an OH

radical, which is in the intermediate structure is also taken into account (Figure 4.3(e)). Thus, the trajectory of an OH radical is, in fact, the trajectory of numerous short lived OH radicals.
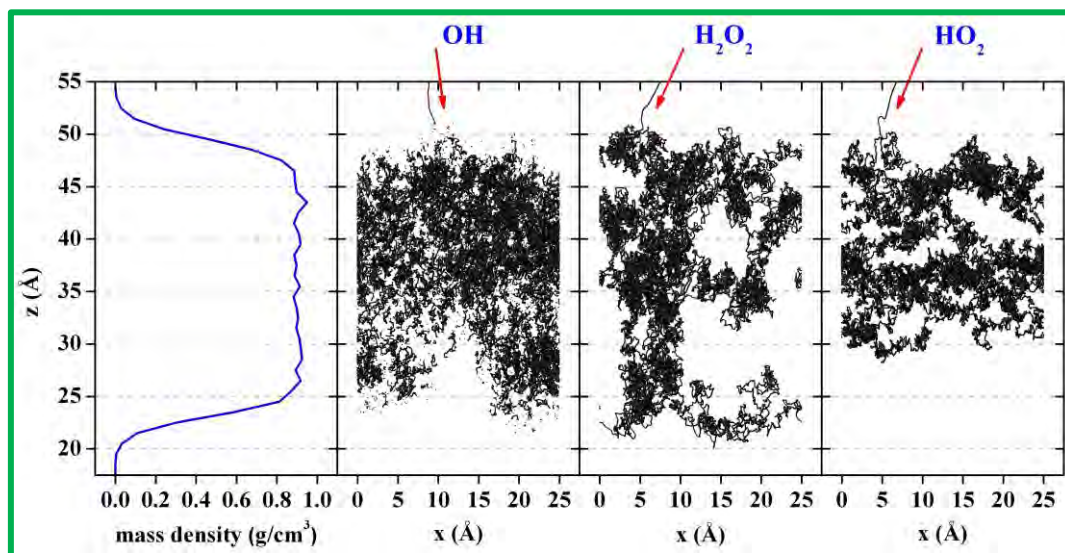
Figure 4.5 *Trajectories of incident OH, H₂O₂ and HO₂ species in water. All species are impacting from the top of the water slab (see red arrows, and cf. Figure 4.1).*
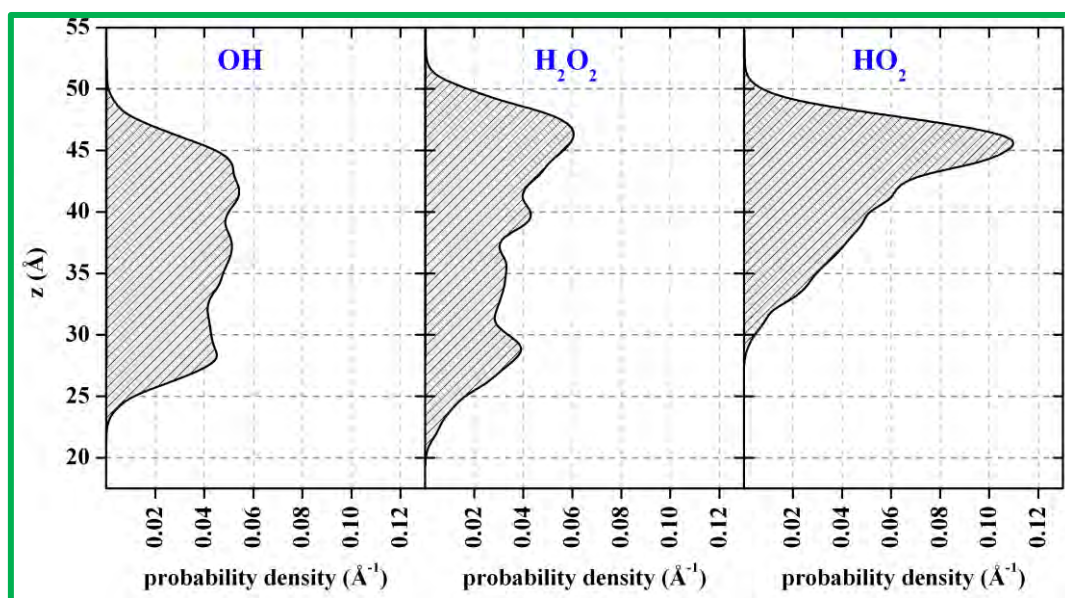
Figure 4.6 *Spatial distribution of the OH, H₂O₂ and HO₂ species along the z-axis in the water slab.*

In Figure 4.6 the spatial distribution of the OH, HO$_2$ and H$_2$O$_2$ species is plotted along the *z*–axis of the simulation box. Each probability density was

obtained by averaging five trajectories. Every trajectory started from the top of the water slab and was integrated for 1.4 ns. Figure 4.6 only illustrates the onset of the transport of the plasma species. Indeed, after a sufficiently long time the graphs would become symmetric.

It is clear that in the case of OH radicals the shape of the shaded area is more or less symmetric (the symmetry line lies at $z = 36.2$ Å, see above), whereas it is more shifted upwards in the cases of H_2O_2 and HO_2. This means that the OH radicals are more rapidly transported than the other two species, and therefore, this species may essentially be found anywhere in the water slab during the simulation time of 1.4 ns. Note that the diffusion of OH radicals is always assisted by chemical reactions (see eqn (4.1) and Figure 4.3(d)–(f)). In contrast to OH radicals, HO_2 radicals are rather found in the interface than in the bulk water, which means that the HO_2 radical is less rapidly transported than the others. Moreover, it was found by Shi *et al.* [234] that it is energetically favorable for the HO_2 radical to bind to the outside of a water cluster, as resulting from the lesser disruption of the water cluster network and a higher stabilization due to hydrogen bridge formation. It is therefore well possible that HO_2 spends more time in the interface than in the bulk water. As can be seen in Figure 4.6, the diffusivity of the H_2O_2 molecule is in between OH and HO_2. This was also observed in this simulation when the MSD (averaged from five runs) as well as the diffusion coefficients of the OH, HO_2 and H_2O_2 species in water, were calculated, which are shown in Figure 4.7.

The calculated diffusion coefficients for OH and H_2O_2 are ~0.84 and ~0.13 $Å^2$/ps, respectively, which correspond well to the values found in the literature (i.e., 0.71 $Å^2$/ps for OH [235], and between 0.13 and 0.15 $Å^2$/ps for H_2O_2 [236-239]).

A value for the diffusion coefficient of HO_2 could not be found in the literature. The performed calculations predict that this value is approximately 2 times less than the diffusion coefficient of H_2O_2 (i.e., ~0.07 $Å^2$/ps). The difference between the calculated value for the diffusion coefficient of OH and the value from ref. [235] is probably due to the fact that their simulation does not take any reactivity of OH into account, so our simulation provides a more realistic description of the system.
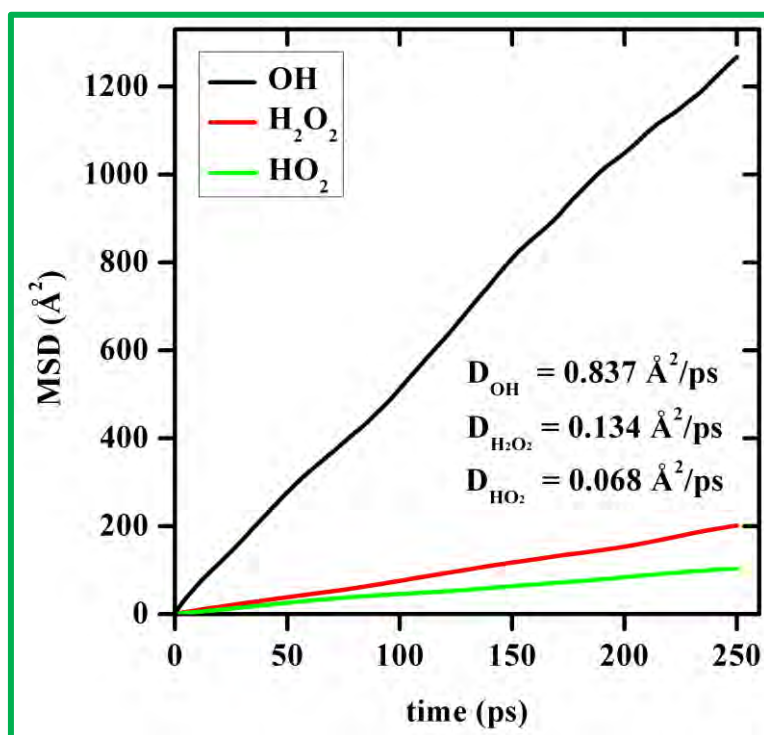
Figure 4.7   *The MSD of the OH, H_2O_2 and HO_2 species in water. The calculated diffusion coefficients are ~ 0.84, 0.13 and 0.07 $Å^2$/ps for OH, H_2O_2 and HO_2, respectively.*

4.4 Conclusions

In conclusion, reactive MD simulations based on the ReaxFF potential were employed in order to study the interaction of ROS (i.e. O, OH, HO_2 and H_2O_2) with water. The bond formation and breaking mechanisms were studied in detail. The performed calculations reveal that O atoms immediately react with water molecules when they reach the surface, resulting in the formation of two OH radicals. OH radicals themselves also react with water, exchanging a hydrogen atom and reforming the reactants (i.e., forming a new OH radical and a water molecule), a process which is continuously repeated. In most cases, HO_2 radicals react with water molecules, forming a superoxide (O_2^-) and hydrated proton (H_3O^+), but recombining back within a few fs to recreate the hydroperoxyl and water molecules. However, an analogue mechanism was also observed, in which this recombination also takes place, but only after the hydrated proton (H_3O^+) is transported through exchanging the H^+ between several water molecules. This can be explained through the continuous

interconversion between hydration complexes, as shown in [231]. H_2O_2 molecules do not react at all, when they are solely surrounded by water molecules. However, when two or three H_2O_2 molecules are in close vicinity of each other, these species react with each other, dissociating into HO_2 radicals and water molecules. HO_2 radicals also react with each other, provided they are sufficiently close to each other in water, forming H_2O_2 and O_2 molecules. OH radicals, on the other hand, do not react with each other, even if they are sufficiently close in a water solution.

The calculated trajectories of the above mentioned species for a long time (i.e., 1.4 ns) have revealed that OH, HO_2 and H_2O_2 can travel through the water layer and eventually reach the surface of bio-molecules. OH and HO_2 radicals travel by forming new OH and HO_2, while H_2O_2 molecules just travel without reaction. The spatial distributions of OH, HO_2 and H_2O_2 have shown that the diffusivity is highest for the OH radicals and lowest for the HO_2 radicals. The diffusion coefficients for OH, H_2O_2 and HO_2 are calculated to be ~0.84, 0.13 and 0.07 Å^2/ps, respectively.

Finally, our calculations predict that the main (i.e., first and second generation) plasma species, which will be present in the liquid layer, and thus can possibly interact with bio-organisms are OH, HO_2, O_2, O_2^-, H_3O^+ and H_2O_2.

Chapter 5

Plasma induced inactivation of lipid A

(Investigation of gram-negative bacteria)

5.1 Introduction

In the present chapter, MD simulations are performed to investigate the interaction of ROS with the endotoxic biomolecule lipid A of the gram-negative bacterium *Escherichia coli* (*E. coli*). Specifically, we study OH and HO_2 radicals, as well as H_2O_2 molecules. These ROS are chosen as they can directly interact with the biomolecule after travelling through the liquid layer (see *chapter 4*). The model system lipid A is the toxic region of lipopolysaccharide (LPS). LPS (or endotoxin) is the outer leaflet of the outer membrane of gram-negative bacteria. It is composed of three parts, namely the inner hydrophobic lipid A, the core oligosaccharide, and the outer O-antigen polysaccharide. The core oligosaccharide connects the outer O-antigen polysaccharide to lipid A. More information about LPS, its toxic region lipid A as well as experimental studies performed on the inactivation of this biomolecule is given in *chapter 1*, *section 1.2*.

It is known that the lipid A of *E. coli* expresses the highest endotoxic activity [100, 240]. This is due to its structure, i.e., the diphosphorylated β(1-6) linked D-glucosamine disaccharide backbone carrying six aliphatic chains. Any deviation from this structure (e.g., the number and length of the fatty acid groups) decreases its toxicity. For instance, the lipid A with a monophosphoryl group is 1000-fold less active than *E. coli* lipid A [100].

Thus, the aim in this chapter is to study whether the ROS may destroy the lipid A structure and thereby decrease its endotoxic activity. Moreover, a comparison and verification of the simulation results to experimental results will also be presented [119-121].

5.2 Computational details

The force field required to correctly describe the specific molecular system of lipid A should contain parameters for C, H, O, N and P atoms. A ReaxFF force field containing parameters for these atoms has been used in the work of Abolfath *et al.* [124]. However, this specific force field appeared not to be suitable for an accurate description of the lipid A system as it was designed to describe DNA and related molecules. To address this problem, two different

force fields are combined in this investigation, i.e., the parameters for the C/H/O/N elements are obtained from [189], which were developed by Rahaman *et al.* for the glycine/water system, whereas the P parameters are adopted from [124].

A schematic picture of the lipid A structure in *E. coli* is presented in Figure 5.1. Its chemical structure can be found in [100, 240]. It is composed of a *β*(1-6) linked D-glucosamine disaccharide carrying two phosphoryl groups (at positions 1 and 4') and substituted with fatty acids, ester-linked at positions 3 and 3', and amide-linked at positions 2 and 2' (see Figure 5.1(b)). These chains are then further substituted by other fatty acids to form the lipid A molecule.
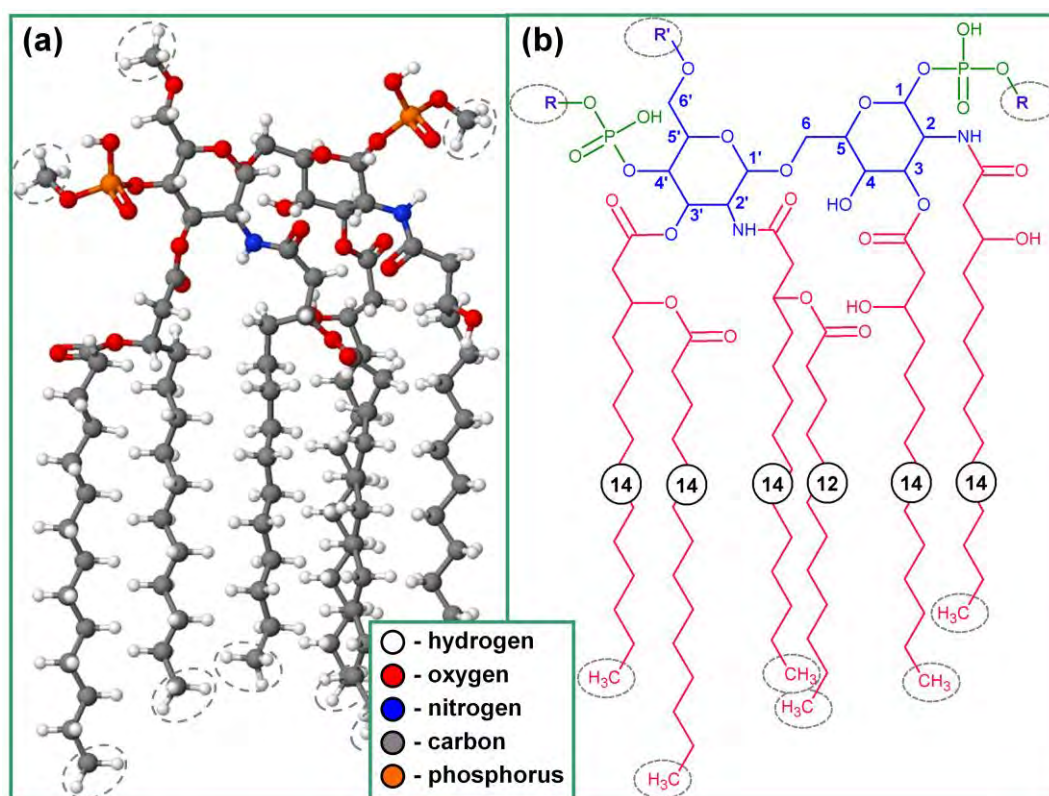
Figure 5.1 *Schematic representation of the lipid A structure (a), and its chemical structure (b).The phosphoryl part, disaccharide backbone and aliphatic chains are indicated in (b) by green, blue and red colors, respectively. This coloring also applies to the other figures below. The repeating parts of the lipid A, as well as the part connected to the oligosaccharide, are designated R and R', respectively, which are substituted by methyl residues (cf. (a)). The number of carbons in the aliphatic chains is indicated in black circles. The fixed H atoms in all methyl residues are indicated in grey dashed circles (see (a) and (b)).*

Hence, in the model structure of lipid A there are two phosphoryl groups (see green color in Figure 5.1(b)) connected to a disaccharide backbone (blue color

in Figure 5.1(b)) carrying six aliphatic chains (red color in Figure 5.1(b)), which are made up of 12-14-carbon chains (see Figure 5.1(b), black circles). As mentioned above, the lipid A is the toxic part of the LPS, which is connected to a long polysaccharide chain, called an O-antigen, by a core oligosaccharide. The polysaccharide chain and core oligosaccharide serve to protect the bacteria, by keeping the structural integrity. However, as we are interested in the toxic part of the LPS, and in order to perform the simulations in a computationally efficient way, focus will only be on the lipid A and the other parts of the LPS will be substituted by methyl residues. In other words, the repeating parts of the lipid A and the part connected to the oligosaccharide (which are specified with R and R', respectively, see Figure 5.1(b)) are replaced by methyl residues (cf. Figure 5.1(a)).

In this MD simulation, the lipid A structure is placed in a box with dimensions 50 Å × 70 Å × 40 Å. This box size is large enough to place the incident plasma species around the structure (see below). PBC are not applied in any direction as no infinite structure is needed in the simulations. However, to prevent translation and geometric deformation of the lipid A (leading to a loss of the geometric agreement with experimental lipid A found in the cell membrane [100, 240]), parts of the structure are spatially fixed during the simulation (see dashed circles in Figure 5.1).

Prior to the particle impacts, the lipid A structure is equilibrated at room temperature for 500 ps in the canonical ensemble, employing the Bussi thermostat [145] with a coupling constant of 100 fs. Both during the thermalization as well as during the particle impact simulations, a time step of 0.25 fs is used. To obtain statistically valid results for bond-dissociation processes and to study all possible damaging mechanisms of the lipid A, 100 runs are performed for each impinging species. At the beginning of each run, 10 incident particles of a single species (e.g., ten OH radicals) are randomly positioned at a distance of at least 10 Å around the structure and from each other, to prevent interactions (including long range interactions, i.e., Coulomb and van der Waals interactions) between the plasma species and the lipid A structure prior to the impact. The velocity directions of incident species are chosen randomly while their initial energy corresponds to room temperature. Every simulation trajectory lasts 500 ps, corresponding to 2×10^6 iterations, in the canonical ensemble; it was carefully checked that this time is long enough to

obtain a chemically destroyed lipid A structure, at least until one critical bond in the structure is broken (see below).

5.3 Results and discussions

As mentioned above, the impinging plasma species in this work are OH, HO_2 and H_2O_2. Other ROS, such as O and O_3, as well as RNS, are also known to have bactericidal effects (see e.g., [31, 221, 222]). Moreover, O_2 and H_2O molecules can also be of interest, as they are naturally found around bacteria. However, these species are not considered in the present chapter for the following three reasons. First, the investigations on the H_2O and O_2 impacts revealed that no bond-breaking events occur in the lipid A. These molecules are found to assemble around the lipid A, having only weak attractive non-bonded interactions with the structure, which was also observed in our previous studies (see *chapter 3*). Second, there is no need to show the bond-breaking mechanisms for O atoms, as it was found in the previous simulations (see *chapter 3*) that O radicals exhibit the same mechanisms as the OH radicals. To validate the latter, test runs were performed for O atom impacts on lipid A, and the same bond dissociation mechanisms as for the OH radicals were indeed observed. Furthermore, our previous simulations (see *chapter 4*) indicated that O atoms cannot reach the biomolecule surface, travelling through the water layer. Instead, they immediately interact with water molecules, resulting in the formation of two OH radicals. Finally, O_3 and RNS are not included in the present work, as the force field used in current simulation does not accurately describe the behavior of these species. In the following subsections the most frequently observed bond-breaking mechanisms will be shown.

5.3.1 Damage of the head group (i.e., disaccharide and phosphoryl groups) of lipid A

The most frequently occurring interaction mechanism of OH radicals with the disaccharide part is presented in Figure 5.2.
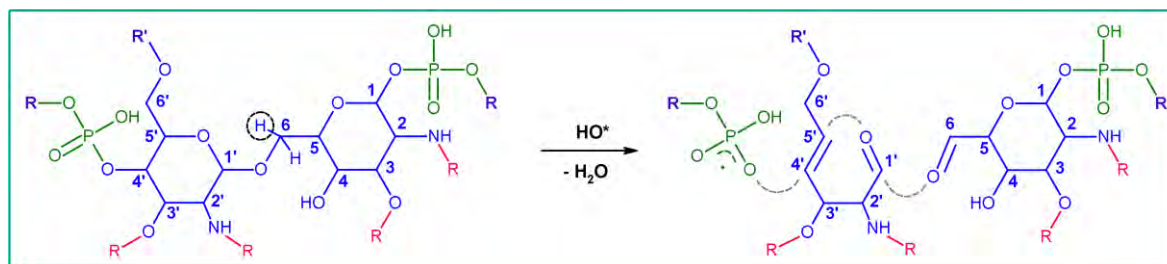
Figure 5.2   *Breaking mechanism of three C–O bonds in the disaccharide part (see blue color and cf. Figure 5.1(b)) upon impact of an OH radical. The OH radical abstracts an H atom (see black dashed circle) leading to the formation of a water molecule. This subsequently results in the cleavage of three C–O bonds (see gray dashed lines) and the formation of two double C=O bonds and one double C=C bond. The aliphatic chains are substituted in this figure with R (see red color and cf. Figure 5.1(b)), for the sake of clarity. This mechanism occurred in 2.1% of the OH radical impact cases (and in 1.2% of the HO_2 impact cases).*

After the H-abstraction reaction by the OH radical (see black dashed circle in Figure 5.2) a water molecule is formed. Subsequently, this leads to the consecutive breaking of three C–O bonds (see gray dashed lines), as well as the formation of double C=C and C=O bonds. From the 100 simulations (i.e., 100×10 impacts, see above), this bond-cleavage mechanism occurs 21 times. In other words, in 2.1% of the OH radical impact cases the bond-breaking mechanism shown in Figure 5.2 occurs.

A similar bond-dissociation mechanism was observed in the case of the HO_2 radical impacts. H-abstraction takes place by the HO_2 radical, leading to the formation of a H_2O_2 molecule and dissociation of C–O bonds, as shown in Figure 5.2. This mechanism occurs 12 times in the case of the HO_2 radicals over 100 simulations, i.e., from 1000 HO_2 radical impacts. Hence, the mechanism shown in Figure 5.2 happens in 1.2% of the cases.

In Figure 5.3 the most frequently observed bond-breaking mechanism in the disaccharide by HO_2 radicals is depicted.

After the H-abstraction from the HO_2 radical by an O atom in the ether group of the disaccharide (see Figure 5.3, black dashed circle) an O_2 molecule is formed. This leads to the dissociation of two C–O bonds (see gray dashed lines), the formation of a double C=C bond and a new hydroxyl group. Note that this mechanism is observed in the simulations 28 times over the 100 runs (i.e., 1000 impacts). In other words, in 2.8 % of the 1000 HO_2 radical impacts the mechanism illustrated in Figure 5.3 occurs.

97
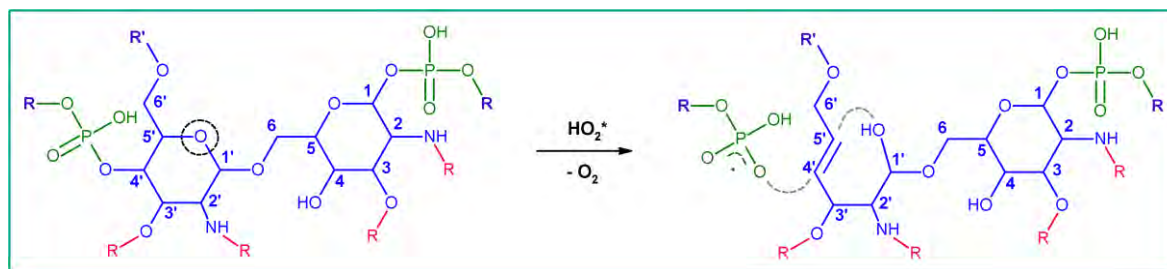
Figure 5.3 *Breaking mechanism of two C–O bonds in the disaccharide part (see blue color and cf. Figure 5.1(b)) upon impact of a HO₂ radical. The 1'-5' ether O atom (see black dashed circle) abstracts the H atom from the HO₂ radical, leaving an O₂ molecule. Subsequently, this leads to the breaking of two C–O bonds (see gray dashed lines) and the formation of a double C=C bond and a new OH group. The aliphatic chains are substituted in this figure with R (see red color and cf. Figure 5.1(b)), for the sake of clarity. This mechanism occurred in 2.8% of the HO₂ impact cases (and in 1.2% of the H₂O₂ impact cases).*

Another frequently observed bond-cleavage mechanism in the disaccharide part upon impact by HO_2 radicals is presented in Figure 5.4.
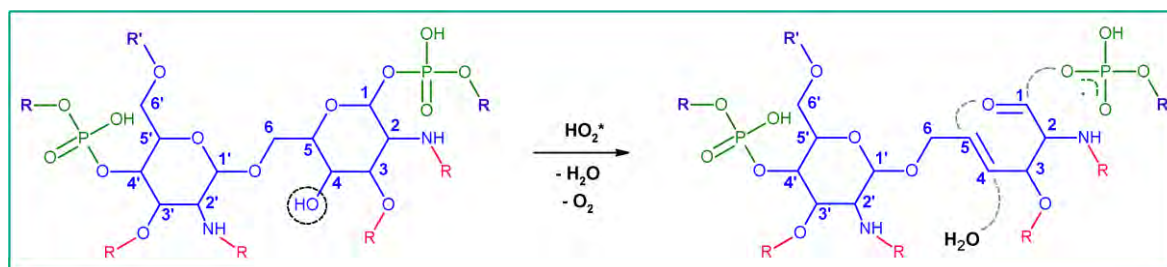
Figure 5.4 *Breaking mechanism of three C–O bonds in the disaccharide part (see blue color and cf. Figure 5.1(b)) upon impact of a HO₂ radical. The OH residue of D-glucosamine connected to the carbon atom at position 4 (see black dashed circle) abstracts the H atom from the HO₂ radical, forming an O₂ molecule. Subsequently, this leads to the breaking of three C–O bonds (see gray dashed lines). Note that one of the C–O bonds is broken due to the detachment of a water molecule. The aliphatic chains are substituted in this figure with R (see red color and cf. Figure 5.1(b)), for the sake of clarity. This mechanism occurred in 3.5% of the HO₂ impact cases (and in 2.5% of the H₂O₂ impact cases).*

Again the H-abstraction reaction from the HO_2 radical takes place, now by the OH group of D-glucosamine (see black dashed circle in Figure 5.4). This leads to the cleavage of three C–O bonds; one in the ether group, one connected to the phosphoryl group and the third one by the detachment of a water molecule (see gray dashed lines in Figure 5.4). This mechanism occurs 35 times over the

100 runs (or 1000 HO_2 radical impacts). Thus, in 3.5 % of the 1000 HO_2 radical impacts the mechanism illustrated in Figure 5.4 takes place.

Similar bond-cleavage mechanisms as shown in Figure 5.3 and Figure 5.4 are also obtained for the H_2O_2 molecules. The only difference is that the H-abstraction reaction can now take place in two ways, i.e., either directly from the H_2O_2 molecule (in 10–20% of the cases), or from a HO_2 radical, which is formed by the reaction of H_2O_2 molecules between each other. The latter is more likely to be seen (i.e., in 80–90% of the cases). Moreover, when three H_2O_2 molecules assemble around the lipid A structure, they react with each other, dissociating into HO_2 radicals and water molecules. Subsequently, one of the HO_2 radicals can react with the lipid A structure, causing the breaking of the bonds as described in Figure 5.3 and Figure 5.4. A similar dissociation mechanism of the H_2O_2 molecule was observed in our previous work (see *chapter 3, section 3.5*).

In the case of the H_2O_2 molecules the mechanisms presented in Figure 5.3 and Figure 5.4 occur 12 and 25 times, respectively, over the 100 simulations, i.e., from the 1000 H_2O_2 molecule impacts. In other words, in 1.2% and 2.5% of the cases, the above mentioned bond-breaking mechanisms occur upon H_2O_2 impacts.

In summary, the OH, HO_2 and H_2O_2 plasma species can dissociate the C–O bonds and cause the detachment of the phosphate groups, resulting in the destruction of disaccharide part and the formation of water and oxygen molecules. This, in turn, leads to a decrease in O–C–O groups (see Figure 5.2 and Figure 5.4) and the formation of new C=C and C=O bonds, and therefore also to a decrease in the total number of C–C and C–H bonds. Note that the above mechanisms typically occurred in a few % of the impacts, which means that these ROS are quite effective in breaking C–O bonds in the disaccharide part of lipid A, and in detaching the phosphoryl groups.

5.3.2 Detachment of the aliphatic chains in lipid A

The most frequently occurring interaction mechanism of OH radicals with the aliphatic chain is presented in Figure 5.5.
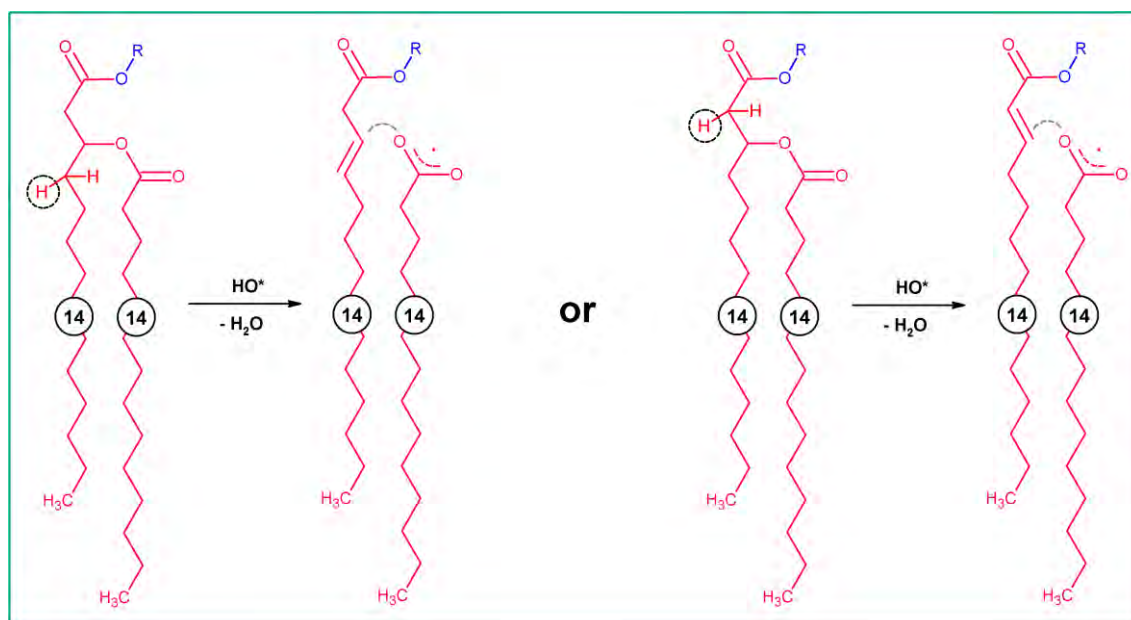
**Figure 5.5**   *C–O bond breaking mechanism in the aliphatic chain (see red color and cf. Figure 5.1(b)) upon impact of an OH radical. The OH radical abstracts one of the H atoms (see black dashed circles), which are close to the ester group, and a water molecule is formed. This, in turn, leads to the formation of a double C=C bond, as well as the cleavage of a C–O bond (see gray dashed lines), hence detachment of an aliphatic chain. The disaccharide is substituted in this figure with R (see blue color and cf. Figure 5.1(b)), for the sake of clarity. This mechanism occurred in 1.7% of the OH radical impact cases, but was almost negligible in the case of the HO_2 and H_2O_2 impacts.*

A H atom positioned close to the ester is abstracted (see black dashed circles). This leads to the formation of a double C=C bond and the dissociation of a C–O bond in the ester, i.e., detachment of an aliphatic chain. A similar C–O bond-breaking mechanism can occur from the ester of the aliphatic chain with 12 carbons (see Figure 5.1(b)). This mechanism is observed in the simulations 17 times over the 100 runs, i.e., the detachment of the aliphatic chains occurs in 1.7% of the cases of 1000 OH radical impacts. Desorption of the aliphatic chains is only seen in a limited number of cases after impact of HO_2 and H_2O_2.

Thus, we can conclude that OH radicals can react with the H atom, which is closely positioned to the ester, and can lead to the detachment of the aliphatic chains, either as $C_{14}H_{27}O_2^{\bullet}$ or $C_{12}H_{23}O_2^{\bullet}$. This results in a decrease of the total

number of ester (O–C=O) groups. On the other hand, detachment of the aliphatic chains after HO_2 or H_2O_2 impacts is almost negligible.

5.3.3 General discussion and comparison with experiments

Table 5.1 presents the number of C–O and C–H bonds broken upon impact of OH, HO_2 and H_2O_2 species, per impacting particle. It should be mentioned that in this work ten impinging particles (e.g., ten OH radicals) hit the surface (almost) simultaneously, so more than one bond-breaking event can occur within one simulation (i.e., within the total simulation time of 500 ps). To take this into account the total number of broken bonds is divided per simulation by ten. Thus, in the following, all bond-breaking events per particle impact will be reported. Note that in total there are 29 C–O bonds and 177 C–H bonds in the structure. Hence, it looks as if the chance of bond-breaking is not very large (around 1% or lower), but the cleavage of even a single C–O bond could possibly destroy the structure and therefore reduce already the toxicity of lipid A, and moreover, in reality several plasma species can impact at the same time. Indeed, if any of the aforementioned mechanisms (see Figures 5.2–5.5) take place, this will most likely eventually result in a decrease of the toxicity of lipid A. For instance, as mentioned above, the lipid A with a monophosphoryl group (see mechanisms shown in Figures 5.2–5.4) is 1000-fold less active than *E. coli* lipid A [100]. Moreover, the number of aliphatic chains has a direct effect on the toxicity of lipid A; a structure with six fatty acid groups expresses the optimal endotoxic activity.

Table 5.1   *Average number of dissociated C–O and C–H bonds upon impact of OH, HO_2 and H_2O_2 plasma species. The values are calculated per impacting particle for a simulation time of 500 ps, and are averaged over 100 independent simulations (i.e., 1000 impacts in total).*

incident plasma species	number of broken C–O bonds	number of broken C–H bonds
OH	0.16	0.55
HO_2	0.38	0.1
H_2O_2	0.25	0.02

The length of the fatty acid chains is also important for the toxicity, as C_{12}, $C_{12}OH$, C_{14}, and $C_{14}OH$ fatty acids are those found in the most toxic lipid A structures [241].

It is obvious from Table 5.1 that the HO_2 radicals are more effective in breaking C–O bonds, followed by the H_2O_2 molecules, while the OH radicals are less effective. This was also clear from the discussion above (*subsection 5.3.1*), because more mechanisms for C–O bond-breaking exist in the disaccharide part upon HO_2 impact than upon OH impact. On the other hand, in the case of the C–H bond-breakings, the OH radicals are clearly more effective, followed by HO_2 and H_2O_2. This is again logical, as the OH radicals always start with H-abstraction from the structure, whereas in the case of HO_2 and H_2O_2 impact, the mechanism starts with H-abstraction from the impacting species.

It should be mentioned that in this work, no C–C and P–O bond-breaking events are observed upon impact of OH, HO_2 and H_2O_2 species. Moreover, the cleavage of C–N bonds was found to be negligible compared to C–O bond-breaking, i.e., the dissociation of C–N bonds occurs only few times for the cases of HO_2 and H_2O_2 impact, whereas no C–N bonds are broken in the case of OH radicals.

Table 5.2   *Percentages of the bond-breaking mechanisms shown in Figures 5.2–5.5 (see above). Note that the values are calculated for a simulation time of 500 ps.*

bond-breaking mechanism	incident plasma particle	occurrence (%)
Figure 5.2	OH	2.1
	HO_2	1.2
	H_2O_2	0
Figure 5.3	OH	0
	HO_2	2.8
	H_2O_2	1.2
Figure 5.4	OH	0
	HO_2	3.5
	H_2O_2	2.5
Figure 5.5	OH	1.7
	HO_2	negligible
	H_2O_2	negligible

The percentages of the bond-breaking processes/mechanisms, which are shown in Figures 5.2–5.5, are given in each figure caption and summarized here in Table 5.2.

It is worth noting that in each of these mechanisms at least one and maximum three C–O bonds are dissociated (see Figures 5.2–5.5). It should also be mentioned that here only the most frequently occurring bond-cleavage mechanisms are shown.

Finally, the comparison of the simulation results with experimental observations [119-121] shows in general good qualitative agreement. Indeed, Bartis *et al.* reported that reactive oxygen species are required for deactivation of LPS in the APPJ [121]. The authors have also shown a decrease in C–C/H and a slight decrease in the O–C–O/N–C=O and O–C=O bonding, by means of XPS, while the C–O/C=O groups increased when treating LPS with ROS [121] (see Figure 1.7 in *chapter 1*). It can be assumed that the decrease in C–C and C–H groups is probably due to the following. All bond-breaking mechanisms upon impact of OH radicals are initiated by the dissociation of C–H bonds (i.e., the H-abstraction reactions; see Figure 5.2 and Figure 5.5 above). This leads, among others, to the formation of double C=C bonds. Hence, the total number of C–C and C–H bonds will decrease (which causes a decrease in the C–C and C–H signals in the XPS spectra), despite the fact that the direct breaking of C–C bonds (at least for OH, HO_2 and H_2O_2 impacts) is not seen. On the other hand, the breaking of O–C–O bonds (see Figure 5.2 and Figure 5.4), as well as the detachment of aliphatic chains (i.e., breaking of O–C=O groups (see Figure 5.5)) are observed, which is in agreement with the XPS measurements [121]. Moreover, this bond-breaking leads to the formation of double C=O bonds (i.e., increase in C=O groups, which is also observed in [121]). The increase in C–O groups, in this work, is observed only for the OH radical impacts (i.e., not for the HO_2 and H_2O_2 impacts) and it occurs solely in the aliphatic chains. This C–O increase is due to the creation of new hydroxyl groups in the aliphatic chains. The mechanism is as follows. One of the OH radicals abstracts the H atom from a $-CH_2-$ group of the aliphatic chain (see Figure 5.1), leading to the formation of a $-HC•-$ radical. Subsequently, another OH radical attaches to the $-HC•-$ radical, resulting in the formation of a new hydroxyl group (i.e., a new C–O bond). This mechanism is observed in this simulation 9 times out of 1000 OH radical impacts (i.e., in 0.9% of the cases). A similar mechanism was also observed in the test simulations with O radicals. O atom can abstract the H atom

from the aliphatic chain and immediately attach to it, leading to the formation of new hydroxyl group. Moreover, O atoms can also break the C–C bonds in the aliphatic chains and form carbonyl groups (i.e., new C=O bonds).

It needs to be stressed here that the experiments were performed on LPS, where interactions between the reactive species and the O-antigen and/or the core oligosaccharide are also possible. This can result in the formation of new C–O/C=O groups, as well as the dissociation of C–C bonds.

The simulation results were also compared with the experimental work by Chung *et al.* [120], as they studied the effects of VUV radiation, oxygen and deuterium radicals on the endotoxic biomolecule lipid A. These authors found that the phosphate moieties and intact aliphatic chains all decreased significantly in the case of radical exposures (mainly due to O radicals, see Figure 1.6 in *chapter 1*) even more than that of the VUV-treated samples [120]. This was also observed in this work, especially upon impact of the OH radicals, which have the same reaction mechanisms as the O radicals.

Finally, no bond-breaking events in the phosphoryl groups (i.e., no P–O bonds were broken) as well as negligible breaking of the C–N bonds were observed, which is consistent with the observations of Bartis *et al.*, who also reported that the radical treatment did not significantly affect the phosphorous and nitrogen content, in contrast to direct and UV/VUV treatments of LPS [119].

5.4 Conclusions

The interaction of ROS, and more specifically OH and HO_2 radicals as well as H_2O_2 molecules, with the lipid A structure was investigated on the atomic level by means of reactive MD simulations. It was found that these plasma species can destroy the lipid A structure, which leads to a decrease of its toxicity. Destruction of different parts of the lipid A structure, namely the hydrophilic head (i.e., the disaccharide and phosphoryl groups) and the aliphatic chains, were thoroughly investigated, for the impacts of OH, HO_2 and H_2O_2 species. It was also found that the interaction mechanisms are in all cases initiated by H-abstraction reactions, which mainly take place from the impinging

particle itself in the cases of HO_2 and H_2O_2 by the lipid A structure, whereas in the case of OH radicals, the radical abstracts the H atom from the lipid A structure. The obtained results are in good qualitative agreement with experimental observations [119-121]. Therefore, our simulations can be useful for improving our understanding about the destruction mechanisms of lipid A molecules, and hence, to obtain a better insight in the antibacterial properties of plasmas.

Summary

The application of cold atmospheric pressure plasmas in medicine requires control over the processes occurring in the plasma and more importantly at the surface of living cells.

Despite many experimental studies that have been performed in plasma medicine (e.g., in inactivation of bacteria), there is still very little fundamental knowledge regarding the relevant interaction mechanisms of plasma species with biomolecules. Complementary to experimental studies, computer simulations may provide fundamental information about the occurring processes, both in the plasma and at the surface of biomolecules, which is difficult or even impossible to obtain through experiments.

Based on these considerations, I studied in this work, the interaction mechanisms of important plasma species with the surface of living organisms.

The outer surface of bacteria was chosen as the (main) model system, since plasma species can directly and initially interact with them. An important structure of the outer part of gram-positive bacteria is peptidoglycan (PG), whereas in gram-negative bacteria it is lipopolysaccharide (LPS). The most important part of LPS is lipid A, as this is responsible for its endotoxicity. Destruction of these structures can thus lead to the deactivation of bacteria. It is also known that most bio-organisms, including bacteria, are coated by a liquid film (composed mostly of water) surrounding them, and there might be many interactions between plasma species and the liquid layer before the plasma species reach the surface of the bio-organisms. Therefore, it is also essential to study the behaviour of the reactive species in water, in order to determine whether these species can travel through this layer and reach the biomolecules, or whether new species are formed along the way.

Thus, in this work I studied the interaction of important plasma species with *PG*, *lipid A* and a *water layer* by means of reactive molecular dynamics simulations, aiming for a better understanding of plasma disinfection. The plasma species under study were reactive oxygen species (ROS), namely O, OH, O_3, HO_2, H_2O_2 as well as O_2 and H_2O.

The interaction of ROS with PG. The interaction mechanisms of ROS with PG were thoroughly investigated. It was found that O_2 and H_2O molecules cannot structurally damage the PG structure, but only engage in non-bonding interactions with PG through hydrogen bridge formation. The other plasma species, i.e., O, O_3, OH, and H_2O_2, are found to break structurally important bonds of PG (i.e., C−O, C−C, or C−N bonds), which subsequently leads to destruction of the bacterial cell wall. The performed calculations revealed that O_3, OH, and especially O atoms are more effective in bond cleavage than H_2O_2 molecules, in agreement with many experiments demonstrating the crucial role of reactive oxygen species (such as O and OH) in bacterial deactivation.

Furthermore, the ether C−O bonds in the disaccharide part of the PG are found to break up more easily, followed by the C−C bonds and C−N bonds. In the case of H_2O_2 molecules, no C−N bond-breaking events were observed, indicating again that the H_2O_2 molecules are somewhat less effective in bacterial cell wall destruction. However, in contrast with the highly reactive O radicals, H_2O_2 molecules are stable species in an aqueous environment and are thus more likely to interact directly with PG. Hence, it is expected that the H_2O_2 molecules are also very important for bacterial deactivation.

The interaction of ROS with a water layer. The interaction mechanisms of ROS (i.e. O, OH, HO_2 and H_2O_2) with water were also studied in detail. It was found that O atoms immediately react with water molecules when they reach the surface, resulting in the formation of two OH radicals. OH radicals themselves also react with water, exchanging a hydrogen atom and reforming the reactants (i.e., forming a new OH radical and a water molecule), a process which is continuously repeated. In most cases, HO_2 radicals react with water molecules, forming a superoxide (O_2^-) and hydrated proton (H_3O^+), but recombining back within a few fs to recreate the HO_2 and H_2O molecules. An analogue mechanism was observed in which this recombination also takes place, but only after the hydrated proton (H_3O^+) is transported through exchanging the H^+ between several water molecules. H_2O_2 molecules do not react at all, when they are solely surrounded by water molecules. However, when two or three H_2O_2 molecules are in close vicinity of each other, they react with each other, dissociating into HO_2 radicals and water molecules. HO_2 radicals also react with each other, provided they are sufficiently close to each other in water, forming H_2O_2 and O_2 molecules. OH radicals, on the other hand, do not react with each

other, even if they are sufficiently close, at least within the simulation time of 100 ps.

The trajectories of the above mentioned species followed over a long time (i.e., 1.4 ns), revealed that OH, HO_2 and H_2O_2 can travel through the water layer and eventually reach the surface of biomolecules. OH and HO_2 radicals travel by forming new OH and HO_2, while H_2O_2 molecules just travel without reaction. The spatial distributions of OH, HO_2 and H_2O_2 demonstrated that the diffusivity is the highest for the OH radicals and lowest for the HO_2 radicals. The diffusion coefficients for OH, H_2O_2 and HO_2 are calculated to be ~0.84, 0.13 and 0.07 $Å^2$/ps, respectively. These values are in reasonably good agreement with literature.

Finally, our calculations predict that the main plasma species which will be present in the liquid layer, and thus can possibly interact with bio-organisms, are OH, HO_2, O_2, O_2^-, H_3O^+ and H_2O_2.

The interaction of ROS with lipid A. The interaction of OH, HO_2 and H_2O_2 with the lipid A structure was also investigated on the atomic scale. It was found that these plasma species can destroy the lipid A structure, which leads to a decrease of its toxicity. Destruction of different parts of the lipid A structure, namely the hydrophilic head (i.e., the disaccharide and phosphoryl groups) and the aliphatic chains, was thoroughly investigated. It was also found that the interaction mechanisms are in all cases initiated by H-abstraction reactions, which mainly take place from the impinging particle itself in the cases of HO_2 and H_2O_2 by the lipid A structure, whereas in the case of OH radicals, the radical abstracts the H atom from the lipid A structure. The obtained results are in good qualitative agreement with experimental observations. Our simulations can therefore be useful for improving our understanding of the destruction mechanisms of lipid A molecules, and hence, to obtain a better insight in the antibacterial properties of plasmas.

We can in general conclude from the above mentioned studies on the interaction of plasma generated ROS with PG, lipid A and a water layer that these reactive species are able to destroy the outer cell membrane components, and thus can lead to the deactivation of these organisms. All interaction mechanisms are found to be initiated by H-abstraction reactions. This, in turn, leads to the breaking of structurally important bonds in the molecules. The mechanisms behind these breakups are, however, dependent on the impinging

plasma species, and this also determines the effectiveness of the bond dissociation and hence their bactericidal effect.

These computational studies contribute to improve our fundamental insight into the interaction mechanisms of the above mentioned structures with plasma-generated species at the atomic level.

Finally, the performed investigations demonstrate that such atomic scale simulations provide valuable insight into the details of the microscopic events that occur in the plasma treatment of bacteria. This in turn is important to gain insight into the fundamental operating mechanisms in plasma medicine in general.

Outlook for future work. In subsequent studies, simulating the interaction of plasma species with more complex and larger structures may be envisaged. An example of such a more complex structure is the phospholipid bilayer, which is the layer underneath the PG (or LPS) in bacteria. Moreover, liquid films or biofilms covering bacteria are not composed of only water but actually have a quite complex structure and composition. It consists of a conglomeration of different types of biopolymers that forms the scaffold for the three-dimensional architecture of the biofilm and is responsible for adhesion to surfaces and for cohesion in the biofilm. Hence the study of breaking-up this structure by cold atmospheric plasmas is also of importance for the further development of plasma medicine.

Samenvatting

De toepassing van koude plasma's bij atmosfeerdruk in de geneeskunde vereist een goede controle over de processen die plaatsgrijpen in het plasma zelf, alsook aan het oppervlak van de behandelde cellen en weefsels.

Ondanks de vele experimentele studies in plasmageneeskunde, o.a. voor de inactivatie van bacteriën, is het fundamentele inzicht in de onderliggende mechanismen vooralsnog ruimschoots ontoereikend. Computer simulaties kunnen erg gedetailleerde informatie leveren omtrent deze mechanismen en processen. Deze informatie is enerzijds vaak complementair aan de beschikbare experimentele gegevens, maar anderzijds bovendien experimenteel soms slechts zeer moeilijk of zelfs onmogelijk te bekomen.

Daarom heb ik in dit werk de interactiemechanismen van belangrijke plasmadeeltjes met het oppervlak van bacteriën onderzocht.

Als modelsysteem heb ik het oppervlak van bacteriën gekozen, vermits plasmadeeltjes hiermee direct kunnen interageren, en dit ook de eerste structuren zijn waarmee plasmadeeltjes zullen interageren. Een belangrijke structuur aan het oppervlak van grampositieve bacteriën is peptidoglycaan (PG). In gramnegatieve bacteriën is lipopolysaccharide (LPS) een belangrijke structuur. Het belangrijkste onderdeel van LPS is lipide-A, vermits dit deel verantwoordelijk is voor de endotoxiciteit van LPS. Afbraak van deze structuren kan leiden tot de deactivatie van bacteriën. Daarnaast is geweten dat de meeste bio-organismen (met inbegrip van bacteriën) omgeven worden door een vloeibare film (de zogenaamde biofilm), die hoofdzakelijk bestaat uit water. Vooraleer de plasmadeeltjes het eigenlijke bio-organisme bereiken, zullen ze dus eerst interageren met deze biofilm. Daarom is het essentieel om ook het gedrag van de plasmadeeltjes met water te bestuderen, om zo te bepalen of de plasmadeeltjes doorheen de waterlaag kunnen getransporteerd worden en zo de biomoleculen kunnen bereiken, en of er mogelijkerwijze onderweg nieuwe deeltjes gevormd worden.

Daarom heb ik in dit werk de interactie van belangrijke plasmadeeltjes met *PG, lipide-A* en *een waterlaag* bestudeerd aan de hand van reactieve moleculaire dynamica simulaties, gericht op een beter inzicht in plasma desinfectie. De bestudeerde plasmadeeltjes zijn reactieve zuurstofdeeltjes ("Reactive Oxygen

Species", of ROS), en in het bijzonder O, OH, O_3, HO_2, H_2O_2, alsook O_2 en H_2O.

De interactie van ROS met PG. De interactiemechanismen van ROS met PG zijn in detail bestudeerd. Uit de simulaties blijkt dat O_2 en H_2O geen structurele schade toebrengen aan PG, maar enkel niet-bindende interacties aangaan door middel van waterstofbruggen. De andere plasmadeeltjes, nl. O, O_3, OH en H_2O_2, veroorzaken wel de dissociatie van structureel belangrijke bindingen in PG, nl. van C–O, C–C en C–N bindingen. Deze dissociaties kunnen vervolgens leiden tot een afbraak van de bacteriële celwand. De uitgevoerde simulaties tonen aan dat O_3, OH en in het bijzonder O effectiever zijn in het breken van bindingen dan H_2O_2, in overeenstemming met vele experimenten die de cruciale rol van ROS zoals O en OH in bacteriële deactivatie aantonen.

Daarnaast werd vastgesteld dat de ether C–O bindingen in het disaccharide gedeelte van PG gemakkelijker breken, gevolgd door de C–C bindingen en de C–N bindingen. In het geval van H_2O_2 moleculen werden geen C–N dissociaties waargenomen, hetgeen opnieuw bevestigt dat H_2O_2 minder effectief is in het opbreken van de bacteriële celwand. In tegenstelling tot de erg reactieve O radicalen echter, zijn H_2O_2 moleculen deeltjes die stabiel zijn in een waterige omgeving, en dus een grotere waarschijnlijkheid vertonen om direct met PG te interageren. Daarom wordt verwacht dat ook de H_2O_2 moleculen erg belangrijk zijn voor bacteriële deactivatie.

De interactie van ROS met een waterlaag. De interactiemechanismen van ROS (nl. O, OH, HO_2 en H_2O_2) met water zijn ook in detail bestudeerd. Er werd gevonden dat O atomen onmiddellijk met watermoleculen reageren wanneer ze het wateroppervlak bereiken, ter vorming van twee OH radicalen. Ook OH radicalen zelf reageren met water, waarbij een waterstofatoom wordt uitgewisseld en de uitgangsproducten zo opnieuw gevormd worden in een continu proces. In de meeste gevallen reageren ook HO_2 radicalen met water moleculen, waarbij een superoxide (O_2^-) en een gehydrateerd proton (H_3O^+) gevormd worden. Deze produkten reageren echter bijna instantaan terug om zo opnieuw HO_2 en H_2O te vormen. Er werd ook een analoog mechanisme waargenomen waarin dezelfde recombinatie plaatsgrijpt, maar slechts nadat het gehydrateerde proton doorheen de waterlaag getransporteerd is door de uitwisseling van H^+ tussen verscheidene watermoleculen. H_2O_2 moleculen reageren helemaal niet wanneer ze louter door H_2O moleculen omgeven worden.

Wanneer zich echter twee of drie H_2O_2 moleculen in elkaars nabijheid bevinden, kunnen deze met elkaar reageren, waarbij ze dissociëren in HO_2 radicalen en watermoleculen. HO_2 radicalen interageren ook met elkaar, op voorwaarde dat ze zich voldoende dicht in elkaars nabijheid bevinden. Hierbij wordt dan H_2O_2 en O_2 gevormd. OH radicalen echter reageren nooit met elkaar, zelfs wanneer ze zich voldoende dicht bij elkaar bevinden – ten minste niet in de simulatietijd van 100 ps.

Door het volgen van de moleculaire trajecten over een lange tijd (1.4 ns), kon worden vastgesteld dat OH, HO_2 en H_2O_2 doorheen de waterlaag kunnen getransporteerd worden en zo de biomolecule of het oppervlak van de cel kunnen bereiken. OH en HO_2 radicalen bewegen door het water door de continue vorming van nieuwe OH en HO_2 radicalen, terwijl H_2O_2 moleculen eenvoudigweg doorheen het water diffunderen zonder enige reactie te ondergaan. De berekende ruimtelijke verdelingen van OH, HO_2 en H_2O_2 tonen aan dat de diffusiviteit van OH het hoogst is, en die van HO_2 het laagst is. De berekende diffusiecoëfficiënten van OH, HO_2 en H_2O_2 zijn ~0.84, 0.13 en 0.07 $Å^2$/ps, hetgeen in goede overeenkomst is met de literatuur.

Tenslotte tonen deze berekeningen aan dat de belangrijkste plasmadeeltjes die aanwezig zullen zijn in de waterlaag en dus mogelijk kunnen interageren met de bio-organismen of cellen OH, HO_2, O_2, O_2^-, H_3O^+ en H_2O_2 zijn.

De interactie van ROS met lipide-A. De interactie van OH, HO_2 en H_2O_2 met lipide-A is ook bestudeerd op atomaire schaal. De simulaties tonen aan dat deze plasmadeeltjes de lipide-A structuur kunnen opbreken, hetgeen leidt tot een vermindering van zijn toxiciteit. De afbraak van verschillende delen van het lipide-A, namelijk de hydrofiele kop (d.w.z., het disaccharide en de fosforylgroepen) en de alifatische ketens, is in detail bestudeerd. Er werd gevonden dat de interactiemechanismen in alle gevallen geïnitieerd worden door H-abstractie reacties. In het geval van HO_2 en H_2O_2, wordt het H-atoom hoofdzakelijk van het invallende deeltje zelf geabstraheerd. In het geval van OH radicalen echter, abstraheert het radicaal het H-atoom van de lipide-A structuur. De bekomen resulaten zijn in goede kwalitatieve overeenstemming met experimentele bevindingen. Daarom kunnen onze simulaties nuttig zijn om ons inzicht in de afbraakmechanismen van lipide-A door plasma's te verbeteren, en op die manier inzicht te verkrijgen in de antibacteriële eigenschappen van plasma's.

In het algemeen kunnen we uit bovenbeschreven studies met betrekking tot de interactie van plasma ROS met PG, lipide-A en een waterlaag concluderen dat deze plasmadeeltjes in staat zijn het oppervlak van bacteriën af te breken, en zo de deactivatie van deze organismen kunnen bewerkstelligen. De simulaties tonen aan dat alle interactiemechanismen geïnitieerd worden door H-abstractie reacties. Dit leidt op zijn beurt tot de dissociatie van structureel belangrijke bindingen in de moleculen en de afbraak van de behandelde organismen. De mechanismen en processen die onderliggend zijn aan deze afbraak zijn echter afhankelijk van de invallende plasmadeeltjes, en dit bepaalt dan ook de effectiviteit van de bindingsdissociaties en dus hun antibacterieel effect.

Deze computationele studies dragen bij aan een beter fundamenteel inzicht in de interactiemechanismen van bovenvernoemde structuren met plasmadeeltjes op atomaire schaal.

Tenslotte tonen de uitgevoerde studies ook aan dat dergelijke atomaire simulaties een waardevol inzicht bieden in de details van de microscopische processen die plaatsvinden in de plasmabehandeling van bacteriën. Dit is op zijn beurt belangrijk om inzicht te verkrijgen in de fundamenteel werkzame mechanismen in plasmageneeskunde.

Toekomstperspectief. In vervolgstudies zou de interactie van plasmadeeltjes met complexere en grotere structuren beoogd kunnen worden. Een voorbeeld van een dergelijke complexere structuur is de fosfolipide dubbellaag, die in bacteriën de laag onder PG (of LPS) is. Daarnaast bestaan de biofilms die bacteriën omgeven niet uit louter water, maar zijn zij relatief complex qua structuur en samenstelling. Naast water bestaat een biofilm uit een conglomeraat van verschillende biopolymeren dat de mal vormt voor de driedimensionele architectuur van de biofilm en verantwoordelijk is voor de adhesie aan oppervlakken en de cohesie in de biofilm zelf. Daarom is ook de studie van het opbreken van deze structuur door koude atmosferische plasma's van groot belang voor een verdere ontwikkeling van plasmageneeskunde.

Bibliography

[1]   A. Bogaerts, E. Neyts, R. Gijbels, and J. van der Mullen, "Gas discharge plasmas and their applications," *Spectrochimica Acta Part B: Atomic Spectroscopy,* vol. 57, pp. 609-658, 2002.

[2]   M. G. Kong, G. Kroesen, G. Morfill, T. Nosenko, T. Shimizu, J. van Dijk*, et al.*, "Plasma medicine: an introductory review," *New Journal of Physics,* vol. 11, p. 115012, 2009.

[3]   K. Ostrikov, E. C. Neyts, and M. Meyyappan, "Plasma nanoscience: from nano-solids in plasmas to nano-plasmas in solids," *Advances in Physics,* vol. 62, pp. 113-224, 2013.

[4]   M. Yousfi, N. Merbahi, A. Pathak, and O. Eichwald, "Low-temperature plasmas at atmospheric pressure: toward new pharmaceutical treatments in medicine," *Fundam Clin Pharmacol,* vol. 28, pp. 123-35, Apr 2014.

[5]   M. Laroussi, "Low Temperature Plasma-Based Sterilization: Overview and State-of-the-Art," *Plasma Processes and Polymers,* vol. 2, pp. 391-400, 2005.

[6]   Y.-F. Li, T. Shimizu, J. L. Zimmermann, and G. E. Morfill, "Cold Atmospheric Plasma for Surface Disinfection," *Plasma Processes and Polymers,* vol. 9, pp. 585-589, 2012.

[7]   M. Hee Lee, B. Joo Park, S. Chang Jin, D. Kim, I. Han, J. Kim*, et al.*, "Removal and sterilization of biofilms and planktonic bacteria by microwave-induced argon plasma at atmospheric pressure," *New Journal of Physics,* vol. 11, p. 115022, 2009.

[8]   H. W. Lee, G. J. Kim, J. M. Kim, J. K. Park, J. K. Lee, and G. C. Kim, "Tooth bleaching with nonthermal atmospheric pressure plasma," *J Endod,* vol. 35, pp. 587-91, Apr 2009.

[9]   A. B. Shekhter, V. A. Serezhenkov, T. G. Rudenko, A. V. Pekshev, and A. F. Vanin, "Beneficial effect of gaseous nitric oxide on the healing of skin wounds," *Nitric Oxide,* vol. 12, pp. 210-9, Jun 2005.

[10]   H. Min Joh, S. Ja Kim, T. H. Chung, and S. H. Leem, "Reactive oxygen species-related plasma effects on the apoptosis of human bladder cancer cells in atmospheric pressure pulsed plasma jets," *Applied Physics Letters,* vol. 101, p. 053703, 2012.

[11]   J. Huang, H. Li, W. Chen, G.-H. Lv, X.-Q. Wang, G.-P. Zhang*, et al.*, "Dielectric barrier discharge plasma in Ar/O2 promoting apoptosis behavior in A549 cancer cells," *Applied Physics Letters,* vol. 99, p. 253701, 2011.

[12]   N. Barekzi and M. Laroussi, "Dose-dependent killing of leukemia cells by low-temperature plasma," *Journal of Physics D: Applied Physics,* vol. 45, p. 422002, 2012.

[13] N. K. Kaushik, Y. H. Kim, Y. G. Han, and E. H. Choi, "Effect of jet plasma on T98G human brain cancer cells (vol 13, pg 176, 2012)," *Current Applied Physics,* vol. 13, pp. 614-618, 2013.

[14] S. Zhao, Z. Xiong, X. Mao, D. Meng, Q. Lei, Y. Li*, et al.*, "Atmospheric pressure room temperature plasma jets facilitate oxidative and nitrative stress and lead to endoplasmic reticulum stress dependent apoptosis in HepG2 cells," *PLoS One,* vol. 8, p. e73665, 2013.

[15] G. Fridman, G. Friedman, A. Gutsol, A. B. Shekhter, V. N. Vasilets, and A. Fridman, "Applied Plasma Medicine," *Plasma Processes and Polymers,* vol. 5, pp. 503-533, 2008.

[16] G. E. Morfill, M. G. Kong, and J. L. Zimmermann, "Focus on Plasma Medicine," *New Journal of Physics,* vol. 11, p. 115011, 2009.

[17] J. Ehlbeck, U. Schnabel, M. Polak, J. Winter, T. von Woedtke, R. Brandenburg*, et al.*, "Low temperature atmospheric pressure plasma sources for microbial decontamination," *Journal of Physics D: Applied Physics,* vol. 44, p. 013002, 2011.

[18] K. D. Weltmann, E. Kindel, T. von Woedtke, M. Hähnel, M. Stieber, and R. Brandenburg, "Atmospheric-pressure plasma sources: Prospective tools for plasma medicine," *Pure and Applied Chemistry,* vol. 82, 2010.

[19] K. D. Weltmann, M. Polak, K. Masur, T. von Woedtke, J. Winter, and S. Reuter, "Plasma Processes and Plasma Sources in Medicine," *Contributions to Plasma Physics,* vol. 52, pp. 644-654, 2012.

[20] G. Isbary, T. Shimizu, Y. Li, W. Stolz, H. Thomas, G. Morfill*, et al.*, "Cold atmospheric plasma devices for medical issues," *Expert review of medical devices,* vol. 10, pp. 367-377, 2013.

[21] T. von Woedtke, S. Reuter, K. Masur, and K. D. Weltmann, "Plasmas for medicine," *Physics Reports,* vol. 530, pp. 291-320, 2013.

[22] X. Lu, M. Laroussi, and V. Puech, "On atmospheric-pressure non-equilibrium plasma jets and plasma bullets," *Plasma Sources Science and Technology,* vol. 21, p. 034005, 2012.

[23] M. Laroussi and T. Akan, "Arc-Free Atmospheric Pressure Cold Plasma Jets: A Review," *Plasma Processes and Polymers,* vol. 4, pp. 777-788, 2007.

[24] U. Kogelschatz, "Dielectric-barrier discharges: their history, discharge physics, and industrial applications," *Plasma chemistry and plasma processing,* vol. 23, pp. 1-46, 2003.

[25] F. Iza, G. J. Kim, S. M. Lee, J. K. Lee, J. L. Walsh, Y. T. Zhang*, et al.*, "Microplasmas: Sources, Particle Kinetics, and Biomedical Applications," *Plasma Processes and Polymers,* vol. 5, pp. 322-344, 2008.

[26] M. Moreau, N. Orange, and M. G. Feuilloley, "Non-thermal plasma technologies: new tools for bio-decontamination," *Biotechnol Adv,* vol. 26, pp. 610-7, Nov-Dec 2008.

[27]   S. Lerouge, M. Wertheimer, and Y. L'H, "Plasma sterilization: a review of parameters, mechanisms, and limitations," *Plasmas and Polymers,* vol. 6, pp. 175-188, 2001.

[28]   M. Moisan, K. Boudam, D. Carignan, D. Kéroack, P. Levif, J. Barbeau*, et al.*, "Sterilization/disinfection of medical devices using plasma: the flowing afterglow of the reduced-pressure N2-O2discharge as the inactivating medium," *The European Physical Journal Applied Physics,* vol. 63, p. 10001, 2013.

[29]   M. Moisan, J. Barbeau, S. Moreau, J. Pelletier, M. Tabrizian, and L. H. Yahia, "Low-temperature sterilization using gas plasmas: a review of the experiments and an analysis of the inactivation mechanisms," *International journal of Pharmaceutics,* vol. 226, pp. 1-21, 2001.

[30]   P. Bruggeman and C. Leys, "Non-thermal plasmas in and in contact with liquids," *Journal of Physics D: Applied Physics,* vol. 42, p. 053001, 2009.

[31]   D. B. Graves, "The emerging role of reactive oxygen and nitrogen species in redox biology and some implications for plasma applications to medicine and biology," *Journal of Physics D: Applied Physics,* vol. 45, p. 263001, 2012.

[32]   J. Heinlin, G. Morfill, M. Landthaler, W. Stolz, G. Isbary, J. L. Zimmermann*, et al.*, "Plasma medicine: possible applications in dermatology," *JDDG: Journal der Deutschen Dermatologischen Gesellschaft,* vol. 8, pp. 968-976, 2010.

[33]   H. W. Lee, G. Y. Park, Y. S. Seo, Y. H. Im, S. B. Shim, and H. J. Lee, "Modelling of atmospheric pressure plasmas for biomedical applications," *Journal of Physics D: Applied Physics,* vol. 44, p. 053001, 2011.

[34]   E. C. Neyts, M. Yusupov, C. C. Verlackt, and A. Bogaerts, "Computer simulations of plasma-biomolecule and plasma-tissue interactions for a better insight in plasma medicine," *Journal of Physics D: Applied Physics,* 2014.

[35]   E. Stoffels, A. Flikweert, W. Stoffels, and G. Kroesen, "Plasma needle: a non-destructive atmospheric plasma source for fine surface treatment of (bio) materials," *Plasma Sources Science and Technology,* vol. 11, p. 383, 2002.

[36]   A. Schutze, J. Y. Jeong, S. E. Babayan, J. Park, G. S. Selwyn, and R. F. Hicks, "The atmospheric-pressure plasma jet: a review and comparison to other plasma sources," *Plasma Science, IEEE Transactions on,* vol. 26, pp. 1685-1694, 1998.

[37]   S. Reuter, K. Niemi, V. Schulz-von der Gathen, and H. F. Döbele, "Generation of atomic oxygen in the effluent of an atmospheric pressure plasma jet," *Plasma Sources Science and Technology,* vol. 18, p. 015006, 2009.

[38]   S. Rupf, A. Lehmann, M. Hannig, B. Schäfer, A. Schubert, U. Feldmann*, et al.*, "Killing of adherent oral microbes by a non-thermal atmospheric plasma jet," *Journal of medical microbiology,* vol. 59, pp. 206-212, 2010.

[39]   K. D. Weltmann, E. Kindel, R. Brandenburg, C. Meyer, R. Bussiahn, C. Wilke*, et al.*, "Atmospheric pressure plasma jet for medical therapy: plasma parameters and risk estimation," *Contributions to Plasma Physics,* vol. 49, pp. 631-640, 2009.

[40]   G. Fridman, M. Peddinghaus, M. Balasubramanian, H. Ayan, A. Fridman, A. Gutsol, *et al.*, "Blood coagulation and living tissue sterilization by floating-electrode dielectric barrier discharge in air," *Plasma Chemistry and Plasma Processing,* vol. 26, pp. 425-442, 2006.

[41]   S. Schneider, J. W. Lackmann, F. Narberhaus, J. E. Bandow, B. Denis, and J. Benedikt, "Separation of VUV/UV photons and reactive particles in the effluent of a He/O2atmospheric pressure plasma jet," *Journal of Physics D: Applied Physics,* vol. 44, p. 295201, 2011.

[42]   D. Ellerweg, J. Benedikt, A. von Keudell, N. Knake, and V. Schulz-von der Gathen, "Characterization of the effluent of a He/O2microscale atmospheric pressure plasma jet by quantitative molecular beam mass spectrometry," *New Journal of Physics,* vol. 12, p. 013021, 2010.

[43]   D. Ellerweg, A. von Keudell, and J. Benedikt, "Unexpected O and O3production in the effluent of He/O2microplasma jets emanating into ambient air," *Plasma Sources Science and Technology,* vol. 21, p. 034019, 2012.

[44]   J. K. Lee, M. S. Kim, J. H. Byun, K. T. Kim, G. C. Kim, and G. Y. Park, "Biomedical Applications of Low Temperature Atmospheric Pressure Plasmas to Cancerous Cell Treatment and Tooth Bleaching," *Japanese Journal of Applied Physics,* vol. 50, p. 08JF01, 2011.

[45]   M. Kuchenbecker, N. Bibinov, A. Kaemlimg, D. Wandke, P. Awakowicz, and W. Viöl, "Characterization of DBD plasma source for biomedical applications," *Journal of Physics D: Applied Physics,* vol. 42, p. 045212, 2009.

[46]   M. R. Wertheimer and S. Coulombe, "Plasma Medicine," *Physics in Canada,* vol. 68, p. 189, 2012.

[47]   A. Fridman, A. Chirokov, and A. Gutsol, "Non-thermal atmospheric pressure discharges," *Journal of Physics D: Applied Physics,* vol. 38, p. R1, 2005.

[48]   H.-E. Wagner, R. Brandenburg, K. Kozlov, A. Sonnenfeld, P. Michel, and J. Behnke, "The barrier discharge: basic properties and applications to surface treatment," *Vacuum,* vol. 71, pp. 417-436, 2003.

[49]   K. Fricke, H. Steffen, T. von Woedtke, K. Schröder, and K.-D. Weltmann, "High Rate Etching of Polymers by Means of an Atmospheric Pressure Plasma Jet," *Plasma Processes and Polymers,* vol. 8, pp. 51-58, 2011.

[50]   R. Wallenwein, "Low-temperature plasma sterilization with respect to patents," *Zentralsterilisation,* vol. 3, pp. 373-384, 1995.

[51]   I. Soloshenko, V. Tsiolko, V. Khomich, A. Shchedrin, A. Ryabtsev, V. Y. Bazhenov, *et al.*, "Sterilization of medical productsin low-pressure glow discharges," *Plasma physics reports,* vol. 26, pp. 792-800, 2000.

[52]   M. Moisan, J. Barbeau, M.-C. Crevier, J. Pelletier, N. Philip, and B. Saoudi, "Plasma sterilization. Methods and mechanisms," *Pure and applied chemistry,* vol. 74, pp. 349-358, 2002.

[53] J. Feichtinger, A. Schulz, M. Walker, and U. Schumacher, "Sterilisation with low-pressure microwave plasmas," *Surface and coatings technology,* vol. 174, pp. 564-569, 2003.

[54] F. Rossi, R. De Mitri, S. Bobin, and R. Eloy, "Plasma sterilisation: Mechanisms overview and influence of discharge parameters," *Plasma Processes and Polymers,* pp. 319-331, 2005.

[55] O. Kylián, M. Hasiwa, and F. Rossi, "Plasma-Based De-Pyrogenization," *Plasma Processes and Polymers,* vol. 3, pp. 272-275, 2006.

[56] F. Rossi, O. Kylian, H. Rauscher, M. Hasiwa, and D. Gilliland, "Low pressure plasma discharges for the sterilization and decontamination of surfaces," *New Journal of Physics,* vol. 11, p. 115017, 2009.

[57] J. Schneider, K. Baumgärtner, J. Feichtinger, J. Krüger, P. Muranyi, A. Schulz*, et al.*, "Investigation of the practicability of low-pressure microwave plasmas in the sterilisation of food packaging materials at industrial level," *Surface and coatings technology,* vol. 200, pp. 962-966, 2005.

[58] H. Baxter, G. Campbell, A. Whittaker, A. Jones, A. Aitken, A. Simpson*, et al.*, "Elimination of transmissible spongiform encephalopathy infectivity and decontamination of surgical instruments by using radio-frequency gas-plasma treatment," *Journal of general virology,* vol. 86, pp. 2393-2399, 2005.

[59] K. Banerjee, S. Kumar, K. Bremmell, and H. Griesser, "Molecular-level removal of proteinaceous contamination from model surfaces and biomedical device materials by air plasma treatment," *Journal of Hospital Infection,* vol. 76, pp. 234-242, 2010.

[60] A. Whittaker, E. Graham, R. Baxter, A. Jones, P. Richardson, G. Meek*, et al.*, "Plasma cleaning of dental instruments," *Journal of Hospital Infection,* vol. 56, pp. 37-41, 2004.

[61] A. von Keudell, P. Awakowicz, J. Benedikt, V. Raballand, A. Yanguas-Gil, J. Opretzka*, et al.*, "Inactivation of Bacteria and Biomolecules by Low-Pressure Plasma Discharges," *Plasma Processes and Polymers,* vol. 7, pp. 327-352, 2010.

[62] N. Bai, P. Sun, H. Zhou, H. Wu, R. Wang, F. Liu*, et al.*, "Inactivation of Staphylococcus aureus in Water by a Cold, He/O2 Atmospheric Pressure Plasma Microjet," *Plasma Processes and Polymers,* vol. 8, pp. 424-431, 2011.

[63] K. Oehmigen, M. Hähnel, R. Brandenburg, C. Wilke, K. D. Weltmann, and T. von Woedtke, "The Role of Acidification for Antimicrobial Activity of Atmospheric Pressure Plasma in Liquids," *Plasma Processes and Polymers,* vol. 7, pp. 250-257, 2010.

[64] M. Hähnel, T. von Woedtke, and K.-D. Weltmann, "Influence of the Air Humidity on the Reduction ofBacillusSpores in a Defined Environment at Atmospheric Pressure Using a Dielectric Barrier Surface Discharge," *Plasma Processes and Polymers,* vol. 7, pp. 244-249, 2010.

[65] M. Hähnel, A. Diener, Ü. Kolukisaoglu, K. D. Weltmann, and K. Thurow, "The Influence on Cell Growth Properties in Different Microtiterplate Types by Corona-Dielectric Barrier Discharge Plasma at Atmospheric Pressure," *Plasma Processes and Polymers,* vol. 8, pp. 70-76, 2011.

[66] B. A. Niemira, "Cold plasma decontamination of foods," *Annu Rev Food Sci Technol,* vol. 3, pp. 125-42, 2012.

[67] J. E. Kim, D. U. Lee, and S. C. Min, "Microbial decontamination of red pepper powder by cold plasma," *Food Microbiol,* vol. 38, pp. 128-36, Apr 2014.

[68] S. Deng, R. Ruan, C. K. Mok, G. Huang, X. Lin, and P. Chen, "Inactivation of Escherichia coli on almonds using nonthermal plasma," *J Food Sci,* vol. 72, pp. M62-6, Mar 2007.

[69] F. Leipold, Y. Kusano, F. Hansen, and T. Jacobsen, "Decontamination of a rotating cutting tool during operation by means of atmospheric pressure plasmas," *Food control,* vol. 21, pp. 1194-1198, 2010.

[70] S. Perni, G. Shama, and M. G. Kong, "Cold atmospheric plasma disinfection of cut fruit surfaces contaminated with migrating microorganisms," *Journal of Food Protection®,* vol. 71, pp. 1619-1625, 2008.

[71] J. Wan, J. Coventry, P. Swiergon, P. Sanguansri, and C. Versteeg, "Advances in innovative processing technologies for microbial inactivation and enhancement of food safety–pulsed electric field and low-temperature plasma," *Trends in food science & technology,* vol. 20, pp. 414-424, 2009.

[72] S. U. Kalghatgi, G. Fridman, M. Cooper, G. Nagaraj, M. Peddinghaus, M. Balasubramanian*, et al.*, "Mechanism of blood coagulation by nonthermal atmospheric pressure dielectric barrier discharge plasma," *Plasma Science, IEEE Transactions on,* vol. 35, pp. 1559-1566, 2007.

[73] J. Choi, A. A. H. Mohamed, S. K. Kang, K. C. Woo, K. T. Kim, and J. K. Lee, "900-MHz Nonthermal Atmospheric Pressure Plasma Jet for Biomedical Applications," *Plasma Processes and Polymers,* vol. 7, pp. 258-263, 2010.

[74] S. Kuo, O. Tarasenko, J. Chang, S. Popovic, C. Chen, H. Fan*, et al.*, "Contribution of a portable air plasma torch to rapid blood coagulation as a method of preventing bleeding," *New Journal of Physics,* vol. 11, p. 115016, 2009.

[75] S. P. Kuo, C.-Y. Chen, C.-S. Lin, and S.-H. Chiang, "Wound bleeding control by low temperature air plasma," *Plasma Science, IEEE Transactions on,* vol. 38, pp. 1908-1914, 2010.

[76] G. Fridman, A. D. Brooks, M. Balasubramanian, A. Fridman, A. Gutsol, V. N. Vasilets*, et al.*, "Comparison of Direct and Indirect Effects of Non-Thermal Atmospheric-Pressure Plasma on Bacteria," *Plasma Processes and Polymers,* vol. 4, pp. 370-375, 2007.

[77] S. Kalghatgi, D. Dobrynin, G. Fridman, M. Cooper, G. Nagaraj, L. Peddinghaus*, et al.*, "Applications of non thermal atmospheric pressure plasma in medicine," in

Plasma Assisted Decontamination of Biological and Chemical Agents, ed: Springer, 2008, pp. 173-181.

[78]   M. Vandamme, E. Robert, S. Dozias, J. Sobilo, S. Lerondel, A. Le Pape*, et al.*, "Response of human glioma U87 xenografted on mice to non thermal plasma treatment," *Plasma medicine,* vol. 1, 2011.

[79]   M. Vandamme, E. Robert, S. Pesnel, E. Barbosa, S. Dozias, J. Sobilo*, et al.*, "Antitumor Effect of Plasma Treatment on U87 Glioma Xenografts: Preliminary Results," *Plasma Processes and Polymers,* vol. 7, pp. 264-273, 2010.

[80]   K. Ninomiya, T. Ishijima, M. Imamura, T. Yamahara, H. Enomoto, K. Takahashi*, et al.*, "Evaluation of extra- and intracellular OH radical generation, cancer cell injury, and apoptosis induced by a non-thermal atmospheric-pressure plasma jet," *Journal of Physics D: Applied Physics,* vol. 46, p. 425401, 2013.

[81]   E. Robert, M. Vandamme, J. Sobilo, V. Sarron, D. Ries, S. Dozias*, et al.*, "First Achievements and Opportunities for Cancer Treatment Using Non-thermal Plasma," in *Plasma for Bio-Decontamination, Medicine and Food Security*, Z. Machala, K. Hensel, and Y. Akishev, Eds., ed: Springer Netherlands, 2012, pp. 381-392.

[82]   E. Robert, E. Barbosa, S. Dozias, M. Vandamme, C. Cachoncinlle, R. Viladrosa*, et al.*, "Experimental study of a compact nanosecond plasma gun," *Plasma processes and polymers,* vol. 6, pp. 795-802, 2009.

[83]   S. Emmert, F. Brehmer, H. Hänßle, A. Helmke, N. Mertens, R. Ahmed*, et al.*, "Atmospheric pressure plasma in dermatology: Ulcus treatment and much more," *Clinical Plasma Medicine,* vol. 1, pp. 24-29, 2013.

[84]   A. Kramer, J. Lademann, C. Bender, A. Sckell, B. Hartmann, S. Münch*, et al.*, "Suitability of tissue tolerable plasmas (TTP) for the management of chronic wounds," *Clinical Plasma Medicine,* vol. 1, pp. 11-18, 2013.

[85]   G. Lloyd, G. Friedman, S. Jafri, G. Schultz, A. Fridman, and K. Harding, "Gas Plasma: Medical Uses and Developments in Wound Care," *Plasma Processes and Polymers,* vol. 7, pp. 194-211, 2010.

[86]   G. Isbary, G. Morfill, H. U. Schmidt, M. Georgi, K. Ramrath, J. Heinlin*, et al.*, "A first prospective randomized controlled trial to decrease bacterial load using cold atmospheric argon plasma on chronic wounds in patients," *Br J Dermatol,* vol. 163, pp. 78-82, Jul 2010.

[87]   G. Isbary, J. Heinlin, T. Shimizu, J. Zimmermann, G. Morfill, H. U. Schmidt*, et al.*, "Successful and safe use of 2 min cold atmospheric argon plasma in chronic wounds: results of a randomized controlled trial," *British Journal of Dermatology,* vol. 167, pp. 404-410, 2012.

[88]   G. Isbary, J. Köritzer, A. Mitra, Y. F. Li, T. Shimizu, J. Schroeder*, et al.*, "Ex vivo human skin experiments for the evaluation of safety of new cold atmospheric plasma devices," *Clinical Plasma Medicine,* vol. 1, pp. 36-44, 2013.

[89] G. Isbary, J. L. Zimmermann, T. Shimizu, Y. F. Li, G. E. Morfill, H. M. Thomas, *et al.*, "Non-thermal plasma—More than five years of clinical experience," *Clinical Plasma Medicine,* vol. 1, pp. 19-23, 2013.

[90] H.-R. Metelmann, T. T. Vu, H. T. Do, T. N. B. Le, T. H. A. Hoang, T. T. T. Phi, *et al.*, "Scar formation of laser skin lesions after cold atmospheric pressure plasma (CAP) treatment: A clinical long term observation," *Clinical Plasma Medicine,* vol. 1, pp. 30-35, 2013.

[91] A. S. Wu, S. Kalghatgi, D. Dobrynin, R. Sensenig, E. Cerchar, E. Podolsky, *et al.*, "Porcine intact and wounded skin responses to atmospheric nonthermal plasma," *Journal of Surgical Research,* vol. 179, pp. e1-e12, 2013.

[92] H. W. Lee, S. H. Nam, A.-A. H. Mohamed, G. C. Kim, and J. K. Lee, "Atmospheric Pressure Plasma Jet Composed of Three Electrodes: Application to Tooth Bleaching," *Plasma Processes and Polymers,* vol. 7, pp. 274-280, 2010.

[93] J. Park, *The murein sacculus* vol. 1, 1996.

[94] D. Mengin-Lecreulx and B. Lemaitre, "Structure and metabolism of peptidoglycan and molecular requirements allowing its detection by the Drosophila innate immune system," *Journal of endotoxin research,* vol. 11, pp. 105-111, 2005.

[95] W. Vollmer, D. Blanot, and M. A. de Pedro, "Peptidoglycan structure and architecture," *FEMS Microbiol Rev,* vol. 32, pp. 149-167, Mar 2008.

[96] W. Vollmer and S. J. Seligman, "Architecture of peptidoglycan: more data and more models," *Trends Microbiol,* vol. 18, pp. 59-66, Feb 2010.

[97] B. A. Dmitriev, F. V. Toukach, O. Holst, E. T. Rietschel, and S. Ehlers, "Tertiary structure of Staphylococcus aureus cell wall murein," *J Bacteriol,* vol. 186, pp. 7141-7148, Nov 2004.

[98] P. Giesbrecht, T. Kersten, H. Maidhof, and J. Wecke, "Staphylococcal cell wall: morphogenesis and fatal variations in the presence of penicillin," *Microbiology and molecular biology reviews,* vol. 62, pp. 1371-1414, 1998.

[99] J. Cohen, "The immunopathogenesis of sepsis," *Nature,* vol. 420, pp. 885-891, 2002.

[100] C. Erridge, E. Bennett-Guerrero, and I. R. Poxton, "Structure and function of lipopolysaccharides," *Microbes and Infection,* vol. 4, pp. 837-851, 2002.

[101] D. Dobrynin, G. Fridman, G. Friedman, and A. Fridman, "Physical and biological mechanisms of direct plasma interaction with living tissue," *New Journal of Physics,* vol. 11, p. 115020, 2009.

[102] I. c. o. n.-i. r. protection, "Guidelines on limits of exposure to ultraviolet radiation of wavelengths between 180 nm and 400 nm (incoherent optical radiation)," *Health Physics,* vol. 87, pp. 171-186, 2004.

[103] Q. Zhang, P. Sun, H. Feng, R. Wang, Y. Liang, W. Zhu, *et al.*, "Assessment of the roles of various inactivation agents in an argon-based direct current atmospheric pressure cold plasma jet," *Journal of Applied Physics,* vol. 111, p. 123305, 2012.

[104] X. Deng, J. Shi, and M. G. Kong, "Physical mechanisms of inactivation of Bacillus subtilis spores using cold atmospheric plasmas," *Plasma Science, IEEE Transactions on,* vol. 34, pp. 1310-1316, 2006.

[105] S. J. Kim, T. H. Chung, S. H. Bae, and S. H. Leem, "Bacterial inactivation using atmospheric pressure single pin electrode microplasma jet with a ground ring," *Applied Physics Letters,* vol. 94, p. 141502, 2009.

[106] X. Lu, T. Ye, Y. Cao, Z. Sun, Q. Xiong, Z. Tang*, et al.*, "The roles of the various plasma agents in the inactivation of bacteria," *Journal of Applied Physics,* vol. 104, p. 053309, 2008.

[107] H. J. Ahn, K. I. Kim, G. Kim, E. Moon, S. S. Yang, and J.-S. Lee, "Atmospheric-pressure plasma jet induces apoptosis involving mitochondria via generation of free radicals," *PLoS One,* vol. 6, p. e28154, 2011.

[108] R. Sensenig, S. Kalghatgi, E. Cerchar, G. Fridman, A. Shereshevsky, B. Torabi*, et al.*, "RETRACTED ARTICLE: Non-thermal Plasma Induces Apoptosis in Melanoma Cells via Production of Intracellular Reactive Oxygen Species," *Annals of biomedical engineering,* vol. 39, pp. 674-687, 2011.

[109] M. Vandamme, E. Robert, S. Lerondel, V. Sarron, D. Ries, S. Dozias*, et al.*, "ROS implication in a new antitumor strategy based on non-thermal plasma," *International Journal of Cancer,* vol. 130, pp. 2185-2194, 2012.

[110] J. Liebmann, J. Scherer, N. Bibinov, P. Rajasekaran, R. Kovacs, R. Gesche*, et al.*, "Biological effects of nitric oxide generated by an atmospheric pressure gas-plasma on human skin cells," *Nitric Oxide,* vol. 24, pp. 8-16, 2011.

[111] X. Yan, F. Zou, X. P. Lu, G. He, M. J. Shi, Q. Xiong*, et al.*, "Effect of the atmospheric pressure nonequilibrium plasmas on the conformational changes of plasmid DNA," *Applied Physics Letters,* vol. 95, p. 083702, 2009.

[112] D. O'Connell, L. J. Cox, W. B. Hyland, S. J. McMahon, S. Reuter, W. G. Graham*, et al.*, "Cold atmospheric pressure plasma jet interactions with plasmid DNA," *Applied Physics Letters,* vol. 98, p. 043701, 2011.

[113] H. Yasuda, T. Miura, H. Kurita, K. Takashima, and A. Mizuno, "Biological evaluation of DNA damage in bacteriophages inactivated by atmospheric pressure cold plasma," *Plasma Processes and Polymers,* vol. 7, pp. 301-308, 2010.

[114] M. Leduc, D. Guay, S. Coulombe, and R. L. Leask, "Effects of Non-thermal Plasmas on DNA and Mammalian Cells," *Plasma Processes and Polymers,* vol. 7, pp. 899-909, 2010.

[115] S. Kalghatgi, C. M. Kelly, E. Cerchar, B. Torabi, O. Alekseev, A. Fridman*, et al.*, "Effects of non-thermal plasma on mammalian cells," *PloS one,* vol. 6, p. e16270, 2011.

[116] Z. Xiong, T. Du, X. Lu, Y. Cao, and Y. Pan, "How deep can plasma penetrate into a biofilm?," *Applied Physics Letters,* vol. 98, p. 221503, 2011.

[117] Y. Sakiyama, D. B. Graves, H.-W. Chang, T. Shimizu, and G. E. Morfill, "Plasma chemistry model of surface microdischarge in humid air and dynamics of reactive neutral species," *Journal of Physics D: Applied Physics,* vol. 45, p. 425201, 2012.

[118] J. W. Lackmann, S. Schneider, E. Edengeiser, F. Jarzina, S. Brinckmann, E. Steinborn*, et al.*, "Photons and particles emitted from cold atmospheric-pressure plasma inactivate bacteria and biomolecules independently and synergistically," *J R Soc Interface,* vol. 10, p. 20130591, Dec 6 2013.

[119] E. A. J. Bartis, C. Barrett, T. Y. Chung, N. Ning, J. W. Chu, D. B. Graves*, et al.*, "Deactivation of lipopolysaccharide by Ar and H2inductively coupled low-pressure plasma," *Journal of Physics D: Applied Physics,* vol. 47, p. 045202, 2014.

[120] T.-Y. Chung, N. Ning, J.-W. Chu, D. B. Graves, E. Bartis, S. Joonil*, et al.*, "Plasma Deactivation of Endotoxic Biomolecules: Vacuum Ultraviolet Photon and Radical Beam Effects on Lipid A," *Plasma Processes and Polymers,* vol. 10, pp. 167-180, 2013.

[121] E. A. J. Bartis, D. B. Graves, J. Seog, and G. S. Oehrlein, "Atmospheric pressure plasma treatment of lipopolysaccharide in a controlled environment," *Journal of Physics D: Applied Physics,* vol. 46, p. 312002, 2013.

[122] N. Y. Babaeva, N. Ning, D. B. Graves, and M. J. Kushner, "Ion activation energy delivered to wounds by atmospheric pressure dielectric-barrier discharges: sputtering of lipid-like surfaces," *Journal of Physics D: Applied Physics,* vol. 45, p. 115203, 2012.

[123] R. M. Cordeiro, "Reactive oxygen species at phospholipid bilayers: distribution, mobility and permeation," *Biochim Biophys Acta,* vol. 1838, pp. 438-444, Jan 2014.

[124] R. M. Abolfath, A. C. van Duin, and T. Brabec, "Reactive molecular dynamics study on the first steps of DNA damage by free hydroxyl radicals," *J Phys Chem A,* vol. 115, pp. 11045-11049, Oct 13 2011.

[125] J. Van der Paal, S. Aernouts, A. C. T. van Duin, E. C. Neyts, and A. Bogaerts, "Interaction of O and OH radicals with a simple model system for lipids in the skin barrier: a reactive molecular dynamics investigation for plasma medicine," *Journal of Physics D: Applied Physics,* vol. 46, p. 395201, 2013.

[126] H. C. Flemming and J. Wingender, "The biofilm matrix," *Nat Rev Microbiol,* vol. 8, pp. 623-633, Sep 2010.

[127] C. A. J. van Gils, S. Hofmann, B. K. H. L. Boekema, R. Brandenburg, and P. J. Bruggeman, "Mechanisms of bacterial inactivation in the liquid phase induced by a remote RF cold atmospheric pressure plasma jet," *Journal of Physics D: Applied Physics,* vol. 46, p. 175203, 2013.

[128] S. Ikawa, K. Kitano, and S. Hamaguchi, "Effects of pH on Bacterial Inactivation in Aqueous Solutions due to Low-Temperature Atmospheric Pressure Plasma Application," *Plasma Processes and Polymers,* vol. 7, pp. 33-42, 2010.

[129] A. Tani, Y. Ono, S. Fukui, S. Ikawa, and K. Kitano, "Free radicals induced in aqueous solution by non-contact atmospheric-pressure cold plasma," *Applied Physics Letters,* vol. 100, p. 254103, 2012.

[130] B. Alder and T. Wainwright, "Phase transition for a hard sphere system," *The Journal of Chemical Physics,* vol. 27, p. 1208, 1957.

[131] D. Frenkel and B. Smit, *Understanding molecular simulation: from algorithms to applications* vol. 1: Academic press, 2001.

[132] R. Car and M. Parrinello, "Unified approach for molecular dynamics and density-functional theory," *Physical review letters,* vol. 55, p. 2471, 1985.

[133] E. Schrödinger, "Quantisierung als Eigenwertproblem," *Annalen der Physik,* vol. 384, pp. 361-376, 1926.

[134] M. Born and R. Oppenheimer, "Zur quantentheorie der molekeln," *Annalen der Physik,* vol. 389, pp. 457-484, 1927.

[135] J.-P. Hansen and I. R. McDonald, *Theory of simple liquids*: Elsevier, 1990.

[136] L. De Broglie, "Recherches sur la théorie des quanta," Migration-université en cours d'affectation, 1924.

[137] D. C. Rapaport, *The art of molecular dynamics simulation*: Cambridge university press, 2004.

[138] L. Verlet, "Computer" experiments" on classical fluids. I. Thermodynamical properties of Lennard-Jones molecules," *Physical review,* vol. 159, p. 98, 1967.

[139] M. P. Allen and D. J. Tildesley, *Computer simulation of liquids*: Oxford university press, 1989.

[140] U. Khalilov, "New perspectives on thermal and hyperthermal oxidation of Si surfaces," UNIVERSITEIT ANTWERPEN (BELGIUM), 2013.

[141] W. C. Swope, H. C. Andersen, P. H. Berens, and K. R. Wilson, "A computer simulation method for the calculation of equilibrium constants for the formation of physical clusters of molecules: Application to small water clusters," *The Journal of Chemical Physics,* vol. 76, pp. 637-649, 1982.

[142] J. J. Erpenbeck and W. W. Wood, "Molecular dynamics techniques for hard-core systems," *Statistical mechanics B: Modern theoretical chemistry,* vol. 6, pp. 1-40, 1977.

[143] D. Frenkel, "Introduction to monte carlo methods," *Computational Soft Matter: From Synthetic Polymers to Proteins,* vol. 23, pp. 29-59, 2004.

[144] H. J. Berendsen, J. P. M. Postma, W. F. van Gunsteren, A. DiNola, and J. Haak, "Molecular dynamics with coupling to an external bath," *The Journal of chemical physics,* vol. 81, pp. 3684-3690, 1984.

[145] G. Bussi, D. Donadio, and M. Parrinello, "Canonical sampling through velocity rescaling," *The Journal of chemical physics,* vol. 126, p. 014101, 2007.

[146] H. C. Andersen, "Molecular dynamics simulations at constant pressure and/or temperature," *The Journal of Chemical Physics,* vol. 72, pp. 2384-2393, 1980.

[147] S. Nosé, "A unified formulation of the constant temperature molecular dynamics methods," *The Journal of Chemical Physics,* vol. 81, pp. 511-519, 1984.

[148] W. G. Hoover, "Canonical dynamics: equilibrium phase-space distributions," *Physical Review A,* vol. 31, p. 1695, 1985.

[149] P. H. Hünenberger, "Thermostat algorithms for molecular dynamics simulations," in *Advanced Computer Simulation*, ed: Springer, 2005, pp. 105-149.

[150] W. Somers, A. Bogaerts, A. Van Duin, S. Huygh, K. Bal, and E. Neyts, "Temperature influence on the reactivity of plasma species on a nickel catalyst surface: An atomic scale study," *Catalysis Today,* vol. 211, pp. 131-136, 2013.

[151] Y. Duan and P. A. Kollman, "Pathways to a protein folding intermediate observed in a 1-microsecond simulation in aqueous solution," *Science,* vol. 282, pp. 740-744, 1998.

[152] A. Kuronen, "Introduction to Atomistic Simulations," *Lecture Notes, University of Helsinki,* 2006.

[153] H. Fehske, R. Schneider, and A. Weiße, *Computational many-particle physics* vol. 739: Springer, 2008.

[154] D. A. Case, T. E. Cheatham, T. Darden, H. Gohlke, R. Luo, K. M. Merz*, et al.*, "The Amber biomolecular simulation programs," *Journal of computational chemistry,* vol. 26, pp. 1668-1688, 2005.

[155] R. Salomon-Ferrer, D. A. Case, and R. C. Walker, "An overview of the Amber biomolecular simulation package," *Wiley Interdisciplinary Reviews: Computational Molecular Science,* vol. 3, pp. 198-210, 2013.

[156] A. C. Van Duin, S. Dasgupta, F. Lorant, and W. A. Goddard, "ReaxFF: a reactive force field for hydrocarbons," *The Journal of Physical Chemistry A,* vol. 105, pp. 9396-9409, 2001.

[157] D. W. Brenner, "Empirical potential for hydrocarbons for use in simulating the chemical vapor deposition of diamond films," *Physical Review B,* vol. 42, p. 9458, 1990.

[158] D. P. Tieleman, H. Leontiadou, A. E. Mark, and S.-J. Marrink, "Simulation of pore formation in lipid bilayers by mechanical stress and electric fields," *Journal of the American Chemical Society,* vol. 125, pp. 6382-6383, 2003.

[159] A. A. Gurtovenko and I. Vattulainen, "Pore formation coupled to ion transport through lipid membranes as induced by transmembrane ionic charge imbalance: atomistic molecular dynamics study," *Journal of the American Chemical Society,* vol. 127, pp. 17570-17571, 2005.

[160] M. Orsi, D. Y. Haubertin, W. E. Sanderson, and J. W. Essex, "A quantitative coarse-grain model for lipid bilayers," *The Journal of Physical Chemistry B,* vol. 112, pp. 802-815, 2008.

[161] W. L. Jorgensen and J. Tirado-Rives, "The OPLS [optimized potentials for liquid simulations] potential functions for proteins, energy minimizations for crystals of cyclic peptides and crambin," *Journal of the American Chemical Society,* vol. 110, pp. 1657-1666, 1988.

[162] W. L. Jorgensen, D. S. Maxwell, and J. Tirado-Rives, "Development and testing of the OPLS all-atom force field on conformational energetics and properties of organic liquids," *Journal of the American Chemical Society,* vol. 118, pp. 11225-11236, 1996.

[163] W. Van Gunsteren and H. Berendsen, "Gromos-87 Manual; Biomos BV: Nijenborgh 4, 9747 AG Groningen, The Netherlands," 1987.

[164] O. Berger, O. Edholm, and F. Jähnig, "Molecular dynamics simulations of a fluid bilayer of dipalmitoylphosphatidylcholine at full hydration, constant pressure, and constant temperature," *Biophysical journal,* vol. 72, pp. 2002-2013, 1997.

[165] B. R. Brooks, C. L. Brooks, 3rd, A. D. Mackerell, Jr., L. Nilsson, R. J. Petrella, B. Roux*, et al.*, "CHARMM: the biomolecular simulation program," *J Comput Chem,* vol. 30, pp. 1545-614, Jul 30 2009.

[166] M. P. Allen, "Introduction to molecular dynamics simulation," *Computational Soft Matter: From Synthetic Polymers to Proteins,* vol. 23, pp. 1-28, 2004.

[167] Available: http://www.ks.uiuc.edu/Research/namd/

[168] J. C. Phillips, R. Braun, W. Wang, J. Gumbart, E. Tajkhorshid, E. Villa*, et al.*, "Scalable molecular dynamics with NAMD," *Journal of computational chemistry,* vol. 26, pp. 1781-1802, 2005.

[169] D. van der Spoel, E. Lindahl, B. Hess, A. Van Buuren, E. Apol, P. Meulenhoff*, et al.*, "GROMACS user manual version 3.3," 2008.

[170] S. Pronk, S. Páll, R. Schulz, P. Larsson, P. Bjelkmar, R. Apostolov*, et al.*, "GROMACS 4.5: a high-throughput and highly parallel open source molecular simulation toolkit," *Bioinformatics,* vol. 29, pp. 845-854, 2013.

[171] M. S. Daw, S. M. Foiles, and M. I. Baskes, "The embedded-atom method: a review of theory and applications," *Materials Science Reports,* vol. 9, pp. 251-310, 1993.

[172] M. Baskes, J. Nelson, and A. Wright, "Semiempirical modified embedded-atom potentials for silicon and germanium," *Physical review B,* vol. 40, p. 6085, 1989.

[173] M. Finnis and J. Sinclair, "A simple empirical N-body potential for transition metals," *Philosophical Magazine A,* vol. 50, pp. 45-55, 1984.

[174] T.-R. Shan, B. D. Devine, T. W. Kemper, S. B. Sinnott, and S. R. Phillpot, "Charge-optimized many-body potential for the hafnium/hafnium oxide system," *Physical Review B,* vol. 81, p. 125328, 2010.

[175] P. Vashishta, R. K. Kalia, A. Nakano, and J. P. Rino, "Interaction potential for silicon carbide: a molecular dynamics study of elastic constants and vibrational density of states for crystalline and amorphous silicon carbide," *Journal of applied physics,* vol. 101, p. 103515, 2007.

[176] J. Tersoff, "New empirical approach for the structure and energy of covalent systems," *Physical Review B,* vol. 37, p. 6991, 1988.

[177] D. W. Brenner, O. A. Shenderova, J. A. Harrison, S. J. Stuart, B. Ni, and S. B. Sinnott, "A second-generation reactive empirical bond order (REBO) potential energy expression for hydrocarbons," *Journal of Physics: Condensed Matter,* vol. 14, p. 783, 2002.

[178] B. Ni, K.-H. Lee, and S. B. Sinnott, "A reactive empirical bond order (REBO) potential for hydrocarbon–oxygen interactions," *Journal of Physics: Condensed Matter,* vol. 16, p. 7261, 2004.

[179] K. Chenoweth, A. C. van Duin, and W. A. Goddard, "ReaxFF reactive force field for molecular dynamics simulations of hydrocarbon oxidation," *The Journal of Physical Chemistry A,* vol. 112, pp. 1040-1053, 2008.

[180] E. C. Neyts, Y. Shibuta, A. C. van Duin, and A. Bogaerts, "Catalyzed Growth of Carbon Nanotube with Definable Chirality by Hybrid Molecular Dynamics− Force Biased Monte Carlo Simulations," *ACS nano,* vol. 4, pp. 6665-6672, 2010.

[181] E. C. Neyts, A. C. van Duin, and A. Bogaerts, "Changing chirality during single-walled carbon nanotube growth: a reactive molecular dynamics/Monte Carlo study," *J Am Chem Soc,* vol. 133, pp. 17225-17231, Nov 2 2011.

[182] P. Valentini, T. E. Schwartzentruber, and I. Cozmuta, "Molecular dynamics simulation of O2 sticking on Pt (111) using the ab initio based ReaxFF reactive force field," *The Journal of chemical physics,* vol. 133, p. 084703, 2010.

[183] J. E. Mueller, A. C. van Duin, and W. A. Goddard III, "Application of the ReaxFF Reactive Force Field to Reactive Dynamics of Hydrocarbon Chemisorption and Decomposition†," *The Journal of Physical Chemistry C,* vol. 114, pp. 5675-5685, 2010.

[184] J. C. Fogarty, H. M. Aktulga, A. Y. Grama, A. C. van Duin, and S. A. Pandit, "A reactive molecular dynamics simulation of the silica-water interface," *J Chem Phys,* vol. 132, p. 174704, May 7 2010.

[185] U. Khalilov, E. C. Neyts, G. Pourtois, and A. C. T. van Duin, "Can We Control the Thickness of Ultrathin Silica Layers by Hyperthermal Silicon Oxidation at Room Temperature?," *The Journal of Physical Chemistry C,* vol. 115, pp. 24839-24848, 2011.

[186] U. Khalilov, G. Pourtois, A. Bogaerts, A. C. van Duin, and E. C. Neyts, "Reactive molecular dynamics simulations on SiO2-coated ultra-small Si-nanowires," *Nanoscale,* vol. 5, pp. 719-25, Jan 21 2013.

[187] U. Khalilov, G. Pourtois, A. v. Duin, and E. Neyts, "Self-limiting oxidation in small-diameter Si nanowires," *Chemistry of materials,* vol. 24, pp. 2141-2147, 2012.

[188] E. C. Neyts, U. Khalilov, G. Pourtois, and A. C. T. van Duin, "Hyperthermal Oxygen Interacting with Silicon Surfaces: Adsorption, Implantation, and Damage Creation," *The Journal of Physical Chemistry C,* vol. 115, pp. 4818-4823, 2011.

[189] O. Rahaman, A. C. van Duin, W. A. Goddard III, and D. J. Doren, "Development of a ReaxFF reactive force field for glycine and application to solvent effect and tautomerization," *The Journal of Physical Chemistry B,* vol. 115, pp. 249-261, 2010.

[190] S. Monti, A. Corozzi, P. Fristrup, K. L. Joshi, Y. K. Shin, P. Oelschlaeger*, et al.*, "Exploring the conformational and reactive dynamics of biomolecules in solution using an extended version of the glycine reactive force field," *Phys Chem Chem Phys,* vol. 15, pp. 15062-77, Sep 28 2013.

[191] S. Monti, A. C. T. van Duin, S.-Y. Kim, and V. Barone, "Exploration of the Conformational and Reactive Dynamics of Glycine and Diglycine on TiO2: Computational Investigations in the Gas Phase and in Solution," *The Journal of Physical Chemistry C,* vol. 116, pp. 5141-5150, 2012.

[192] M. J. Buehler, "Large-scale hierarchical molecular modeling of nanostructured biological materials," *Journal of Computational and Theoretical Nanoscience,* vol. 3, pp. 603-623, 2006.

[193] B. Narayanan, A. C. T. van Duin, B. B. Kappes, I. E. Reimanis, and C. V. Ciobanu, "A reactive force field for lithium–aluminum silicates with applications to eucryptite phases," *Modelling and Simulation in Materials Science and Engineering,* vol. 20, p. 015002, 2012.

[194] E. Stoffels, Y. Sakiyama, and D. B. Graves, "Cold atmospheric plasma: charged species and their interactions with cells and tissues," *Plasma Science, IEEE Transactions on,* vol. 36, pp. 1441-1457, 2008.

[195] E. de Vos Burchart, "Studies on zeolites: molecular mechanics, framework stability, and crystal growth," Delft University of Technology, Delft, The Netherlands, 1992.

[196] G. O. Janssens, B. G. Baekelandt, H. Toufar, W. J. Mortier, and R. A. Schoonheydt, "Comparison of cluster and infinite crystal calculations on zeolites with the electronegativity equalization method (EEM)," *The Journal of Physical Chemistry,* vol. 99, pp. 3251-3258, 1995.

[197] W. J. Mortier, S. K. Ghosh, and S. Shankar, "Electronegativity-equalization method for the calculation of atomic charges in molecules," *Journal of the American Chemical Society,* vol. 108, pp. 4315-4320, 1986.

[198] H. M. Aktulga, "PuReMD Manual (Purdue Reactive Molecular Dynamics Program)," 2010.

[199] S. Plimpton, P. Crozier, and A. Thompson, "LAMMPS-large-scale atomic/molecular massively parallel simulator," *Sandia National Laboratories,* 2007.

[200] H. M. Aktulga, J. C. Fogarty, S. A. Pandit, and A. Y. Grama, "Parallel reactive molecular dynamics: Numerical methods and algorithmic techniques," *Parallel Computing,* vol. 38, pp. 245-259, 2012.

[201] G. Te Velde, F. M. Bickelhaupt, E. J. Baerends, C. Fonseca Guerra, S. J. van Gisbergen, J. G. Snijders*, et al.*, "Chemistry with ADF," *Journal of Computational Chemistry,* vol. 22, pp. 931-967, 2001.

[202] K.-i. Nomura, R. K. Kalia, A. Nakano, P. Vashishta, A. C. van Duin, and W. A. Goddard III, "Dynamic transition in the structure of an energetic crystal during chemical reactions at shock front prior to detonation," *Physical review letters,* vol. 99, p. 148303, 2007.

[203] A. van Duin, "Reaxff user manual," *December 2002,* 2002.

[204] M. Laroussi and F. Leipold, "Evaluation of the roles of reactive species, heat, and UV radiation in the inactivation of bacterial cells by air plasmas at atmospheric pressure," *International Journal of Mass Spectrometry,* vol. 233, pp. 81-86, 2004.

[205] J.-P. Lim, H. S. Uhm, and S.-Z. Li, "Influence of oxygen in atmospheric-pressure argon plasma jet on sterilization of Bacillus atrophaeous spores," *Physics of Plasmas,* vol. 14, p. 093504, 2007.

[206] M. Laroussi, "Low-temperature plasmas for medicine?," *Plasma Science, IEEE Transactions on,* vol. 37, pp. 714-725, 2009.

[207] S. Sharif, M. Singh, S. J. Kim, and J. Schaefer, "Staphylococcus aureus peptidoglycan tertiary structure from carbon-13 spin diffusion," *Journal of the American Chemical Society,* vol. 131, pp. 7023-7030, 2009.

[208] T. Schneider, M. M. Senn, B. Berger-Bächi, A. Tossi, H. G. Sahl, and I. Wiedemann, "In vitro assembly of a complete, pentaglycine interpeptide bridge containing cell wall precursor (lipid II-Gly5) of Staphylococcus aureus," *Molecular microbiology,* vol. 53, pp. 675-685, 2004.

[209] B. A. Dmitriev, F. V. Toukach, K.-J. Schaper, O. Holst, E. T. Rietschel, and S. Ehlers, "Tertiary structure of bacterial murein: the scaffold model," *Journal of bacteriology,* vol. 185, pp. 3458-3468, 2003.

[210] W. Vollmer and J.-V. Höltje, "The architecture of the murein (peptidoglycan) in gram-negative bacteria: vertical scaffold or horizontal layer (s)?," *Journal of bacteriology,* vol. 186, pp. 5978-5987, 2004.

[211] B. Dmitriev, F. Toukach, and S. Ehlers, "Towards a comprehensive view of the bacterial cell wall," *TRENDS in Microbiology,* vol. 13, pp. 569-574, 2005.

[212] P. Bruice, "Organic Chemistry, fifth ed," *Person Prentice Hall, New Jersey,* p. 1041, 2007.

[213] J. Clayden, N. Greeves, S. Warren, and P. Wothers, "Organic Chemistry. New York 2001," ed: Oxford University Press Inc.

[214] H. Y. Kim, H. W. Lee, S. K. Kang, H. Wk. Lee, G. C. Kim, and J. K. Lee, "Modeling the chemical kinetics of atmospheric plasma for cell treatment in a liquid solution," *Physics of Plasmas,* vol. 19, p. 073518, 2012.

[215] R. Zellner, F. Ewig, R. Paschke, and G. Wagner, "Pressure and temperature dependence of the gas-phase recombination of hydroxyl radicals," *The Journal of Physical Chemistry,* vol. 92, pp. 4184-4190, 1988.

[216] M. Yusupov, A. Bogaerts, S. Huygh, R. Snoeckx, A. C. T. van Duin, and E. C. Neyts, "Plasma-Induced Destruction of Bacterial Cell Wall Components: A Reactive Molecular Dynamics Simulation," *The Journal of Physical Chemistry C,* vol. 117, pp. 5993-5998, 2013.

[217] D. Wang, D. Zhao, K. Feng, X. Zhang, D. Liu, and S. Yang, "The cold and atmospheric-pressure air surface barrier discharge plasma for large-area sterilization applications," *Applied Physics Letters,* vol. 98, p. 161501, 2011.

[218] F. Liu, P. Sun, N. Bai, Y. Tian, H. Zhou, S. Wei*, et al.*, "Inactivation of Bacteria in an Aqueous Environment by a Direct-Current, Cold-Atmospheric-Pressure Air Plasma Microjet," *Plasma Processes and Polymers,* vol. 7, pp. 231-236, 2010.

[219] T. K. Madhuri, D. Papatheodorou, A. Tailor, C. Sutton, and S. Butler-Manuel, "First clinical experience of argon neutral plasma energy in gynaecological surgery in the UK," *Gynecological Surgery,* vol. 7, pp. 423-425, 2010.

[220] W. Van Gaens and A. Bogaerts, "Kinetic modelling for an atmospheric pressure argon plasma jet in humid air," *Journal of Physics D: Applied Physics,* vol. 46, p. 275201, 2013.

[221] A. Mahfoudh, F. Poncin-Épaillard, M. Moisan, and J. Barbeau, "Effect of dry-ozone exposure on different polymer surfaces and their resulting biocidal action on sporulated bacteria," *Surface Science,* vol. 604, pp. 1487-1493, 2010.

[222] M. J. Pavlovich, H.-W. Chang, Y. Sakiyama, D. S. Clark, and D. B. Graves, "Ozone correlates with antibacterial effects from indirect air dielectric barrier discharge treatment of water," *Journal of Physics D: Applied Physics,* vol. 46, p. 145202, 2013.

[223] I.-F. W. Kuo and C. J. Mundy, "An ab initio molecular dynamics study of the aqueous liquid-vapor interface," *Science,* vol. 303, pp. 658-660, 2004.

[224] M. Sprik, J. Hutter, and M. Parrinello, "Abinitio molecular dynamics simulation of liquid water: Comparison of three gradient-corrected density functionals," *The Journal of chemical physics,* vol. 105, pp. 1142-1152, 1996.

[225] H. J. C. Berendsen, J. R. Grigera, and T. P. Straatsma, "The missing term in effective pair potentials," *The Journal of Physical Chemistry,* vol. 91, pp. 6269-6271, 1987.

[226] W. Benedict, N. Gailar, and E. K. Plyler, "Rotation-Vibration Spectra of Deuterated Water Vapor," *The Journal of Chemical Physics,* vol. 24, pp. 1139-1165, 2004.

[227] S. A. Clough, Y. Beers, G. P. Klein, and L. S. Rothman, "Dipole moment of water from Stark measurements of H2O, HDO, and D2O," *The Journal of Chemical Physics,* vol. 59, pp. 2254-2259, 2003.

[228] K. Krynicki, C. D. Green, and D. W. Sawyer, "Pressure and temperature dependence of self-diffusion in water," *Faraday Discussions of the Chemical Society,* vol. 66, pp. 199-208, 1978.

[229] D. J. Jacob, "Heterogeneous chemistry and tropospheric ozone," *Atmospheric Environment,* vol. 34, pp. 2131-2159, 2000.

[230] S. Chalmet and M. F. Ruiz-Lopez, "The structures of ozone and HOx radicals in aqueous solution from combined quantum/classical molecular dynamics simulations," *J Chem Phys,* vol. 124, p. 194502, May 21 2006.

[231] M. E. Tuckerman, D. Marx, and M. Parrinello, "The nature and transport mechanism of hydrated hydroxide ions in aqueous solution," *Nature,* vol. 417, pp. 925-929, 2002.

[232] S. T. Moin, T. S. Hofer, B. R. Randolf, and B. M. Rode, "An ab initio quantum mechanical charge field molecular dynamics simulation of hydrogen peroxide in water," *Computational and Theoretical Chemistry,* vol. 980, pp. 15-22, 2012.

[233] M. Khadre, A. Yousef, and J. G. Kim, "Microbiological aspects of ozone applications in food: a review," *Journal of Food Science,* vol. 66, pp. 1242-1252, 2001.

[234] Q. Shi, S. D. Belair, J. S. Francisco, and S. Kais, "On the interactions between atmospheric radicals and cloud droplets: a molecular picture of the interface," *Proc Natl Acad Sci U S A,* vol. 100, pp. 9686-90, Aug 19 2003.

[235] M. G. Campo and J. R. Grigera, "Classical molecular-dynamics simulation of the hydroxyl radical in water," *J Chem Phys,* vol. 123, p. 084507, Aug 22 2005.

[236] P. S. Stewart, "Diffusion in Biofilms," *Journal of Bacteriology,* vol. 185, pp. 1485-1491, 2003.

[237] X. Liu, M. M. Ramsey, X. Chen, D. Koley, M. Whiteley, and A. J. Bard, "Real-time mapping of a hydrogen peroxide concentration profile across a polymicrobial bacterial biofilm using scanning electrochemical microscopy," *Proceedings of the National Academy of Sciences,* vol. 108, pp. 2668-2673, 2011.

[238] S. van Stroe-Biezen, F. Everaerts, L. Janssen, and R. Tacken, "Diffusion coefficients of oxygen, hydrogen peroxide and glucose in a hydrogel," *Analytica chimica acta,* vol. 273, pp. 553-560, 1993.

[239] T. Henzler and E. Steudle, "Transport and metabolic degradation of hydrogen peroxide in Chara corallina: model calculations and measurements with the pressure probe suggest transport of H2O2 across water channels," *Journal of Experimental Botany,* vol. 51, pp. 2053-2066, 2000.

[240] M. Caroff and D. Karibian, "Structure of bacterial lipopolysaccharides," *Carbohydrate research,* vol. 338, pp. 2431-2447, 2003.

[241] U. Zähringer, Y. Knirel, B. Lindner, J. Helbig, A. Sonesson, R. Marre*, et al.*, "The lipopolysaccharide of Legionella pneumophila serogroup 1 (strain Philadelphia 1): chemical structure and biological significance," *Progress in clinical and biological research,* vol. 392, pp. 113-139, 1994.

Appendix

Force field parameters for the C/H/O/N/P system [124, 189].

```
Reactive MD-force field: Combined (see [124, 189])
 39        ! Number of general parameters
   50.0000 !Overcoordination parameter
    9.5469 !Overcoordination parameter
    1.6725 !Valency angle conjugation parameter
    1.7224 !Triple bond stabilization parameter
    6.8702 !Triple bond stabilization parameter
   60.4850 !C2-correction
    1.0588 !Undercoordination parameter
    4.6000 !Triple bond stabilization parameter
   12.1176 !Undercoordination parameter
   13.3056 !Undercoordination parameter
  -40.0000 !Triple bond stabilization energy
    0.0000 !Lower Taper-radius
   10.0000 !Upper Taper-radius
    2.8793 !Not used
   33.8667 !Valency undercoordination
    6.0891 !Valency angle/lone pair parameter
    1.0563 !Valency angle
    2.0384 !Valency angle parameter
    6.1431 !Not used
    6.9290 !Double bond/angle parameter
    0.3989 !Double bond/angle parameter: overcoord
    3.9954 !Double bond/angle parameter: overcoord
   -2.4837 !Not used
    5.7796 !Torsion/BO parameter
   10.0000 !Torsion overcoordination
    1.9487 !Torsion overcoordination
   -1.2327 !Conjugation 0 (not used)
    2.1645 !Conjugation
    1.5591 !vdWaals shielding
    0.1000 !Cutoff for bond order (*100)
    1.7602 !Valency angle conjugation parameter
    0.6991 !Overcoordination parameter
   50.0000 !Overcoordination parameter
    1.8512 !Valency/lone pair parameter
    0.5000 !Not used
   20.0000 !Not used
    5.0000 !Molecular energy (not used)
    0.0000 !Molecular energy (not used)
```

```
    0.7903 !Valency angle conjugation parameter
 7     ! Nr of atoms; cov.r; valency;a.m;Rvdw;Evdw;gammaEEM;cov.r2;#
          alfa;gammavdW;valency;Eunder;Eover;chiEEM;etaEEM;n.u.
          cov r3;Elp;Heat inc.;n.u.;n.u.;n.u.;n.u.
          ov/un;val1;n.u.;val3,vval4
C    1.3817    4.0000   12.0000    1.8903    0.1838    0.6544    1.1341    4.0000
     9.7559    2.1346    4.0000   34.9350   79.5548    5.4088    6.0000    0.0000
     1.2114    0.0000  202.2908    8.9539   34.9289   13.5366    0.8563    0.0000
    -2.8983    2.5000    1.0564    4.0000    2.9663    0.0000    0.0000    0.0000
H    0.8930    1.0000    1.0080    1.3550    0.0930    0.8203   -0.1000    1.0000
     8.2230   33.2894    1.0000    0.0000  121.1250    3.7248    9.6093    1.0000
    -0.1000    0.0000   55.1878    3.0408    2.4197    0.0003    1.0698    0.0000
   -19.4571    4.2733    1.0338    1.0000    2.8793    0.0000    0.0000    0.0000
O    1.2450    2.0000   15.9990    2.3890    0.1000    1.0898    1.0548    6.0000
     9.7300   13.8449    4.0000   37.5000  116.0768    8.5000    8.3122    2.0000
     0.9049    0.4056   68.0152    3.5027    0.7640    0.0021    0.9745    0.0000
    -3.5500    2.9000    1.0493    4.0000    2.9225    0.0000    0.0000    0.0000
N    1.2333    3.0000   14.0000    2.2403    0.1102    0.9928    1.1748    5.0000
     9.8276   12.0698    4.0000   30.2790  100.0000    6.1112    6.6645    2.0000
     1.0433    0.1000  119.9837    0.7382    6.7108    2.7268    0.9745    0.0000
    -2.0000    4.0000    1.0183    4.0000    2.8793    0.0000    0.0000    0.0000
S    1.9405    2.0000   32.0600    2.0677    0.2099    1.0336    1.5479    6.0000
     9.9575    4.9055    4.0000   52.9998  112.1416    6.5000    8.2545    2.0000
     1.4601    9.7177   71.1843    5.7487   23.2859   12.7147    0.9745    0.0000
   -11.0000    2.7466    1.0338    6.2998    2.8793    0.0000    0.0000    0.0000
Mg   1.8315    2.0000   24.3050    2.2464    0.1806    0.5020    1.0000    2.0000
    10.9186   27.1205    3.0000   38.0000    0.0000    0.9499    5.6130    0.0000
    -1.3000    0.0000  220.0000   49.9248    0.3370    0.0000    0.0000    0.0000
    -1.0823    2.3663    1.0564    6.0000    2.9663    0.0000    0.0000    0.0000
P    1.5994    3.0000   30.9738    1.7000    0.1743    1.0000    1.3000    5.0000
     9.1909   14.2932    5.0000    0.0000    0.0000    1.8292    7.2520    0.0000
    -1.0000   10.2596    1.5000    0.2205   16.7429   15.9629    0.0000    0.0000
    -2.5000    1.6114    1.0338    5.0000    2.8793    0.0000    0.0000    0.0000
15      ! Nr of bonds; Edis1;Lppen;n.u.;pbe1;pbo5;13corr;pbo6
                       pbe2;pbo3;pbo4;Etrip;pbo1;pbo2;ovcorr
 1  1 158.2004   99.1897   78.0000   -0.7738   -0.4550    1.0000   37.6117    0.4147
        0.4590   -0.1000    9.1628    1.0000   -0.0777    6.7268    1.0000    0.0000
 1  2 169.4760    0.0000    0.0000   -0.6083    0.0000    1.0000    6.0000    0.7652
        5.2290    1.0000    0.0000    1.0000   -0.0553    6.9316    0.0000    0.0000
 2  2 153.3934    0.0000    0.0000   -0.4600    0.0000    1.0000    6.0000    0.7300
        6.2500    1.0000    0.0000    1.0000   -0.0790    6.0552    0.0000    0.0000
 1  3 100.9167  136.3836   65.3877    0.3895   -0.3906    1.0000   18.8159    0.6674
        1.1202   -0.3411    9.1099    1.0000   -0.1966    5.6975    0.0000    0.0000
 3  3 142.2858  145.0000   50.8293    0.2506   -0.1000    1.0000   29.7503    0.6051
        0.3451   -0.1055    9.0000    1.0000   -0.1225    5.5000    1.0000    0.0000
```

```
  1  4 165.1874 148.6965  87.7249  -1.3237  -0.3504   1.0000  27.5446   0.1473
           0.1449  -0.2871   7.2074   1.0000  -0.2565   4.4890   1.0000   0.0000
  3  4 130.8596 169.4551  40.0000   0.3837  -0.1639   1.0000  35.0000   0.2000
           1.0000  -0.3579   7.0004   1.0000  -0.1193   6.8773   1.0000   0.0000
  4  4 157.9384  82.5526 152.5336   0.4010  -0.1034   1.0000  12.4261   0.5828
           0.1578  -0.1509  11.9186   1.0000  -0.0861   5.4271   1.0000   0.0000
  2  3 160.0000   0.0000   0.0000  -0.5725   0.0000   1.0000   6.0000   0.5626
           1.1150   1.0000   0.0000   0.0000  -0.0920   4.2790   0.0000   0.0000
  2  4 208.1369   0.0000   0.0000  -0.3949   0.0000   1.0000   6.0000   0.3340
           6.0174   1.0000   0.0000   1.0000  -0.1026   5.5235   0.0000   0.0000
  1  7 110.0000  92.0000   0.0000   0.2171  -0.1418   1.0000  13.1260   0.6000
           0.3601  -0.1310  10.7257   1.0000  -0.0869   5.3302   1.0000   0.0000
  2  7   0.1466   0.0000   0.0000   0.2250  -0.1418   1.0000  13.1260   0.6000
           0.3912  -0.1310   0.0000   1.0000  -0.1029   9.3302   0.0000   0.0000
  3  7 202.5868 164.1808   0.0000   0.5506  -0.5000   1.0000  25.0000   0.4300
           0.0912  -0.1285  16.0342   1.0000  -0.2008   6.2678   1.0000   0.0000
  4  7 130.0000   0.0000   0.0000   0.2171  -0.1418   1.0000  13.1260   0.6000
           0.3601  -0.1310  10.7257   1.0000  -0.0869   5.3302   1.0000   0.0000
  7  7   0.0000   0.0000   0.0000   0.2171  -0.5000   1.0000  35.0000   0.6000
           0.5000  -0.5000  20.0000   1.0000  -0.2000  10.0000   1.0000   0.0000
  7     ! Nr of off-diagonal terms; Ediss;Ro;gamma;rsigma;rpi;rpi2
  1  2   0.1239   1.4004   9.8467   1.1210  -1.0000  -1.0000
  2  3   0.0283   1.2885  10.9190   0.9215  -1.0000  -1.0000
  2  4   0.1275   1.3000   9.8924   1.0418  -1.0000  -1.0000
  1  3   0.0647   2.0109  10.0105   1.3177   1.2052   1.0682
  1  4   0.1952   1.8813   9.7734   1.3434   1.2545   1.1533
  3  4   0.1201   2.4775   9.0171   1.5285   1.0682   1.2716
  3  7   0.0611   1.7624  10.2685   1.7989   1.4523  -1.0000
 50     ! Nr of angles;at1;at2;at3;Thetao,o;ka;kb;pv1;pv2
  1  1  1  59.0573  30.7029   0.7606   0.0000   0.7180   6.2933   1.1244
  1  1  2  65.7758  14.5234   6.2481   0.0000   0.5665   0.0000   1.6255
  2  1  2  70.2607  25.2202   3.7312   0.0000   0.0050   0.0000   2.7500
  1  2  2   0.0000   0.0000   6.0000   0.0000   0.0000   0.0000   1.0400
  1  2  1   0.0000   3.4110   7.7350   0.0000   0.0000   0.0000   1.0400
  2  2  2   0.0000  27.9213   5.8635   0.0000   0.0000   0.0000   1.0400
  1  1  3  66.0686  28.5756   1.4793   0.0000   2.9950  58.6562   1.0000
  3  1  3  84.3310  21.5172   5.4724  -1.0000   1.5183   0.0000   2.9776
  1  1  4  66.8437  45.0000   1.2491   0.0000   1.1834   0.0000   3.0000
  3  1  4  82.7022  45.0000   0.5769   0.0000   1.1019   0.0000   1.0000
  4  1  4  90.0000  43.1792   0.5055   0.0000   1.1155   0.0000   1.0204
  2  1  3  64.3088  32.5434   2.1997   0.0000   0.1000   0.0000   1.2995
  2  1  4  63.9629  41.6246   1.4921   0.0000   0.2000   0.0000   2.8070
  1  2  4   0.0000   0.0019   6.3000   0.0000   0.0000   0.0000   1.0400
  1  3  1  68.4903  45.0000   1.3617   0.0000   2.8294   0.0000   1.0000
  1  3  3  80.6161  45.0000   1.4073   0.0000   1.0572  68.1072   1.4451
```

```
1  3  4   69.5983   45.0000    1.4248    0.0000    2.9000    0.0000    2.3286
3  3  3   89.9934   17.9465    1.7798    0.0000    2.9881    0.0000    1.0538
3  3  4   83.5202   33.7933    1.0337    0.0000    2.9000    0.0000    1.3398
4  3  4   67.1317   42.3748    1.7873    0.0000    3.0072    0.0000    1.5832
1  3  2   90.0000    7.1513    7.5000    0.0000    1.3111    0.0000    3.0000
2  3  3   75.6935   50.0000    2.0000    0.0000    1.0000    0.0000    1.1680
2  3  4   72.7348   20.1071    7.5000    0.0000    0.1000    0.0000    1.0746
2  3  2   85.8000    9.8453    2.2720    0.0000    2.8635    0.0000    1.5800
1  4  1   70.6778   12.3495    3.0486    0.0000    2.8702    0.0000    1.0000
1  4  3   73.9745   21.1329    2.3337    0.0000    2.8701    0.0000    1.7170
1  4  4   71.4579   14.0942    2.8540    0.0000    2.8701    0.0000    1.0631
3  4  3   74.2613   20.9008    2.8607  -18.0069    3.0701    0.0000    1.3874
3  4  4   74.2615   27.8669    1.6736   -0.9193    3.0117    0.0000    1.4381
4  4  4   73.3189   24.9685    2.2561    0.0000    2.9983    0.0000    2.1573
1  4  2   70.2498   13.6111    2.6311    0.0000    0.2025    0.0000    1.0000
2  4  3   74.5739   45.0000    1.4078    0.0000    0.3956    0.0000    3.0000
2  4  4   79.7136   45.0000    0.5316    0.0000    0.5437    0.0000    1.0000
2  4  2   80.2201    6.8385    7.5000    0.0000    0.1000    0.0000    1.0000
1  2  3    0.0000    8.9481    0.5983    0.0000    0.0000    0.0000    1.0000
1  2  4    0.0000    0.2694    2.1363    0.0000    0.0000    0.0000    1.8036
1  2  5    0.0000   15.0000    3.0000    0.0000    0.0000    0.0000    1.0400
3  2  3    0.0000   15.0000    2.8900    0.0000    0.0000    0.0000    2.8774
3  2  4    0.0000    1.0574    0.1000    0.0000    0.0000    0.0000    2.7676
4  2  4    0.0000    0.0100    1.0929    0.0000    0.0000    0.0000    2.1728
2  2  3    0.0000    8.5744    3.0000    0.0000    0.0000    0.0000    1.0421
2  2  4    0.0000    0.0019    6.0000    0.0000    0.0000    0.0000    1.0400
3  7  3   88.6293   18.2614    0.8145    0.0000   -0.1780    0.0000    2.3661
2  3  7   75.0000    7.8005    0.9394    0.0000    1.3523    0.0000    1.0400
3  3  7   60.0000   40.0000    4.0000    0.0000    1.0000    0.0000    1.0400
3  2  7    0.0000   10.0000    1.0000    0.0000    1.0000    0.0000    1.0400
7  3  7   50.6740   13.3258    0.1000    0.0000    1.0718    0.0000    1.1254
1  3  7   76.8677    5.4250    3.1105    0.0000   -0.0827    0.0000    2.1396
2  7  3   75.0000   25.0000    2.0000    0.0000    1.0000    0.0000    1.2500
3  7  7   70.0000   25.0000    2.0000    0.0000    1.0000    0.0000    1.2500
49    ! Nr of torsions;at1;at2;at3;at4;;V1;V2;V3;V2(BO);vconj;n.u;n
1  1  1  1   -0.2500   34.7453    0.0288   -6.3507   -1.6000    0.0000    0.0000
1  1  1  2   -0.2500   29.2131    0.2945   -4.9581   -2.1802    0.0000    0.0000
2  1  1  2   -0.2500   31.2081    0.4539   -4.8923   -2.2677    0.0000    0.0000
1  1  1  3   -0.5740   22.4215    0.8787   -2.7603   -1.1000    0.0000    0.0000
2  1  1  3    1.8164   18.8479    0.5134   -7.0513   -1.0978    0.0000    0.0000
3  1  1  3   -2.5000   56.1599   -1.0000   -4.3607   -0.8614    0.0000    0.0000
1  1  3  1    2.5000   14.6490    1.0000   -2.5209   -0.9000    0.0000    0.0000
1  1  3  2   -2.2946   11.6826   -1.0000   -2.5000   -0.9000    0.0000    0.0000
2  1  3  1   -1.0402   26.8401    0.6384   -2.5000   -0.9000    0.0000    0.0000
2  1  3  2   -1.0000   66.0304    0.7580   -5.4593   -1.1000    0.0000    0.0000
```

```
1  1  3  3    1.0182    5.3409    0.1292   -4.3356   -2.0544    0.0000    0.0000
2  1  3  3    2.1531   45.9655    1.0000   -2.5000   -2.8274    0.0000    0.0000
3  1  3  1    0.6706   80.0000   -0.2443   -4.7181   -3.0437    0.0000    0.0000
3  1  3  2   -1.0000   91.6742   -0.5000   -3.9849   -3.0476    0.0000    0.0000
3  1  3  3   -1.9346    5.0000    0.6401   -3.3416   -2.7174    0.0000    0.0000
1  3  3  1    1.0469    4.3827    0.8149   -3.4434   -2.7536    0.0000    0.0000
1  3  3  2   -2.5000   -0.5181    0.0268   -5.4085   -2.9498    0.0000    0.0000
2  3  3  2   -2.1995  -25.0000   -1.0000   -2.6000   -0.9921    0.0000    0.0000
1  3  3  3    2.4118  -24.8219    0.9706   -2.5004   -0.9972    0.0000    0.0000
2  3  3  3   -2.5000   43.1840   -0.6826   -6.6539   -1.2407    0.0000    0.0000
3  3  3  3   -2.5000  -25.0000    1.0000   -2.5000   -0.9000    0.0000    0.0000
1  1  4  2   -1.0000   71.4280   -0.5000   -8.0000   -1.9825    0.0000    0.0000
2  1  4  2   -1.0000   63.9914    0.7449   -8.0000   -2.1051    0.0000    0.0000
3  1  4  2   -1.0000   24.9527    1.0000   -4.6063   -2.5261    0.0000    0.0000
3  1  1  4    1.0000   25.3373    1.0000   -4.1453   -0.9511    0.0000    0.0000
4  1  1  4   -1.0000   21.8427    1.0000   -4.0686   -1.7241    0.0000    0.0000
1  1  4  1    1.0000   83.8750    1.0000   -6.5279   -1.6589    0.0000    0.0000
3  1  4  1   -1.0000   48.6477    1.0000   -8.0000   -1.8038    0.0000    0.0000
2  1  1  4    1.0000   98.8297   -0.2745   -4.9954   -1.9000    0.0000    0.0000
4  1  4  2    0.5000    2.8273   -0.1650   -7.9605   -2.0202    0.0000    0.0000
2  1  4  1   -1.0000   92.9120   -0.4541   -7.7688   -1.5996    0.0000    0.0000
0  1  2  0    0.0000    0.0000    0.0000    0.0000    0.0000    0.0000    0.0000
0  2  2  0    0.0000    0.0000    0.0000    0.0000    0.0000    0.0000    0.0000
0  2  3  0    0.0000    0.1000    0.0200   -2.5415    0.0000    0.0000    0.0000
0  1  1  0    0.0000   50.0000    0.3000   -4.0000   -2.0000    0.0000    0.0000
0  3  3  0    0.5511   25.4150    1.1330   -5.1903   -1.0000    0.0000    0.0000
0  1  4  0    0.2176   40.4126    0.3535   -3.9875   -2.0051    0.0000    0.0000
0  2  4  0    0.0000    0.1032    0.3000   -5.0965    0.0000    0.0000    0.0000
0  3  4  0    1.1397   61.3225    0.5139   -3.8507   -2.7831    0.0000    0.0000
0  4  4  0    0.7265   44.3155    1.0000   -4.4046   -2.0000    0.0000    0.0000
4  1  4  4   -0.0949    8.7582    0.3310   -7.9430   -2.0000    0.0000    0.0000
1  1  1  7    0.0000   19.3871    0.0103  -25.5765   -1.7255    0.0000    0.0000
7  1  1  7    0.0000   80.5586    0.1104   -8.0928   -1.7255    0.0000    0.0000
0  1  7  0    4.0000   45.8264    0.9000   -4.0000    0.0000    0.0000    0.0000
0  7  7  0    4.0000   45.8264    0.9000   -4.0000    0.0000    0.0000    0.0000
2  1  3  7   -1.5000   13.7486    0.1710   -3.7686    0.0000    0.0000    0.0000
2  3  7  3   -0.3120   -1.7990    0.2371   -3.2710    0.0000    0.0000    0.0000
1  3  7  3   -1.5000   -2.5000    0.6794   -2.5000    0.0000    0.0000    0.0000
7  3  7  3   -1.5000    7.4600   -0.9075   -9.0000    0.0000    0.0000    0.0000
4     ! Nr of hydrogen bonds;at1;at2;at3;Rhb;Dehb;vhb1
3  2  3    2.1200   -3.5800    1.4500   19.5000
3  2  4    2.1215   -7.5000    1.4500   19.5000
4  2  3    1.7500   -4.3286    1.4500   19.5000
4  2  4    2.4000   -2.3575    1.4500   19.5000
```

List of publications

Publications related to this thesis

1. **Yusupov M**, Neyts E C, Verlackt C C, Khalilov U, van Duin A C T and Bogaerts A 2014 Inactivation of the endotoxic biomolecule lipid A by oxygen plasma species: a reactive molecular dynamics study, submitted to *Plasma Process. Polym.*

2. Neyts E C, **Yusupov M**, Verlackt C and Bogaerts A 2014 Computer simulations of plasma-biomolecule and plasma-tissue interactions for a better insight in plasma medicine, accepted for publication in *J. Phys. D: Appl. Phys.*

3. **Yusupov M**, Neyts E C, Simon P, Berdiyorov G, Snoeckx R, van Duin A C T and Bogaerts A 2014 Reactive molecular dynamics simulations of oxygen species in a liquid water layer of interest for plasma medicine *J. Phys. D: Appl. Phys.* **47** 025205

4. **Yusupov M**, Bogaerts A, Huygh S, Snoeckx R, van Duin A C T and Neyts E C 2013 Plasma-induced destruction of bacterial cell wall components: a reactive molecular dynamics simulation *J. Phys. Chem. C* **117** 5993-5998

5. Bogaerts A, Aerts R, Snoeckx R, Somers W, Van Gaens W, **Yusupov M** and E Neyts 2012 Modeling of plasma and plasma-surface interactions for medical, environmental and nano applications *J. Phys.: Conf. Ser.* **399** 012011

6. **Yusupov M**, Neyts E C, Khalilov U, Snoeckx R, van Duin A C T and Bogaerts A 2012 Atomic scale simulations of plasma species interacting with bacterial cell walls *New J. Phys.* **14** 093043

Publications not related to this thesis

7. **Yusupov M**, Saraiva M, Depla D and Bogaerts A 2012 Sputter deposition of $Mg_xAl_yO_z$ thin films in a dual-magnetron device: a multi-species Monte Carlo model *New J. Phys.* **14** 073043

8. **Yusupov M**, Bultinck E, Depla D and Bogaerts A 2011 Elucidating the asymmetric behavior of the discharge in a dual magnetron sputter deposition system *Appl. Phys. Lett.* **98** 131502

9. **Yusupov M**, Bultinck E, Depla D and Bogaerts A 2011 Behavior of electrons in a dual-magnetron sputter deposition system: a Monte Carlo model *New J. Phys.* **13** 033018

10. Dzhurakhalov A A, Rahmatov S E, Elmonov A O, **Yusupov M** 2009 Orientation dependences of sputtering yield of two-component single crystals at grazing ion bombardment *J. Poverkhnost* **1** 78-82

11. Elmonov A A, **Yusupov M**, Dzhurakhalov A A, Bogaerts A 2008 Sputtering of Si(001) and SiC(001) by grazing ion bombardment *Publ. Astron. Obs. Belgrade* **84** 209-213

12. Dzhurakhalov A A, Rahmatov S E, Teshabaeva N A, **Yusupov M** 2005 Layer-by-layer sputtering and ultrathin ion implantation by low-energy grazing ion bombardment *MRS Proceedings* **908** 0908

Conference contributions

1. Verlackt C C, **Yusupov M**, Neyts E C and Bogaerts A, Atomic scale simulations of plasma interactions with the bacterial membrane and biofilm *Poster presentation at the International Workshop on Diagnostics and Modelling in Plasma Medicine (DMPM 2014)* May 23-24, 2014, Nara, Japan

2. **Yusupov M**, Verlackt C C, Neyts E C and Bogaerts A, Modeling of the behavior of reactive oxygen species in a liquid water layer of interest for plasma medicine *Poster presentation at the 5th International Conference on Plasma Medicine (ICPM5)* May 18-23, 2014, Nara, Japan

3. Bogaerts A, **Yusupov M**, Van der Paal J, Verlackt C C and Neyts E C, Modeling of plasma-biomolecule interactions for a better understanding of plasma medicine *Invited oral presentation at the 1st International Workshop on Plasma for Cancer Treatment (IWPCT 2014)* March 25-26, 2014, Washington DC, USA

4. Neyts E C, **Yusupov M**, Verlackt C C, Van der Paal J, Van Gaens W, Aernouts S and Bogaerts A, Atomic scale simulations for plasma medicine *Invited seminar at the Ruhr-Universität Bochum* November 22, 2013, Bochum, Germany

5. **Yusupov M**, Neyts E C and Bogaerts A, A reactive molecular dynamics study for plasma medicine applications *Poster presentation at the Symposium on Fundamentals of plasma-surface interactions* November 8, 2013, Antwerp, Belgium

6. Neyts E C, Somers W, **Yusupov M**, Aernouts S, Van der Paal J and Bogaerts A, Atomic scale simulations of reactive systems *Invited oral presentation at the "iPlasmaNano-IV Conference"* August 25-29, 2013, Monterey, California, U.S.A

7. **Yusupov M**, Neyts E C, Van der Paal J, Aernouts S and Bogaerts A, A reactive molecular dynamics study for plasma medicine applications *Poster presentation at the 21st International Symposium on Plasma Chemistry (ISPC 21)* August 4-9, 2013, Cairns, Australia

8. <u>Neyts E C</u>, Aernouts S, **Yusupov M**, Van der Paal J, Van Gaens W and Bogaerts A, Towards an atomic scale understanding of plasma medicine processes *Invited seminar at the Leibniz Institute for Plasma Science and Technology (INP Greifswald)* July 25, 2013, Greifswald, Germany

9. **Yusupov M**, Neyts E C and <u>Bogaerts A</u>, Atomic scale modeling of plasma-bacterial cell wall interactions for plasma medicine applications *Invited oral presentation at the Workshop "Plasma to Plasma!"* January 7-11, 2013, Leiden, The Netherlands

10. **Yusupov M**, Neyts E C and <u>Bogaerts A</u>, Investigation of plasma-bacteria cell wall interaction by atomic-scale simulations *Invited oral presentation at the High-Tech Plasma Processes – 12th European Plasma Conference (HTPP-12)* June 24-29, 2012, Bologna, Italy

11. <u>**Yusupov M**</u>, Neyts E C and Bogaerts A, Molecular dynamics simulation of plasma-bacteria cell wall interaction *Poster presentation at the 4th International Conference on Plasma Medicine (ICPM4)* June 17-21, 2012, Orléans, France

12. <u>**Yusupov M**</u>, Bultinck E, Saraiva M, Leroy W, Depla D and Bogaerts A, Simulation of an Ar/O$_2$ magnetron discharge in single and dual configurations with a multi-species Monte Carlo model *Poster presentation at the International Conference on Reactive Sputter Deposition (RSD 2010)* December 9-10, 2010, Ghent, Belgium

13. <u>**Yusupov M**</u>, Bultinck E, Depla D and Bogaerts A, Electron Monte Carlo model for a dual magnetron discharge, used for the sputter deposition of complex oxide layers *Poster presentation at the Twelfth International Conference on Plasma Surface Engineering (PSE 2010)* September 13-17, 2010, Garmish-Partenkirchen, Germany

14. Dzhurakhalov A A, Rahmatov S E, **Yusupov M** and Khalilov U, Sputtering processes of CuAu(100) and Cu$_3$Au(100) surfaces at low energy ion bombardment *Abstracts of 16th International Conference on Ion Beam Modification of Materials (IBMM 2008)* August 31-September 5, 2008, Dresden, Germany

15. Elmonov A A, **Yusupov M**, Dzhurakhalov A A and Bogaerts A Sputtering of Si(001) and SiC(001) by grazing ion bombardment *Proceedings of 24th

Summer School and International Symposium on the Physics of Ionized Gases (SPIG 2008) August 25-29, 2008, Novi Sad, Serbia

16. Dzhurakhalov A A, Elmonov A A and **Yusupov M**, Preferential sputtering of SiC(001) and GaAs(001) by grazing ion bombardment *Abstracts of 17th International Vacuum Congress, 13th International Conference on Surface Science, International Conference on Nano Science and Technology (IVC-17/ICSS-13 and ICNST 2007)* July 2-6, 2007, Stockholm, Sweden

17. Dzhurakhalov A A, Elmonov A A and **Yusupov M**, Sputtering of Si(001) and SiC(001) by grazing ion bombardment *Abstracts of XXV International Conference on Photonic, Electronic and Atomic Collisions (ICPEAC 2007)* July 25-31, 2007, Freiburg, Germany

18. Dzhurakhalov A A, Rahmatov S E, Elmonov A A and **Yusupov M**, Orientation dependence of sputtering yield of binary single crystals at grazing ion bombardment *Proceedings of XXXVII International Conference on Interaction of Charged Particles with Crystals* May 29-31, 2007, Moscow, Russia

19. Dzhurakhalov A A, Rahmatov S E and **Yusupov M**, Peculiarities of ion sputtering and implantation processes at grazing incidence *Abstracts of 15th International Conference on Ion Beam Modification of Materials (IBMM 2006)* September 18-22, 2006, Taormina, Italy

20. Dzhurakhalov A A, Rahmatov S E, Teshabaeva N A and **Yusupov M**, Layer-by-layer sputtering and ultrathin ion implantation by low-energy grazing ion bombardment *Proceedings of Materials Research Society (MRS) Fall Meeting* November 28 – December 2, 2005, Boston, Massachusetts, USA

21. Dzhurakhalov A A, Rahmatov S E, **Yusupov M** and Nabiev J M, Orientation dependence of ion-interaction processes at bombardment of surface by keV-energy ions *Oral Presentation at the Physical Electronics Conference (UzPEC-4)* November 2-4, 2005, Tashkent, Uzbekistan